Citation:
Postberg, F., Clark, R.N., Hansen, C.J., Coates, A.J., Dalle Ore, C.M., Scipioni, F., Hedman, M.M., and Waite, J.H. (2018b) Plume and Surface Composition of Enceladus, in *Enceladus and the Icy Moons of Saturn*, University of Arizona Press (Eds.: Schenk, Clark, Howett, Verbicer, Waite), pp 129-162.

Plume and Surface Composition of Enceladus

Frank Postberg
University of Heidelberg, Free University of Berlin

Roger N. Clark and Candice J. Hansen
Planetary Science Institute

Andrew J. Coates
University College London

Cristina M. Dalle Ore and Francesca Scipioni
NASA Ames Research Center

Matthew M. Hedman
University of Idaho

J. Hunter Waite
Southwest Research Institute

ABSTRACT

This chapter provides a comprehensive review of Enceladus' plume and surface composition as determined by the end of the Cassini mission. The Enceladean plume is composed of three different phases: Gas, solids (dust), and ions. In all three phases, water is by far the most abundant constituent, but other chemical species are also present. In the gas, H_2 and NH_3 and CO_2 are present with volume mixing ratios of at least fractions of a percent. Methane is the most abundant organic compound (≈ 0.2%), but several, yet unspecified, C_2 - and probably C_3 - species are present. The D/H ratio in the plume is much higher than in Saturn's atmosphere. Macroscopic ($r > 0.2$ μm) plume ice grains appear to be composed of ice in a primarily crystalline state. The main non-icy compounds in these grains are sodium salts and organic material. These materials are heterogeneously distributed over three compositionally diverse ice grain populations and can reach percent-level abundance in individual grains. Ice grains carrying salts or organics are larger than pure water ice grains and are found at higher frequencies in the plume than in the E ring. Organics in ice grains are more refractory than in plume gas with atomic masses of up to at least 200 u. O- and N-bearing organics are likely present in both gas and ice grains. The plume also hosts at least two kinds of nanograins. One, probably icy, population is dispersed inside the plume. The other is dominated by SiO_2 and appears to be embedded in larger ice grains and is only released later in the E ring. The possible origins of the different constituents in Enceladus' interior are discussed. There are more negatively than positively charged water ions in the plume. Cations have the form H_nO^+ ($n = 0 - 3$) and respective dimers, anions are dissociated water molecules (OH, H^-, O^-) or cluster of the form $(H_2O)_nOH^-$ ($n = 1 - 3$). Saturn's magnetosphere hosts an abundance of non-water cations that likely originate from plume constituents: NH^+ is the most abundant, with a mixing ratio of a few percent, followed by N^+, C^+ and cations with masses of 28 u.

Vertical compositional stratification of ice grains in the plume has been clearly documented, but there are also hints of compositional variations in ice grains emerging from different Tiger Stripe fractures. In cones of supersonic gas, heavier molecular species (e.g. CO_2) have a

narrower lateral spread than light species (e.g., H_2). Other spatial variations in the gas are likely, but could not be observed by Cassini's instruments. Although the plume shows clear activity variations over time, currently no compositional fluctuation could be linked to these variations.

Enceladus' surface is subject to constant resurfacing by deposition of plume ices and exhibits the cleanest water ice surface in the solar system. From infrared observations, CO_2 is present in these ices in the south polar terrain (SPT), deposition of aliphatic organics is also indicated there. From disk averaged UV observations, NH_3 might be generally present in surface ices. The best candidates for an additional UV absorber are "tholins" or iron rich nanograins. Predictions for plume deposition rates can be reasonably well matched with observations in various wavelengths, and indicate strong variations in grain size, but possibly also compositional variations. From plume composition, the SPT should be enriched in salts but these have not yet been detected with remote sensing. In the SPT, crystalline ice from plume deposits seems to be predominant. It is currently unclear whether amorphous ice exists on Enceladus' surface.

1. INTRODUCTION

The plume of Enceladus can be seen as the defining feature of Enceladus' uniqueness because no other icy body in the Solar System is currently known to exhibit such continuous and large-scale activity. The composition of the plume immediately became one of the highest priorities of the Cassini mission because it was suspected that compositional information would yield unique insights into interior processes, including (at the time putative) subsurface liquid water. And indeed, the current knowledge of the moon's interior exceeds that of most other planetary bodies (see chapters by Glein et al. Spencer et al. and Hemingway et al., this volume).

The diverse and flexible payload of the Cassini-Huygens flagship mission turned out to be a huge advantage because it enabled immediate follow-up investigations of the plume's composition without designing and launching an entirely new mission. Cassini's instruments were able to measure the composition of emitted gas, solid material (dust), and charged particles with both in situ and remote sensing techniques. During Cassini's extended mission (2008 – 2017) multiple close Enceladus flybys were incorporated into Cassini's tour around Saturn. During these flybys the spacecraft flew directly through the plume in order to allow Cassini's in situ instruments to investigate fresh samples from the Enceladean subsurface. Other flybys allowed high resolution imaging at ultraviolet, visible, and infrared wavelengths to observe the ice grains from the plume and the surface composition that resulted from the outflowing plume materials. A greater part of the ejected micron-sized and sub-micron-sized ice grains falls back onto the moon (Porco et al., 2006; Kempf et al., 2008; Ingersoll and Ewald, 2011) and Enceladus' surface is constantly exposed to ice particle deposition from the plume (Kempf et al., 2010, Schenk et al. 2011). Therefore the composition of the moon's surface is closely linked to the composition of the plume.

However, material emerging from Enceladus is not only apparent close to the moon: Cassini's measurements have shown that a greater part of all matter residing in the vast space between the orbits of the main rings and Titan is dominated by compounds that once were part of Enceladus. The most prominent witness to this fact is Saturn's diffuse E ring, which consists of ice grains that, after ejection into the plume, escape Enceladus' gravitational domain (see chapter by Kempf et al., this volume). In fact, a substantial part of our current knowledge about the plume's composition has been inferred by analyzing the material that escaped the moon's gravity. Neutral gas is ejected at such high velocities that it almost entirely escapes from Enceladus (Hansen et al., 2008). This is also true for charged particles that are quickly coupled to Saturn's magnetosphere.

In this chapter the word "jet" is used for individual, collimated sources that emerge from Enceladus' south polar fractures. "Plume" is used to refer to the entire south polar emission composed of all jets and diffuse sources along the fractures. We first discuss the composition of the plume's 3 distinct phases: Gas, micron-sized grains, and ionized particles (sections 2 – 4). We then try to link the identified compounds to possible subsurface sources (section 5). We review the current state of knowledge regarding Enceladus' surface composition (section 6) and then explore relationships between the compositions of the plume and the surface (section 7). The chapter concludes with an integrated summary and a presentation of major open questions (section 8).

2. COMPOSITION OF THE GAS PHASE

Two Cassini instruments have measured the gaseous component of Enceladus' plume: The Ion and Neutral Mass Spectrometer (INMS) and the Ultraviolet Imaging Spectrograph (UVIS). These instruments observe the plume from quite different and complementary perspectives. While INMS is an in situ detector that measures the composition along the flight path of the spacecraft through the plume, UVIS is a remote sensing instrument that observes the plume gas from a large distance, thereby integrating along the line of sight between the spacecraft and the star or Sun that is being occulted.

The analytical method of INMS is mass spectrometry. In its "closed source mode" neutral gas is collected in an antechamber, which is subsequently transferred through a tube into an ionization chamber. There, the gas is ionized by electron impact from electron guns. The atomic and molecular masses of the cations that form from this electron bombardment are then inferred by a quadrupole mass spectrometer with integer mass resolution ($m / \Delta m \sim$ unitary). The mass range of the instrument is 2 u – 99 u (u = atomic mass unit). The INMS also provides an open source mode where the neutral gas is ionized 'on the fly' and directly enters the quadrupole mass selection unit without interaction with the walls of the instrument's interior. For details about the INMS instrument see *Waite et al.* (2004).

UVIS identifies neutral gases in the plume by absorption of star- or sunlight at ultraviolet wavelengths (110 – 190 nm for stellar occultations, 55 – 110 nm for the solar occultation). Certain absorption features are specific to the molecules in the gas. The spectrum of starlight transmitted through an absorbing gas will be attenuated at different wavelengths in a manner that is diagnostic of the composition of the gas. The extinction due to absorption at a given wavelength for a particular gas is generally given as a cross-section. Then, to estimate the column density, the spectrum of the transmitted signal is compared to the spectral absorption features of a specific gas calculated from these cross-sections as a function of wavelength. For details about the UVIS instrument see *Esposito et al.* (2004).

To fully understand the current view of the plume gas composition it is helpful to review Cassini's exploration in chronological order. For that reason this section starts with the "early results" (subsection 2.1). Those readers that are just interested in the current state of the art might directly jump to subsection 2.2.

2.1 Early Cassini results

The first measurements of the gas composition of the plume of Enceladus by INMS and UVIS were both obtained on July 14th, 2005. Since the exact location of the plume was not known at that time, the measurements were serendipitous for both instruments.

It turned out that Cassini just touched the fringe of the plume during the July 2005 encounter (E2). Nevertheless, INMS mass spectra identified the main gas components of the plume. The data indicated that the atmospheric plume and coma was dominated by water, with significant amounts of carbon dioxide (~ 3%), an unidentified species with a mass of 28 u (~ 4% at that time reported to be either carbon monoxide (CO) or molecular nitrogen (N_2)), and methane (CH_4). Ammonia was detected at a level that did not exceed 0.5%. Trace quantities of acetylene and propane were also reported (*Waite et al.*, 2006).

The UVIS occultation of gamma Orionis, observed on the same day as the INMS measurement, showed that water is a clear match for all absorption features observed with adequate signal to noise ratio in the spectra. The best fit for the column density was given as 1.5 x 10^{16} H_2O molecules / cm^2. From that column density a total gaseous water emission rate of 150 - 350 kg/s could be inferred (*Hansen et al*., 2006). This number varied only slightly through subsequent occultations. The occultations of Zeta Orionis (Oct 2007), the Sun (May 2010), epsilon & zeta Orionis (Oct 2011), and epsilon Orionis (March 2016) yielded similar emission rates ranging from 170 kg/s to 250 kg/s, assuming the same typical gas velocities (*Hansen et al*., 2011, *Hansen et al*., 2017). Data shown in Figure 1 are from the occultation of zeta Orionis observed in 2007, compared to the theoretical water vapor spectrum calculation (Fig. 1).

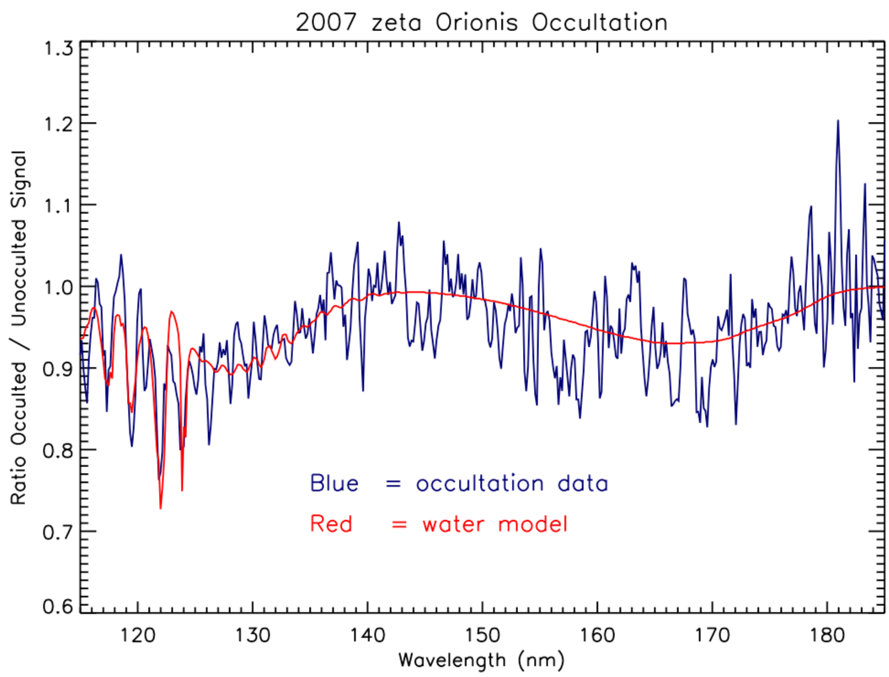

Figure 1. *The spectrum from zeta Orionis shows narrow absorption features between 115 and 130 nm diagnostic of water vapor and a broad absorption at ~155-175 nm. The smooth curve compares water vapor to the spectrum for the best-fit column density of 1.4 x 10^{16} cm^{-2}.*

In all individual occultations UVIS does not detect components other than water. However, tight upper limits for a number of constituents could be constrained and will be discussed in section 2.2.

The next opportunities to measure the plume of Enceladus in situ were the E3 and E5 encounters by Cassini in March and October 2008. As in the case of E2 the trajectories were highly inclined but the relative speed was much higher than at E2, with E5 providing the highest flyby speed of all Enceladus encounters (17.7 km/s compared to 8.2 km/s for E2). The higher flyby speed and the closer distance to the sources of the plume provided a substantial increase in signal-to-noise ratio of E5 compared to E2 and E3.

The E5 flyby data indicated inferential evidence for a liquid water ocean based on ^{40}Ar and ammonia detection in the plume (*Waite et al.*, 2009). However, ^{40}Ar has not been reproduced in subsequent measurements. The plume composition measurements, shown in Figure 2 & Table 1 (reproduced from Table 1 and Figure 1 of *Waite et al.*, 2009) indicate similar values to those of the earlier E2 flyby with two notable exceptions: 1) the number and concentration of organic compounds, especially above 50 u were significantly enhanced and 2) there was a substantially increased H_2 component in the plume. These anomalies were later explained as follows:

i. **Excess organic compounds were fragmentation products**: A view from the broader perspective of subsequent flybys (E14, E17, and E18; < 8 km s^{-1} flyby, see below) suggests that the higher flyby speed of E5 (17.7 km s^{-1}) lead to significant fragmentation of organic compounds with heavy molecular weight, outside the INMS mass range, that are found in the ice grains (*Postberg et al.*, 2018). Ice grains inevitably enter the INMS antechamber during plume traversals. In addition, fragmentation of gaseous molecules that hit the antechamber walls at these high speeds also contribute to the ambiguity of the spectrum. Consequently, most of the abundances depicted in Figure 2 & Table 1 and concentrations given therein, do not reflect the intrinsic gas composition (see caption of Table 1 for details). This is especially true for species with masses greater than 27u.
ii. **Excess hydrogen:** The hydrogen excess was explained by the vaporization of raw titanium from the walls of the titanium antechamber by hyper-velocity impacts of ice grains. Subsequent titanium oxidation reactions (TiO, TiO_2), lead to dissociation of H_2O vapor, yielding gaseous H_2 that was then measured by the mass spectrometer. Verification of this hypothesis using ballistic impact modeling has been published by *Walker et al.* (2015). Later low levels of native H_2 have been detected in the plume (section 2.3).

The serendipitous occurrence of the dissociation reaction described in ii. allowed the determination of the D/H ratio in H_2O from the relatively low mass resolution measurements provided by INMS. The value of 2.9 (+1.5/–0.7) x 10^{-4} is in the mid range of observed cometary D/H values and very similar to the values measured at Comet Halley (Balsiger et al., 1995), as opposed to the order of magnitude lower values found in the atmosphere of Saturn (Pierel et al., 2017). Based on this finding Waite et al. (2009) hypothesized that Enceladus might not have formed by sub nebula condensation processes during the cooling of the sub nebula but was formed or captured late in the Saturnian sub nebula formation process.

The E5 flyby could not resolve the determination and quantification of the species at 28 u because CO was abundantly produced by dissociation of larger CO-bearing species by molecular or ice grain hypervelocity impacts on, and reaction with, the walls of the INMS antechamber. Waite et al. (2009), estimated that up to 80% of the signal at mass 28 u was produced this way. The residual (~20%) of the mass 28 signal was attributed to N_2 or C_2H_4 (ethylene) or a combination of both with an upper limit of 1.2% (volume mixing ratio) for each substance. A ‘small contribution’ from intrinsic CO was also possible.

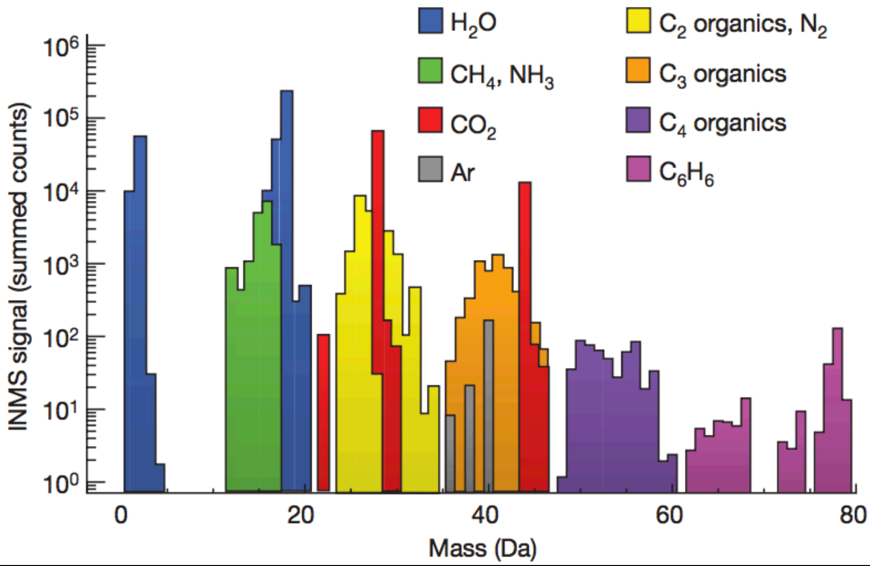

Group	Species	E5 Volume Mixing Ratio (%)	Fragmentation Class
1	H_2O*	90 ± 0.01	
	H_2*	[0.39]	II
	CO_2*	0.053 ± 0.01	
	CO*	[0.044]	II
	CH_4	0.009 ± 0.005	I
	NH_3	0.0082 ± 0.0002	
2	C_2H_2	$(3.3 \pm 2) \times 10^{-3}$	II
	C_2H_4	< 0.012	I
	C_2H_6	$< 1.7 \times 10^{-3}$	I
	HCN	$< 7.4 \times 10^{-3}$	I
	N_2	< 0.011	I
	H_2CO	$(3.1 \pm 1) \times 10^{-3}$	I
	CH_3OH	$(1.5 \pm 0.6) \times 10^{-4}$	I
	H_2S	$(2.1 \pm 1) \times 10^{-5}$	I+
3	(^{40}Ar)**	$(3.1 \pm 0.3) \times 10^{-4}$	II
	C_3H_4	$< 1.1 \times 10^{-4}$	I
	C_3H_6	$(1.4 \pm 0.3) \times 10^{-3}$	II
	C_3H_8	$< 1.1 \times 10^{-4}$	II
	C_2H_4O	$< 7.0 \times 10^{-4}$	I
	C_2H_6O	$< 3.0 \times 10^{-4}$	I
4	C_4H_2	$(3.7 \pm 0.8) \times 10^{-5}$	I+
	C_4H_4	$(1.5 \pm 0.6) \times 10^{-5}$	I+
	C_4H_6	$(5.7 \pm 3) \times 10^{-5}$	I+
	C_4H_8	$(2.3 \pm 0.3) \times 10^{-4}$	II
	C_4H_{10}	$< 7.2 \times 10^{-4}$	II
	C_5H_6	$< 2.7 \times 10^{-6}$	I+
	C_5H_{12}	$< 6.2 \times 10^{-5}$	I+
	C_6H_6	$(8.1 \pm 1) \times 10^{-5}$	I+

Figure 2 & Table 1*. Volume mixing ratios based on analysis of the E5 data presented in Waite et al. (2009), Figure 2 with permission from Nature. Abundances cover the range of accepted composition models for ionization and fragmentation by INMS's electron guns that adequately fit the E5 mass*

spectrum. This table has been augmented to include insights from later flybys. In particular, most values are heavily influenced by molecular fragmentation from high velocity wall impacts, of mostly heavy organics, that are responsible for a greater part of the organic species in the spectrum.
Species listed with upper limits (grey color) are present in some INMS ionization models but absent from others and are potentially present rather than definitive detections. Fragmentation Class indicates the apparent contribution from heavy organic fragmentation by high velocity wall impacts upon the listed abundances observed during the fast E5 flyby (~17.7 km/s). It is based upon the increase in abundance compared to "slow" (< 8 km/s) flybys (E14, E17, E18, E21). Fragmentation Class I indicates a species with a substantial contribution from fragmentation (factor of 2 – 20 larger than at "slow" flybys), Class II indicates species that are almost exclusively due to fragmentation (> factor 20 abundance compared to slow flybys). Class "I+" indicates a species that has not been detected on slow flybys and thus Class I is only a lower limit for the degree of contributions from fragmentation. It is very likely that the abundances for these species are primarily or exclusively due to heavy organic fragmentation. Group 1 indicates major species, group 2 represents the "C2 region" of the spectrum (masses 24-34), group 3 the "C3 region" (masses 36-46) and group 4 the "C4+ region" (masses 48-80) of the spectrum.

* *The mixing ratios for H_2 in brackets have been included in the mixing ratio for H_2O as it is believed the vast majority of H_2 is produced from interaction of hyper-velocity ice grains on the INMS antechamber (see item 'ii' above). The fragmentation class assigned to H_2 is with respect to H_2O. The mixing ratio for CO in brackets has likewise been included in the mixing ratio for CO_2 due to indications of a similar hyper-velocity-induced dissociation process. However, from the low abundance of CO_2 during slow flybys (Table 2) it seems that CO is rather an organic fragmentation product and thus the value for CO_2 in Table 1 and Waite et al. (2009) is substantially overestimated by the addition of CO (4.4%) to the E5 CO_2 raw signal of just 0.9%.*

** *^{40}Ar abundance was originally based upon the lack of fit at mass channel 40 from other potentially contributing species such as C_3H_4 and C_3H_6. However, subsequent analysis of the "slow" Enceladus flybys indicates a large reduction in the abundance of species at mass 40 (and neighbors), as can be seen by the fragmentation class of II. ^{40}Ar cannot be a product of heavy organic fragmentation, so it is much more likely that the ^{40}Ar signal originally reported for the E5 flyby is rather due to some mixture of organic fragments not yet fully understood.*

2.2. Refined Cassini Results

UVIS plume occultations between 2007 and 2011 helped place strong constraints on the possibilities for the ambiguous species at mass 28 (CO, N_2, C_2H_4). An analysis of deviations from a pure water vapor spectrum during stellar occultations yielded an upper limit of 0.9% for CO (Hansen et al. 2006, 2017). A solar occultation by the plume in 2010 presented the unique opportunity to use UVIS' extreme ultraviolet channel (55 – 110nm) to constrain the N_2 abundance in the plume because this wavelength range includes N_2 absorption features. Although the solar occultation did not reveal any absorptions by N_2, the non-detection of such features set an upper limit of 0.5% N_2 in the plume. These upper limits further reduced the options left from the INMS E5 data (*Waite et al*., 2009). Recently, the UVIS team summed many extremely long UVIS integrations of ultraviolet light reflected by the plume and produced a multiply scattered spectrum with features associated with those of hydrocarbon absorbers, primarily C_2H_4 (*Shemansky et al*., 2016). Although this is the first unambiguous detection of a 28 u gas species, a mixing ratio has not been inferred yet.

The UVIS data have been tested for the presence of both methanol (CH_3OH) and ammonia (NH_3). Fits of the spectrum improve when methanol is added to the pure water absorption spectrum, however there are no spectral features with adequate signal to noise ratios to allow unambiguous identification or even an upper limit of methanol as a constituent. As was the case for methanol, adding NH_3 to the model plume composition improved the overall fit by increasing absorption at short wavelengths. In the case of NH_3 there are definitive spectral features that should show up in the spectrum. However, these features are not detectable at the 0.4 to 1.3% level reported by INMS (*Waite et al.*, 2017; see Table 2). UVIS data are thus consistent with, but cannot be used to independently verify the INMS NH_3 estimate.

INMS plume spectra obtained from the E14, E17, and E18 flybys in 2011 and 2012 provided a much more consistent picture of the gas composition of the plume than previous INMS data. The flybys all occurred with ~7.5 km/s relative speed horizontally over the south polar region with closest approaches ranging from 75 to 100 km in altitude above the vent surface. This configuration allowed for good signal to noise ratios, but avoided effective molecular breakup from wall impacts (evident by the lack of species above 50u). As can be seen in Figure 3, the mass spectra were remarkably similar allowing a deconvolution analysis of the compositional data (Magee et al., in preparation). This allowed a more confident determination of the major volatiles (Table 2) with the exception of the abundance of native H_2 (due to interference with H_2 from H_2O dissociation, see item 'ii' in section 2.1).

Therefore, the efforts of E14, E17, and E18 were complemented in October 2015 by the measurements of the E21 flyby, a horizontal south polar flyby with a closest approach of only 50 km and a relative speed of 8.5 km/s. Here, the INMS for the first time used its open source mode in the Enceladean plume. Although the open source mode is a factor of 400 less sensitive than the closed source mode and comes with strict pointing requirements, it allows for mitigation of the effects from titanium reactions of the closed source antechamber since the material is ionized without wall interaction. The open source concentrations of major volatiles measured during E21 agree with the numbers inferred during E14, E17, and E18 with the exception of mass 28 (see discussion below). The E21 measurements most importantly enabled the detection and quantification of the mixing ratio of H_2 in the plume (*Waite et al.*, 2017). All resulting major volatiles are shown in Table 2.

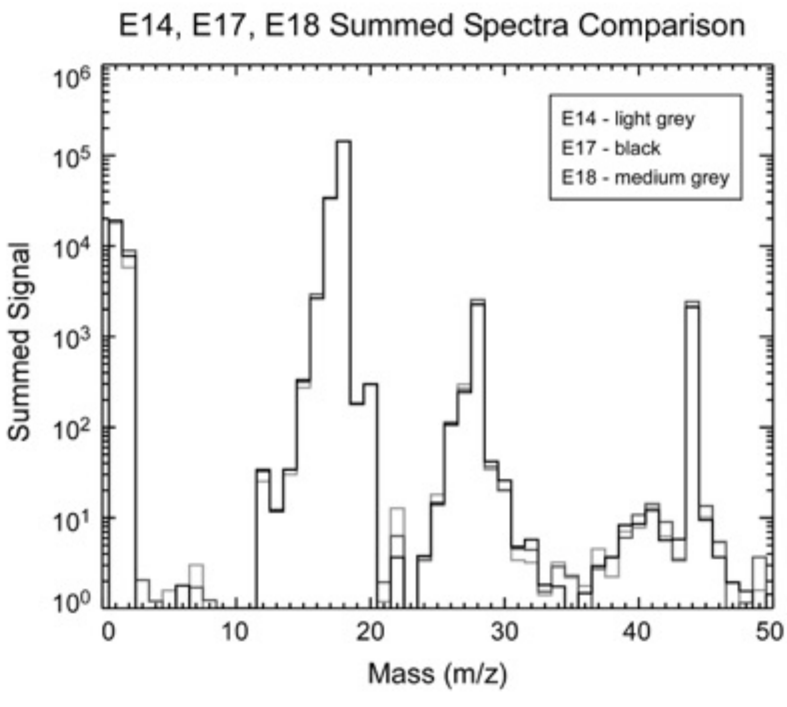

Figure 3: *The mass spectra from flybys E14 (light grey), E17 (black), and E18 (medium grey) show the reproducibility of the gas composition from these lower velocity flybys (~7.5 km s^{-1}). The summed signal amplitude of each spectrum is set relative to the noise floor, such that the*

minimum value on the y-scale represents unit signal-to-noise ratio.

Table 2: *Final volume mixing ratios of all confirmed neutral gas compounds in Enceladus' plume from Cassini INMS measurements reproduced from Waite et al., 2017 Table 1 (with permission from Science).*

H_2O	CO_2	CH_4	NH_3	H_2
96 to 99 %	0.3 to 0.8 %	0.1 to 0.3 %	0.4 to 1.3 %	0.4 to 1.4 %

Surprisingly a species with a mass of 28 u was not seen in the open source data from E21 suggesting that the respective signal seen in the closed source is largely due to a fragmentation product (CO or C_2H_4) from heavier, maybe organic, molecules. The results exclude any 28 u intrinsic species in the plume gas at a mixing ratio of 0.1% (Waite et al. 2017). It is currently unclear if this low fraction of a native plume volatile at 28 u is sufficient to be in agreement with the tentative detection of weak C_2H_4 reflection features by UVIS (Shemansky et al., 2016).

Analysis of the organic compounds via mass deconvolution for both organic compounds carrying 2 or 3 carbon atoms (C_2 and C_3 species) obtained at E14, E17, and E18 leads to a host of ambiguities (Magee et al., in preparation) that can only be resolved with higher mass resolution mass spectrometers on future missions. These compounds with unresolved ambiguities that might be present in the plume are shown in Table 3. Organic molecular species with 3 or more carbon atoms or other species above 50 u were not detected on the low speed flybys. These compounds are not present in the plume gas at mixing ratios accessible to INMS and the concentrations given in Table 3 can be seen as upper limits. The detection of organic species with high molecular masses in detectable concentration on high-speed flybys, at E3 and E5 (*Waite et al.*, 2009) was due to fragmentation of organic molecules (Figure 2 & Table 1) above the mass range of INMS, likely residing in ice grains (Postberg et al., 2018). Also see sections 3.1 and 5.1.

Table 3. *(modified from Magee & Waite, 2017): Ambiguous constituents and their possible concentrations from the deconvolution analysis of INMS spectra obtained at "slow" flybys (E14, E17, E18, and E21). Left panel: Some combination of at least four of the listed species at concentration >100 ppm is required to match the INMS spectra. These species dominate the C2 region of the spectrum (masses 24-34). Right panel: Many possible combinations of the listed species at low concentrations may match the INMS spectra, but at least some of these species are necessary to do so. Isomers are possible in some cases. These species are primarily used to fit the C3 region (masses 36-46).*

Minor Species I Moderate Ambiguity > 100 ppm < 0.2%	**Minor Species II** High Ambiguity < 100 ppm				
	Hydrocarbons	**N-bearing**	**O-bearing**	**NO-bearing**	**Others…**
C_2H_2 (26)	C_3H_4 (40)	CH_5N (31)	O_2 (32)	C_2H_7NO (61)	H_2S (34)
HCN (27)	C_3H_6 (42)	C_2H_3N (41)	CH_3OH (32)	$C_2H_5NO_2$ (75)	PH_3 (34)
C_2H_4 (28)	C_3H_8 (44)	C_2H_7N (45)	C_2H_2O (42)	$C_3H_7NO_2$ (89)	Ar (36,40)
CO (28)	C_4H_8 (56)	$C_2H_6N_2$ (58)	C_2H_4O (44)		C_3H_5Cl (76)
N_2 (28)	C_4H_{10} (58)	C_4H_9N (71)	C_2H_6O (46)		
C_2H_6 (30)	C_5H_{10} (70)	$C_4H_8N_2$ (84)	C_3H_6O (58)		
CH_2O (30)	C_5H_{12} (72)	$C_6H_{12}N_4$ (140)	C_3H_8O (60)		
NO (30)	C_8H_{18} (114)		$C_2H_4O_2$ (60)		
			$C_2H_6O_2$ (62)		
			$C_4H_{10}O$ (74)		
			$C_4H_6O_2$ (86)		

2.3. Compositional variation in space and time

Horizontal variation of the neutral gas density within the plume is substantial. The gas plume seems to consist of supersonic collimated high velocity components ('jets') and emissions from much slower outgassing all along the south polar fractures (*Hansen et al. 2008*, *Teolis et al.* 2017). This idea is in agreement with the observed stratified ice grain emission (Postberg et al. 2011a, *Porco et al.* 2014, *Spitale et al*. 2015) (see section 3.2). It is currently unclear if a compositional variation is linked to this emission because of the low spatial resolution of the published UVIS and INMS compositional results. However, INMS measurements indicate that in supersonic jets, emissions of heavy molecular species (e.g. CO_2, 44u) are subject to a smaller lateral spread than lighter species (e.g., H_2, H_2O) (*Yeoh et al. 2015*, *Perry et al.* 2015). Modeling of these effects shows that the relative abundance of CO_2 and H_2O at altitude can vary more than 30% from the center to the edge of a jet (*Hurley et al.* 2015). This scenario is true for individual sources (Figure 4) but probably also generally affects the south polar plume as a whole, which is a superposition of these sources.

In contrast to ice grain emission, variations in time of the integrated gas emission rate in the entire south polar plume appear to be mild (*Hansen et al.* 2011, 2017). However, emission rate variations of individual gas jets are substantial (*Hansen et al.* 2017, *Teolis et al.* 2017). It is not known if these variations over time correlate with variation in the composition of the gas phase. Limited compositional variations in the gas of individual jet sources over time are likely but have not yet been identified in the Cassini data although major compositional changes in the overall plume gas composition were not observed (*Waite et al.* 2017, *Magee et* *al.*, in preparation).

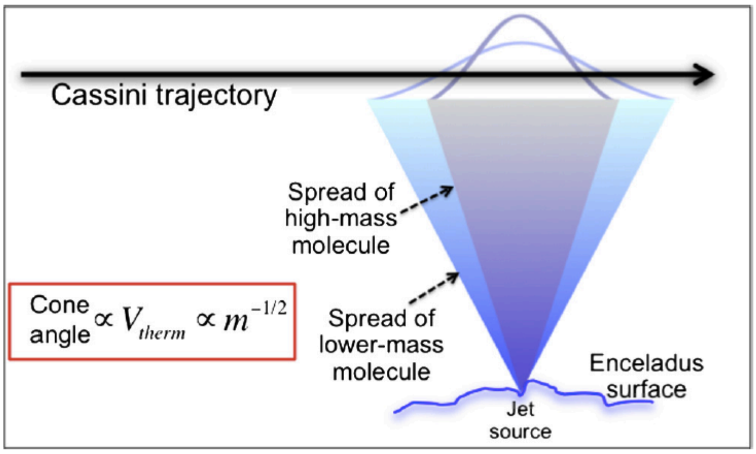

Figure 4 *(from Perry et al. 2015): Illustration of the mass dependent behavior of high-velocity molecules emitted by the jets. For molecules emitted at the same supersonic velocity and in thermal equilibrium with each other at the time they are emitted, the cone angle or spreading of the molecules depends on the molecular mass. This behavior causes differences in spatial composition that are measured by the INMS. Depending on the temperature, bulk velocity and mass, spreading angles vary from 10 to 45 degrees. Cassini's closest approach during horizontal south polar flybys typically was between 50 and 100 km.*

3. COMPOSITION OF THE SOLID PHASE

Three Cassini instruments have assessed the chemical composition of the icy component of Enceladus' plume: The Cosmic Dust Analyser – CDA (Srama et al. 2004), the Cassini Plasma Spectrometer (CAPS) (Young et al. 2004), and the Visible and Infrared Mapping Spectrometer (VIMS) (Brown et al. 2004). The former two are in situ detectors that measure the particles along the flight path of the spacecraft through the plume. While the CDA's Time of flight – mass spectrometer (TOF-MS) subsystem is sensitive to ice grains with radii of about 0.2 – 2 µm, CAPS observes much smaller grains with sizes of up to about 0.003 µm. VIMS is a remote sensing instrument that observes the plume ice grains from a large distance at infrared wavelengths (1 – 5 µm), thereby integrating along its line of sight. On a few occasions the observation geometry allowed VIMS to acquire spatially resolved spectra of the plume.

It is important to remember that a small fraction of plume particles (about 5 - 10% by mass) are launched fast enough to escape Enceladus' gravity and populate the E ring, while the rest of the icy grains fall back onto the moon's surface (Porco et al., 2006; Kempf et al., 2008, 2010; Hedman et al. 2009, Ingersoll and Ewald, 2011). Hence the composition of E ring grains, as well as plume particles can provide information about Enceladus' interior.

We will first discuss implications for the plume composition derived from the CDA's E ring spectra (3.1) and then the results from plume traversals (3.2). We address the nanodust population in the plume observed by CAPS (3.3) and finally the remote sensing results from VIMS (3.4).

3.1 CDA measurements in the E ring.

In practice, most of the knowledge of the composition of ice grains emitted by Enceladus comes from the CDA, an impact ionization detector. When dust or ice grains strike the detector's metal target plate with speeds in excess of 1 km/s, a part of the impactor is ionized. CDA then produces time-of-flight mass spectra of the cations present in each individual impact cloud with a transmission cadence of up to 1 spectrum every 2 seconds. The mass resolution of the instrument is relatively low: $m/\Delta m$ increases from ≈ 10 at 1u up to ≈ 50 at the upper end of the CDA mass range at about 200u (Postberg et al., 2006). From 2004 to 2017 CDA obtained tens of thousands of mass spectra of individual ice grains. Most of them were recorded in the E ring and only a few hundred directly in the plume. As CDA was not built to operate in a dense dusty environment like the Enceladean plume, the instrument settings needed to be tweaked to allow plume measurements. These instrument settings always compromised the quality of plume spectra. However, in the E ring, CDA could be operated nominally and therefore, the E ring spectra provide both, the highest quality spectra and the better statistics, whereas measurements in the plume provide insights into its spatial compositional structure.

The impact ionization process yields different cation abundances of identically composed particles at different impact speeds (Postberg et al., 2008, 2011b). Impact speeds of ice grains during the Cassini mission vary between 3.5 km/s to 20 km/s. It often is a challenge to disentangle speed effects on the spectra from spectral variations that are due to actual compositional variations.

CDA measurements obtained during Cassini's first E-ring crossing in October 2004 quickly confirmed that the particles in the E-ring are mostly composed of water ice (Hillier et al., 2007). Over 99% of particles detected in the entire E ring are dominated by water ice. However, CDA also found that there are significant differences in the compositions of these ice grains, and that about 95% of all E ring mass spectra from the CDA can be categorized into three major distinct families (Postberg et al., 2008, 2009a). The abundance of each compositional type given below is based on the evaluation of about 10,000 E ring ice grain spectra. These families are also present in the plume itself, though in different proportions (see section 3.2). Although interplanetary and interstellar dust (Altobelli et al., 2016) has been detected in the E ring, it does not have an E ring origin and therefore is not discussed here.

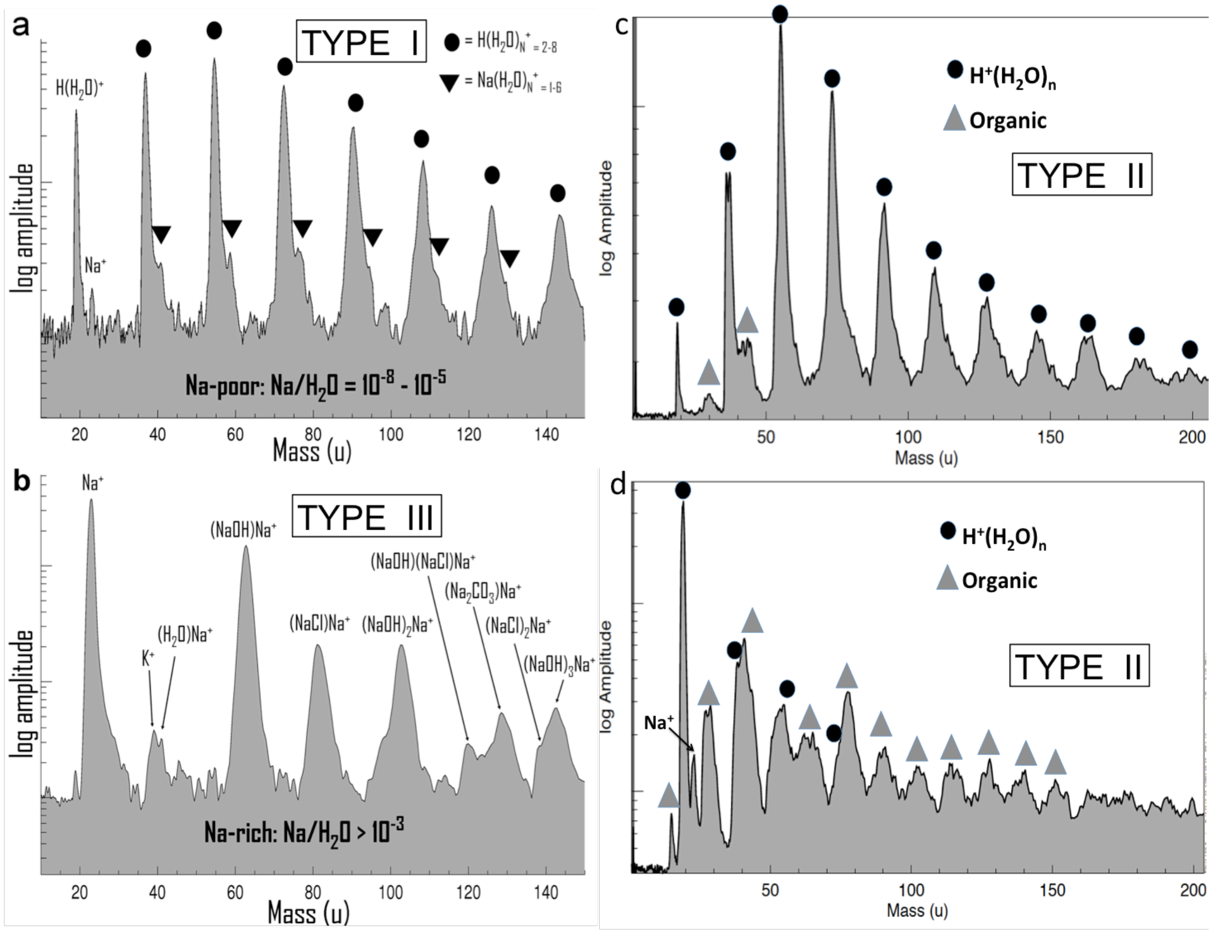

Figure 5: *Panels a and b from Postberg et al. (2009a). Different compositional Types in representative CDA mass spectra of E ring ice grains. (a) Type I spectra show mostly water with only traces of sodium. In contrast, Type III spectra shown in (b) exhibit strong mass lines from different sodium salts. Type II spectra (c) and (d), show a wide variety within their group. Many are very similar to Type I with the addition of subtle mass lines in agreement with molecular organic cations carrying only 1 - 3 carbon atoms (c). A few Type II spectra show abundant organic cations, some of them in excess of 100u (d).*

- Type I particles: About 65% of all E ring spectra belong to this group, increasing to even higher fractions with decreasing particle size. These grains appear to be composed of nearly pure water ice because their spectra are dominated by mass lines caused by water-cluster cations $(H_2O)_n(H_3O)^+$, (n = 0 - 15, see Figure 5a). Na^+ and K^+ and their respective water cluster ions $(H_2O)_n(Na, K)^+$ are often present and form the only non-water mass lines. These lines imply mostly very low concentrations of alkali salts in the ice grains with Na/H_2O ratios on the order of 10^{-7} (Postberg et al., 2009a).
- Type II particles: Type II particles on average produce higher total ion yields upon impact, implying they are larger on average than Type I particles. Type II spectra represent the second most abundant E ring family (≈ 25%, increasing with increasing grain size) and in most cases show the same characteristic as Type I with an additional distinct feature at mass 27u to 31u and/or 39u to 45u, with each of these mostly organic features representing more than one ion species (Postberg et al., 2008). In some cases additional non-water signatures, indicative of additional organic compounds, appear. The fraction of organics and the composition of the organic species can vary dramatically among the different grains (Figures 4c and d). Furthermore, while organic signatures are the most prominent non-water species,

sometimes contributions from silicates and salts may be present. Most Type II spectra are salt-poor, similar to Type I.

- Type III particles: This family of about 10% of E ring spectra exhibits a totally different pattern of mass lines (Figure 5b) than the other two. In contrast to Type I and II, the water cluster peaks $(H_2O)_n(H_3O)^+$ are absent or barely recognizable. The characterizing mass lines are of the form $(NaOH)_n(Na)^+$ (n = 0 - 4) indicating a Na/H_2O mole ratio well above 10^{-3}. Frequent mass lines of $NaCl\text{-}Na^+$ and $Na_2CO_3\text{-}Na^+$ reveal NaCl and $NaHCO_3$ and/or Na_2CO_3 as the main sodium bearing compounds. Ground experiments with analogue material indicate an average concentration of 0.5 - 2% sodium and potassium salts by mass, with K compounds being less abundant by far (Postberg et al., 2009a, 2009b). Impacts of Type III particles have an average ion yield which is several times higher than of Type I particles, implying a considerably larger size (Postberg et al., 2011a).

In a few impact spectra, a combination of spectral features from different Types (e.g., Type II and Type III) are found. While Type I and Type III grains are fairly homogenous within their compositional family, the organic bearing Type II grains are quite compositionally diverse, with the concentrations of organic species varying from traces up to the percent level (Postberg et al., 2018). Most Type II grains show one or two groups of organic mass lines between 26u and 31u and 39u and 45u respectively. These cations are indicative of C_2 and C_3 hydrocarbons respectively but could also contain oxygen and nitrogen bearing species, e.g. CH_xO^+, x = 1-3 or $CH_2NH_2^+$ between 29 and 31u or respective C_2 species between 41u and 45 u. In general these organic species are in agreement with volatile organics observed by INMS (Magee et al., in preparation).

However, a small fraction of Type II grains exhibits strong organic mass lines at masses in excess of 70u up to the end of the CDA mass range at 200u (Postberg et al., 2018). These high mass organics cations (HMOC) indicative of concentrations on the percent level might stem from refractory organic inclusions in the ice grains (section 5.1). The HMOC type grains show aromatic and aliphatic constituents with functional groups containing oxygen and likely nitrogen. It is possible that all these constituents originate from cross-linked or polymerized macromolecules (Postberg et al. 2018). These high-mass organics species residing in ice grains might have also been observed by the INMS in the plume during high speed flybys, where the high impact velocity disintegrated large molecules to organic fragments small enough to show up in INMS limited mass range (< 100 u) (Postberg et al., 2018, see section 2.1). The observation of unspecified high mass molecular species in the plume by CAPS (Coates et al., 2010a, 2010b) might also be due to large fragment ions from these organic species (see section 4.1).

Another dust population observed by the CDA instrument that can provide information about the E ring's composition, and thus Enceladus' plume, are the so-called `stream particles'. These are high-speed, nanometer-sized dust particles that are not gravitationally bound to the Saturnian system and were seen for the first time well before Cassini reached Saturn (Kempf et al., 2005b; Hsu et al., 2010). These tiny grains of dust, once charged, gain sufficient kinetic energy from Saturn's magnetic field to be thrown out of orbit into interplanetary space (Grün et al., 1993; Hamilton and Burns, 1993; Horanyi et al., 1993; Kempf et al., 2005b; Hsu et al., 2010, 2011, 2012). Numerical modeling of their trajectories indicates that the majority of Saturn's stream particles were once part of the E ring before they were ejected into the streams. Moreover, from their composition and dynamical modeling these particles are thought to be inclusions released from much larger E ring ice grains by the magnetospheric plasma erosion (Hsu et al., 2011, 2015).

CDA can only detect these tiny grains because they hit the detector with extraordinary high speed, acquired by their magnetospheric interaction, typically exceeding 100 km/s (Hsu et al., 2010). Still, only the largest of stream particles (≈ 20%) produce a signal that is strong enough to allow a rough characterization of their composition with CDA (Hsu et al. 2011). These particles provide unique information about the plume's composition because, unlike E ring grains, many of these largest Saturnian stream particles have silicon as a major constituent and are depleted in water ice (Kempf et al., 2005a; Hsu et al., 2011). Co-adding of the weaker signals shows that at least a part of the grains that show no individual particle signal (≈ 80%) have a similar silicon-rich composition (Hsu et al. 2011). The strongest stream particle spectra nearly all show a silicon mass line and have been used by Hsu et al. (2015) for more detailed compositional analysis. They find that they are almost metal-free with a composition in agreement with pure silica (SiO_2) rather than typical rock-forming silicates (e.g., olivine or pyroxene). A size estimate derived from their dynamical properties by numerical modeling (Hsu et al. 2011) agrees with the sizes inferred from the spectra signal of the silca grains on a very confined size range with radii ranging 2 – 9 nm (Hsu et al. 2015). A rough quantitative estimate by Hsu et al. (2015) gives a silica / water ice mixing ratio of 150 – 3500 ppm in the material ejected from the plume into the E ring. This number is based on the assumption that all nanograins detected by CDA are made of silica, although the composition can only definitely be assessed for a fraction of them. In this sense, the mixing ratio given above represents an upper limit. Note that this population is different from the nanograins observed directly in the plume by CAPS (section 3.4).

Tables 4 and 5 give an overview on the E ring composition near Enceladus estimated from CDA data. Table 5 also shows how concentrations inferred in the E ring might be extrapolated to plume composition. The entries in Table 5 do come with some caveats, as described in the caption. An additional ambiguity is introduced, but not considered in Table 5, because CDA is not sensitive to grains below ≈ 0.2 μm in the E ring or the plume, yet CAPS measurements show that these small grains are present (section 3.3). This situation becomes even more complicated when assessing the overall composition including the vapor, because it is important to consider the different gas / solid mass ratios in the plume and in the E ring. In the plume this ratio is about 10 (section 8.1). However, only ≈ 10% the grains escape the plume (Porco et al. 2006, Spahn et al. 2006, Schmidt et al. 2008, Kempf et al. 2010, Ingersoll & Ewald 2011, Porco et al. 2017), increasing the gas / dust ratio injected into the E ring to ≈ 100.

Table 4. *Abundances of main ice grain Types as identified by CDA in the E ring and their non-water constituents (Hillier et al. 2007, Postberg et al. 2008, 2009a, 2009b, 2011a, 2018). Valid for particle radii for which the composition can be assessed by CDA (≈ 0.2 – 2 µm). The fraction given in the table is size dependent because in larger grains Type I become less frequent while the other two become more frequent. The abundances of the different Types thus also depend on the minimum size threshold detectable by CDA, which again depends on impact speed and instrument settings. Stream particle nano grains actually do not belong to the E ring in a dynamical sense. However, their E ring origin was indirectly determined by Hsu et al. (2011, 2012).*

	Type I	**Type II**	**Type III**	**Stream particle nano grains**
Number fraction	**60 – 70 %**	**20 - 30%**	**≈ 10%**	**-**
Main non-water constituent (MNWC)	**Na, K**	**Organic**	**Na and K salts**	**SiO_2**
Typical MNWC concentration in individual grains	**< 0.0001%**	**0.000001 – 10%**	**0.5 – 2%**	**high**

Table 5. *Integrated abundances of constituents found by CDA in the E ring. These estimates require some assumptions. It is assumed that all compositional types have a similar ion yield when impinging CDA and that Type II and III grains are on average more massive than Type I grains by a factor of 5. The organic fraction is calculated based on the assumption that most of the organics emitted into the E ring reside in a specific sub population that show extraordinary high organic concentrations up to the percent level (Postberg et al. 2018). An average organic concentration of 0.5 - 5% in these grains was assumed. The actual detection frequency of this grain subtype in the E ring varies between 1% and 3% (Postberg et al., 2018). These two factors determine the uncertainty for organics given in the table. The number for SiO_2 from stream particles is taken from Hsu et al. (2015) and constitutes an upper limit as explained in the text. The water abundance is inferred from the abundances of the non-water constituents and neglects the possibility that there might be further compounds not seen by CDA. In this sense the value is an upper limit.*

	Water ice	**Organic material**	**Na and K Salts**	**SiO_2**
Concentration in E ring solids	**99.0% – 99.9%**	**0.01 – 0.3 %**	**0.1 – 0.4%**	**0.015% – 0.35% (upper limit)**
Concentration in plume solids	**decreasing**	**increasing**	**increasing**	**similar (?)**

3.2 CDA measurements inside the plume

The compositional types identified in E ring ice grains are also found in the plume. Modeling of the plume indicates that the plume is stratified in grain size (Schmidt et al., 2008), which was observed by VIMS (Hedman et al., 2009) and the HRD subsystem of CDA (Kempf et al. 2008). So it is naturally interesting to see if this dynamical stratification comes along with a compositional stratification. Normally the CDA's maximum cadence of spectra transmission (< 0.6/s) does not allow measurements with high spatial resolution in the plume. In 2008 a special modification to the CDA's processing software was made to allow a spectra transmission rate of up to 5/s for a short time. However, the mass resolution and the mass range of the CDA had to be reduced to accommodate this increased transmission rate. The new mode was successfully executed during the highly inclined E5 flyby with a relative speed of 17.7 km/s. The result is shown in Figure 6. Each data point of the profile can be compared with the highly inclined spacecraft trajectory shown in Figure 7.

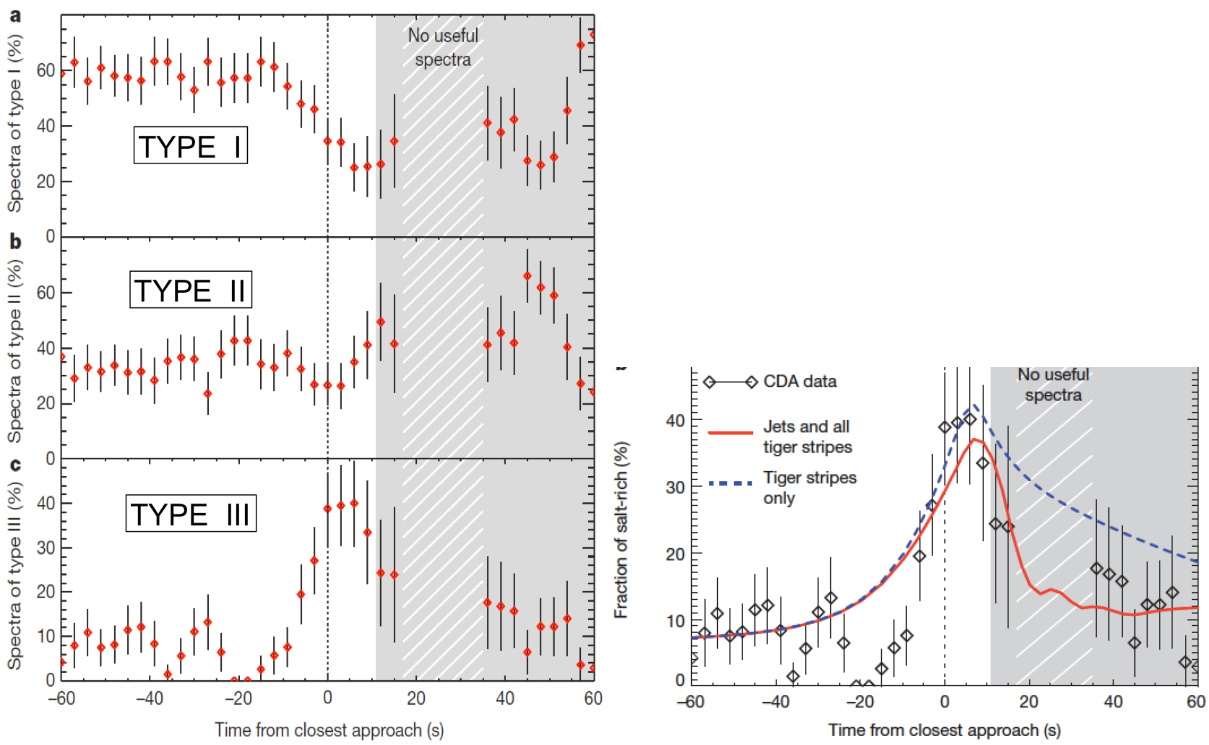

Figure 6: *The compositional plume profile during E5 (modified from Postberg et al. 2011a). Left panel: The relative frequencies of the compositional grain types (I, II, and III) are plotted. Each data point represents an interval of ±4 seconds and includes ~40 spectra (≈ 5/sec) before closest approach and slightly less afterwards. Error bars are one standard deviation from the mean derived from counting statistics. CDA continuously recorded at its maximum rate, therefore the measured frequencies reflect proportions and not absolute abundances. During the period of highest impact rate between ~18 s and ~35 s after CA, too few useful spectra were obtained (hatched region) due to the overload of the instrument. Similarly, unspecified selection effects may have led to fluctuations in the statistics starting from ~11 s after closest approach. Although the data obtained during this time interval (grey) may therefore have been affected by instrument performance issues, they exhibit a stable trend matching the model predictions of Postberg et al. (2011a) shown on the right panel.*

Right panel: Compositional profile of Type III grains with overlaying contours obtained from two models. The dashed line shows a modelled uniform particle flux emerging from all four tiger stripes. The solid line shows a model including eight faster and more collimated jet-like particle sources observed by Spitale & Porco (2007). The contribution from the small jet particles helps fit the rapid decrease of salt-rich grains when the spacecraft was entering the densest part of the plume, starting about five seconds after closest approach. The model fit including fast sources is also considerably better in matching the relatively low level of Type III grains after 40 s from closest approach, when *the spacecraft was still within range of the jets. The background flux of E ring grains is also part of the model. It dominates until about ten seconds before closest approach.*

Figure 6 shows that on E5 near closest approach (CA) to Enceladus (21 km) the proportions of the three main types exhibited significant variations.

a) a steep increase in salt-rich Type III grains from near zero shortly before CA to a maximum of >40% a few seconds after CA and a subsequent shallower decrease towards the dense plume.

b) a corresponding simultaneous decrease in the Type I grain proportion with respect to the E ring background shortly before CA.

c) a less pronounced increase in the proportion of Type II grains after CA with a subsequent sharp maximum between +45s to +51s.

The most plausible explanation for the simultaneous increase of Type III and decrease of Type I proportions in the fringe region of the plume (Figure 7) is that salt-rich grains are ejected at slower speeds than salt-poor grains: The slow Type III grains are dominant at low altitudes, whereas the faster Type I grains enriched at higher altitudes and in the E ring but depleted close to Enceladus. In contrast, the increased ratio of organic-containing Type II ice grains in the core region of the plume, does not seem to depend on altitude and thus ejection speed.

Postberg et al. (2011a) suggest that different size distributions of Type I and III grains are responsible for the different ejection speeds implied by the measurements. As a consequence of the radius-dependent friction force that a grain experiences when accelerated by a gas in a subsurface ice vent (Schmidt et al., 2008), ejection speeds of particles are size dependent. This size dependence leads to the observed tendency of large particles preferentially populating the lower regions of the plume (Kempf et al. 2008, Hedman et al. 2009). Figure 6 (right panel) shows the model fits to the E5 data, assuming size dependent ejection speeds in a uniform particle flux emerging from all four tiger stripes. It qualitatively reproduces the rise in the fraction of salt-rich grains around closest approach. An even better match could be achieved if the eight faster and more collimated jet-like particle sources known at that time (Spitale & Porco, 2007, Hansen et al., 2008) were added to the uniform flux. These jets are modelled with a steeper particle size distribution, which therefore are richer in small grains compared to the slower uniform particle flux, and, in this model, are preferably salt poor (Postberg et al., 2011a). Figure 7 shows a graphical representation of the modelled plume including the jets and the E ring background.

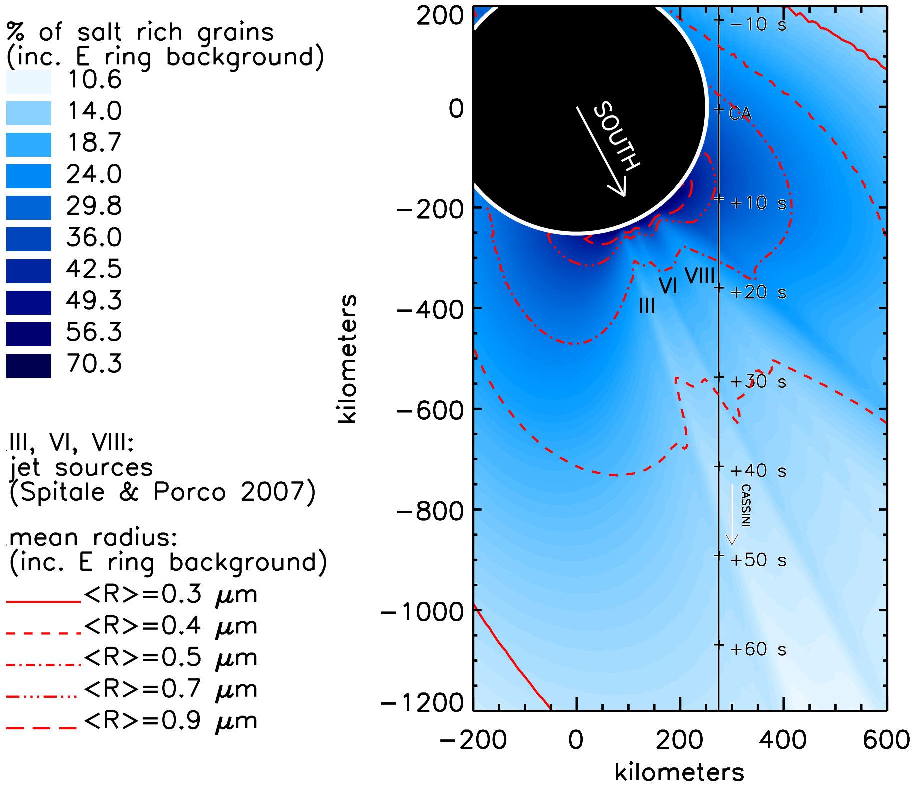

Figure 7: *Graphical representation of the model plume, including the E ring background, as derived from the E5 flyby data (modified from Postberg et al., 2011a). The background colors on the left panel show the modelled proportion of salt-rich grains (Type III). Pure water ice (Type I) and organic bearing grains (Type II) are subsumed as salt-poor in this model. Overlaid are contours of constant mean particle radius obtained from the model. The projection used is in the plane of the E5 spacecraft trajectory (solid black line, shown with 10 s intervals). It is expected to see both the largest particles and the highest fraction of salt-rich grains, a few seconds after closest approach to Enceladus. Structures of the three most relevant localized supersonic jets for this projection are clearly visible in both the compositional profile and size contours. Note that the model only considers particles with radii above the estimated instrument's detection threshold ($r \geq 0.2$ μm).*

The profile of organic-bearing Type II grains does not seem to follow a trend where speed and size are linked to composition as in the case of Type I and III grains. Their proportion is slightly higher in the dense plume compared to the plume fringe region, in which the Type III maximum of E5 lies (Figure 6, left panel). This implies a general enrichment of ice grains containing organic material that could be associated with fast, collimated jets (Postberg et al., 2011a). A second significant increase of Type II grains between 45 and 51 seconds after closest approach coincides with the passage of jet source III identified by Spitale & Porco (2007). This event also coincides with the time where Cassini's ground track lies over the Tiger Stripe fissure called Damascus sulcus and indicates a passage through a region significantly enriched in organic-bearing ice grains. The short timing of this Type II increase only agrees with a very collimated jet source with an opening angle of about 10° because the spacecraft was already 600km above the surface at that point (Fig. 7). The implied organic rich emission from Damascus sulcus is supported by VIMS observations of surface deposits that show the strongest organic absorption at 3.44μm (Brown et al. 2006) on Enceladus around Damascus sulcus (section 6). Moreover, plume grains emerging from Baghdad and Damascus sulci show IR features in VIMS spectra not observed in emissions of the other two fractures (section 3.4).

The high rate spectra recording mode employed during E5 turned out to be a risk to the CDA instrument's health and safety and therefore could not be used again. Despite the limits in detection rate other attempts to map the plume stratification were done during E17, E18 in 2012 and E21 in 2015. Here the maximum spectral recording rate was limited to approx. 0.6/s, about ten times lower than during E5. Unlike E5 the trajectory of all three flybys were not inclined and led Cassini almost horizontally over the south polar terrain. The flyby speeds were less than half of E5: 7.5km/s on E17 and E18 and 8.5 km/s on E21. In terms of spatial resolution, the lower speed partially compensated for the lower detection rate.

In contrast to E5, where the spacecraft trajectory was perpendicular to the Tiger Stripe fractures, Cassini flew almost parallel to these surface features during E17 and E18 (Figure 8). With a mean anomaly of 146° (E17) and 153° (E18) the position in Enceladus' orbit was also very similar. Of these three low velocity flybys, E17 yielded the data set with the highest quality. The compositional profile of E17 (Khawaja et al., 2017) is shown in Figure 8. When entering the plume from the E ring background, the proportion of Type 1 goes down, whereas the proportions of the other two groups go up. However, the increase in the proportion of Type III grains is much less pronounced than in E5 reaching ≈ 18% around the closest approach (≈ 7 % in the E ring), whereas at the same time the Type II proportion reaches 55% (starting from ≈ 30% in the E ring).

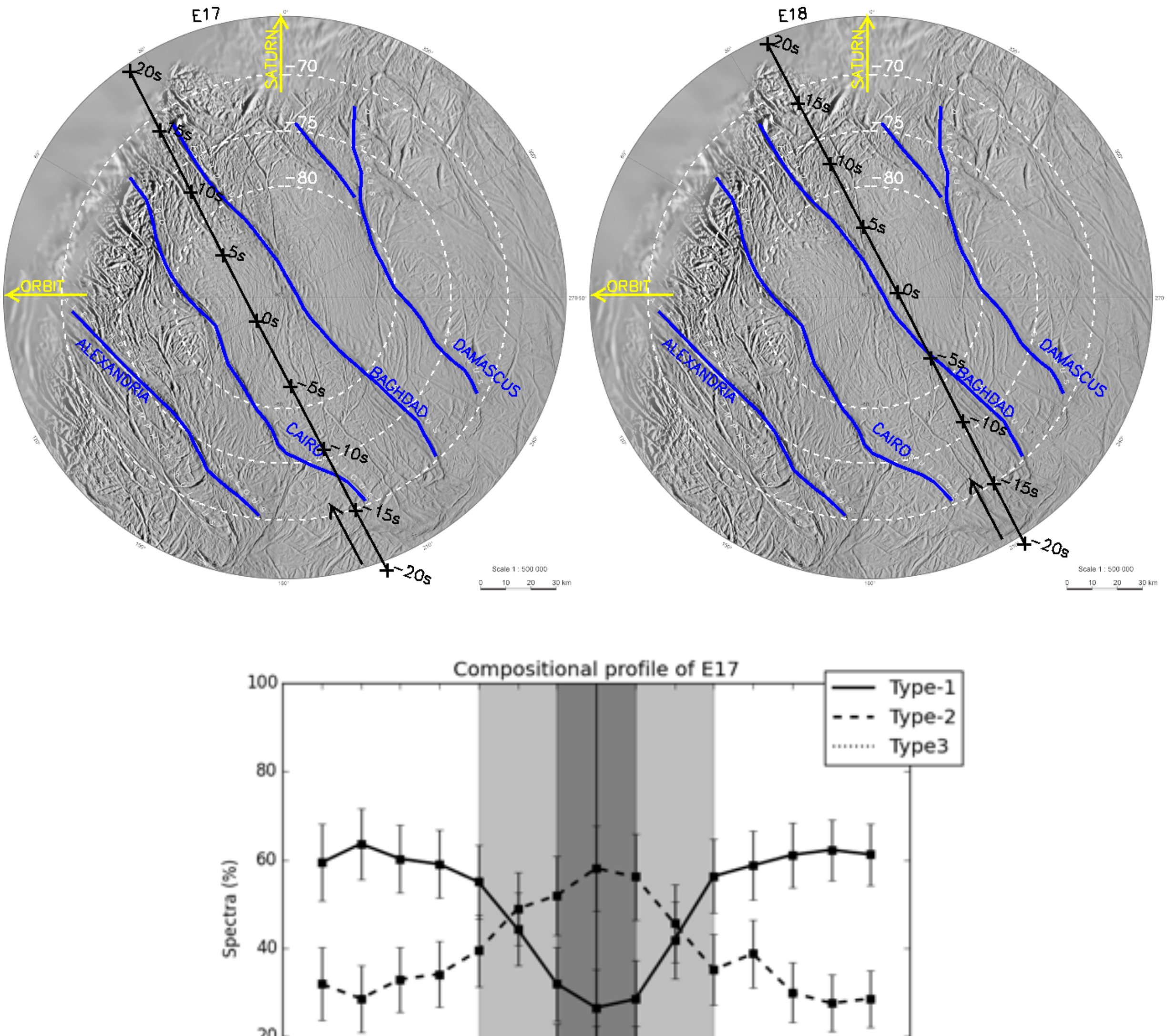

Figure 8: *Upper panels: The trajectories of E17 and E18 are similar. The ground tracks of the spacecraft trajectories (black lines) are marked by time interval with respect to the time of closest approach. Closest approach was at 76 km in both cases. Lower panel: The compositional profile of E17. The grey area indicates the region where plume particles are more abundant than the E ring background. The dark grey area marks the period when Cassini was directly over the South Polar Terrain (below -70° latitude).*

The domination of Type II grains in the plume on E17 might only be reconciled with the E5 findings when a general enrichment of these organic bearing grains inside a large number of fast jets is assumed, which, at the same time, suppress the Type III proportion that are ejected from slower sources. Efforts are ongoing to modify the E5 model in a way that it can be reconciled with the E17 data. Compositional plume variations in time, between E5 (in 2008) and E17 (in 2012), might also be a factor.

3.3 CAPS Measurements on Nanograins in the Plume

Two subsystems of the Cassini Plasma Spectrometer (CAPS), the Ion Mass Spectrometer (IMS) and the Electron Spectrometer (ELS) (*Young et al*., 2004) frequently observed a population of charged nanograins in the Enceladus plume (Jones et al 2009). The principle of operation of ELS allows the detection of negatively charged nanograins, their energy per charge (as ELS uses an electrostatic analyzer) and direction, using a microchannel plate (MCP). For the Enceladus encounters, the flyby speed may be used to determine the mass per charge via a conversion involving that speed. In the case of IMS, there is an additional linear electric field time of flight (TOF) determination of mass, beyond the input electrostatic analyzer, which operates similarly to ELS. Most of the results here refer to the analysis of 'START' MCP pulses beyond the IMS electrostatic section.

With a mass to charge ratio $m/q \sim 10^3$ to 10^4 u/q the detected grains are inside the mass-gap between neutral and charged molecular species (sections 2 and 4) and larger, macroscopic ($r > 0.2\mu m$) solid ice grains observed by CDA (section 3.1 and 3.2) and VIMS (section 3.4) (Figures 9 and 13b). During plume traversals the CDA is not sensitive enough to detect such small grains and CAPS is the only instrument capable of observing this sub-population in the plume. In contrast to the hyper-velocity SiO_2 nanograins observed by CDA in Saturn's magnetosphere, the nanograins in the plume are generally assumed to be of icy composition by comparison with the compositional analysis of gas (Hansen et al. 2008, 2011, Waite et al. 2017, section 2), ions (Coates et al. 2010a, 2010b, section 4) and larger grains observed by the CDA (Postberg et al. 2011a, section 3.2). Thus the icy composition of nanograins is mainly based on plausibility arguments but not on direct measurements.

The nano-particles are charged both negatively and positively and dominate the energy spectra at ~1 keV and higher in the regions in which they are seen. Jones et al. (2009) suggested that triboelectric charging during the plume emission process could provide the charging mechanism. Detailed comparison of the observed fluxes with known jet emission sites gave a good correspondence, and the oppositely charged species were seen to deflect in Saturn's electric and magnetic field.

The charged nanograin analysis of these heavy species (up to about 30,000 amu/q, corresponding to ~2000 H_2O molecules) was further pursued by Hill et al (2012). On this basis they suggest that most of the grain charging occurs in the plume itself via electron impact. They also argued for single charge on the grains. The measured density of negative and positive nanograins near Enceladus is shown in Figure 9(d) from Hill et al. (2012) and indicates that negative nanograins are clearly dominant near Enceladus.

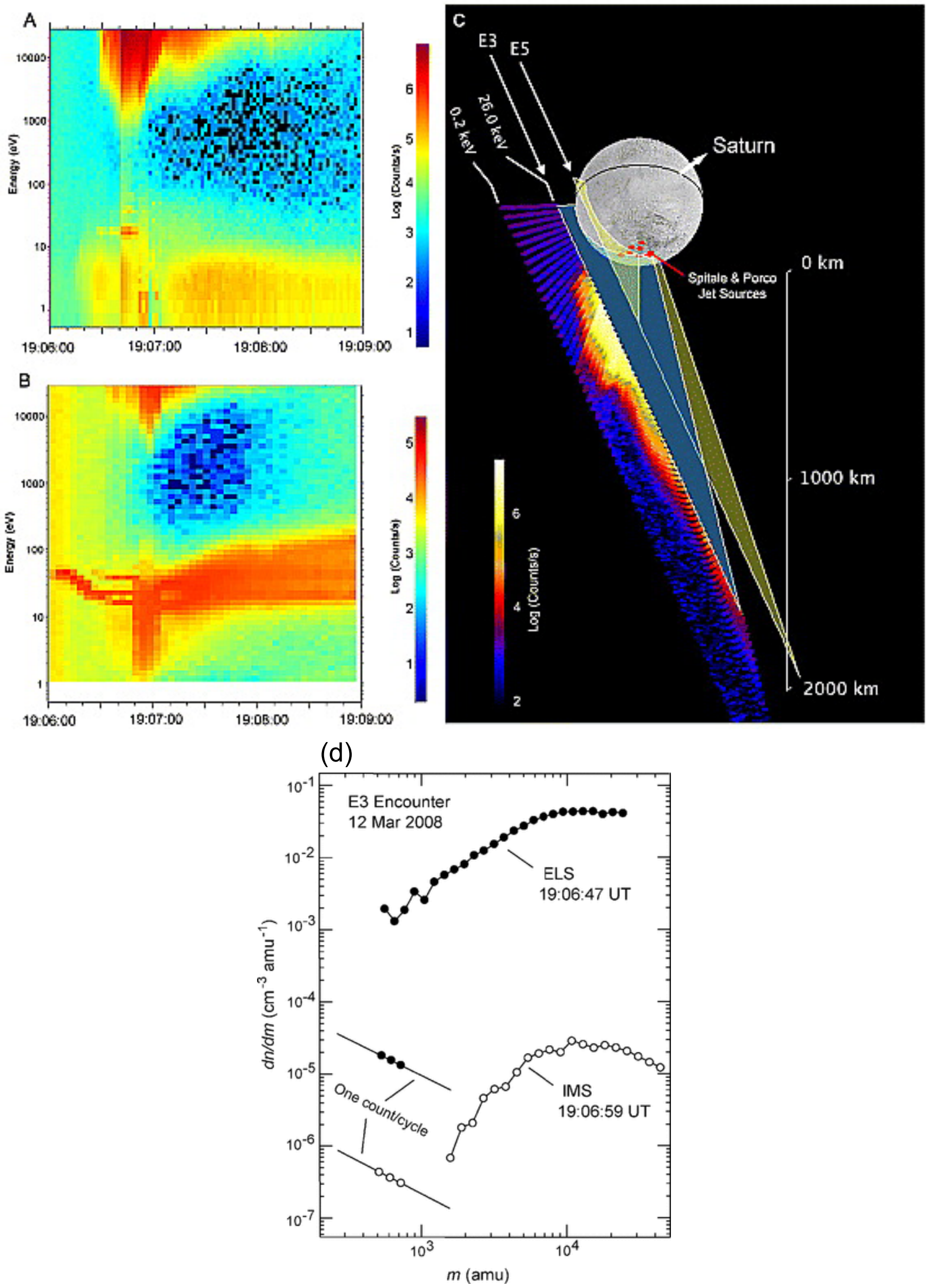

Figure 9 – *(a) ELS and (b) IMS spectrograms showing charged nanograins (high energy signals) during the E3 encounter; (c) E3 and E5 trajectories with ELS nanograin data superimposed and compared with the Cassini ground track (from Jones et al., 2009). (d) shows the calculated density of negative (ELS) and positive (IMS) nanograins showing the dominance of negatively charged grains (from Hill et al., 2012).*

Charged nanograins can easily escape Enceladus' gravity field on trajectories bent by Saturn's co-rotating electromagnetic field (Hill et al. 2012, Dong et al. 2015) and can provide a significant source of material for the Enceladus torus and for the E ring. If one uses the (uncertain) negative and positive nanograin densities from Hill et al. (2012) and assumes a grain speed of ~500 ms^{-1} over an area πR_E^2 and an average mass of 10,000 amu, then an approximate mass flux of negative and positive charged nano-phase dust grains of 5.6 kgs^{-1} can be estimated which is a mass flux comparable to those of grains with $r > 0.6\mu m$ (Kempf et al., this volume). Dong et al. (2015) further analyzed the CAPS nanograin data and combined them with CDA and RPWS observations to provide a composite size distribution. This model distribution was based on fitting a composite dust nanograin size distribution peaking at ~2nm to the other observations. From these fits, the total mass production rate of all grains was found to be ~20% of the INMS water vapor mass density at ~15-65 kgs^{-1} the majority of which resides in grains with radii below 100nm. However, this estimate is controversial because it assumes a continuous size distribution between grains of a few nanometers in size up to micron -sized grains, which is ambiguous as Cassini's instruments do not well constrain the size distribution for radii between 4 nm and about 1 μm (Dong et al., 2015). Recent calibration experiments indicate that Dong et al (2015) drastically underestimated the nanograin detection efficiency of the CAPS sensor. If this underestimate is verified, the flux would go down by a factor of 10 – 20 to not more than a few kg/s. In any case the mass flux of nanograins could be close to the mass flux of macroscopic ice grains escaping into the E ring and would therefore be an important source of matter into the E ring and Saturn's magnetosphere. For a detailed discussion see Kempf et al., this volume.

3.4 VIMS measurements of the plume

Information about the plume ice particle composition can also be derived from remote-sensing spectral data. Challenges associated with these sorts of measurements are that the plume has a low optical depth and the plume particles are strongly forward scattering. The former means that the plume spectra have low signal-to-noise ratios while the latter means that the observations with the highest signals do not typically exhibit strong absorption signals. Indeed, the only clear spectral feature in near-infrared plume spectra is a dip at three microns that is due to the extremely strong fundamental water-ice absorption band. Thus far, no other component than water has been securely detected in near infrared plume spectra, although efforts are ongoing.

While the CDA data contains much more information about the chemical composition of plume particles, the VIMS spectral data provide important constraints on the physical structure of the ice grains. For example, the position of the band minimum depends on whether the ice is in an amorphous or crystalline state, and the observed spectra indicate that the plume particles consist primarily of crystalline water ice (Figure 10). This crystalline state implies that the grains formed at temperatures above 130 K, which is consistent with other evidence that the plume sources are rather warm. Further studies of the spectral and photometric properties of the plume particles could also reveal whether the plume particles are compact grains or loose aggregates of smaller particles.

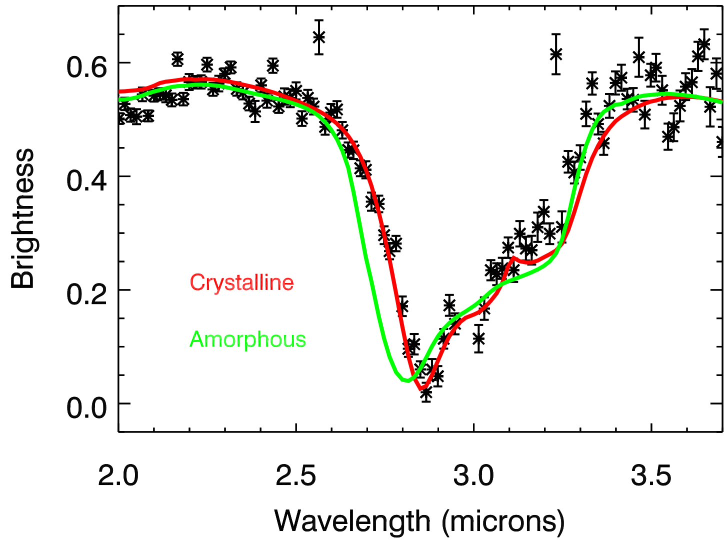

***Figure 10 (Adapted** from Dhingra et al. 2017): Character of ice in Enceladus' plume. Mie-theory based model spectra for crystalline and amorphous ice compared with plume spectra collected with the VIMS instrument onboard Cassini. The VIMS spectra are best fit with a crystalline water ice spectrum.*

VIMS solar occultation data obtained in 2010 together with UVIS measurements show that the plume material above Baghdad and Damascus sulci has a dust-to-gas mass ratio that is roughly an order of magnitude higher than the material above Alexandria and Cairo sulci (Hedman et al. 2018). The highest-resolution near-infrared spectral data obtained by VIMS can resolve material coming from three of the fissures, allowing spatial variations in plume particle properties to be detected (Figure 11). The ice grains emerging from Baghdad, Cairo and Damascus sulci all show a strong three-micron water-ice absorption band with a band minimum position consistent with primarily crystalline water ice. However, the detailed shape of this band, as well as the spectral slope at shorter wavelengths, does differ from fissure to fissure. In particular, the spectra of the Cairo material seem to be distinct from those of the material emerging from Baghdad and Damascus. This observation almost certainly reflects differences in the particle size distributions of the material erupted from the different fractures, but it could also imply variations in the structure and compositions of the grains emerging from the different sources (Dhingra et al. 2017). The high amount of organic bearing grains observed by CDA when flying over Damascus during the E5 flyby (Postberg et al., 2011a) (section 3.2) might also reflect these compositional differences.

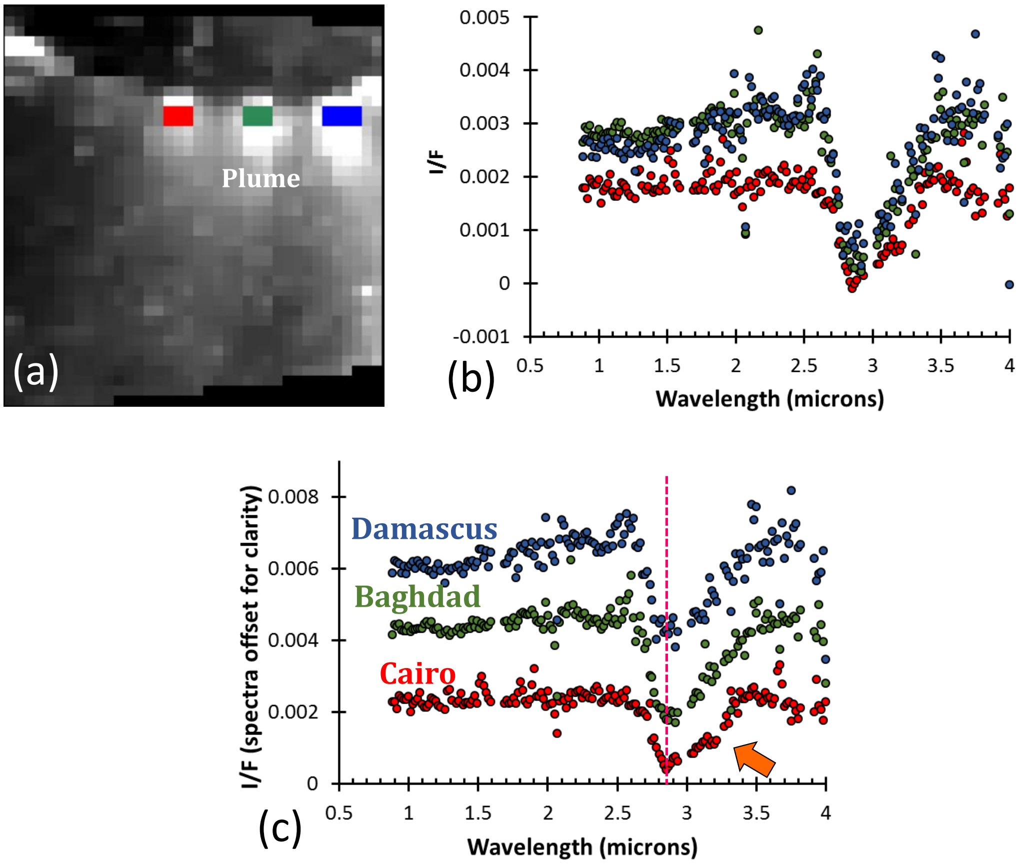

Figure 11: *Spatial variability in the near-IR spectral properties of Enceladus' plume. (a) Spatially-resolved VIMS observation of Enceladus' plume from the E10 encounter (cube: V1652853941). Red, green and blue regions indicate sampled regions in the plume and correspond to eruptions along Cairo, Baghdad and Damascus tiger stripes. Colors correspond to the spectra shown in b and c. (b) Spectral character of eruptions along individual tiger stripes. Note the differences in the spectral slope between 1-2.5 µm. (c) Same spectra as in b but vertically offset for clarity. Note the spectral asymmetry (bump) present in the Cairo spectrum (indicated by an orange arrow), which is not observed in spectra from Baghdad and Damascus. Similarly, a spectral bump around 2.6 µm is only apparent on Baghdad and Damascus. The magenta dotted line indicates the band minimum position, which is the same for all three spectra and indicates crystalline water ice grains in the plume. Uncertainties on individual data points are not plotted for the sake of clarity. Sizes of error bars are typically comparable to those of the symbols, but they vary with wavelength. (See Dhingra et al. 2017 for further details on the uncertainties associated with these spectral observations).*

4 COMPOSITION OF CHARGED PARTICLES

Two of Cassini's instruments assessed the composition of charged particles emitted by Enceladus. The positive ion composition was determined by the Cassini Plasma Spectrometer (CAPS) Ion Mass Spectrometer (IMS, *Young et al*., 2004), which has a time of flight sub-system. The principle of operation of Electron Spectrometer (ELS) allows the detection of negatively charged species, their energy per charge (as ELS uses an electrostatic analyzer) and direction, using a microchannel plate (MCP). Measurements have been performed from inside the plume as well as from escaping material in Saturn's magnetosphere. The analysis of charged species in the magnetosphere has also been pursued using the Charge Energy Mass Spectrometer (CHEMS) sensor of the Magnetospheric Imaging Instrument (MIMI).

In general, the sensitivity of Cassini instruments to minor species in ionized form is lower than for neutral molecules or macroscopic ice grains. In fact, only the measurements in Saturn's magnetosphere allowed for long enough integration times (months to years) to unambiguously identify non-water constituents. In some cases, quantification was possible, nicely complementing the neutral gas and solid grains compositional measurements of Enceladus' plume material.

4.1 CAPS Measurements of Charged Molecules in the Plume

The discovery of the Enceladus plume via the magnetic field deflection (Dougherty et al., 2006) and subsequent Cassini measurements (Spahn et al. 2006, Hansen et al. 2006, Porco et al., 2006, Waite et al. 2006) provided the impetus to determine the plasma and neutral interaction and composition of the plume. The first ion measurements were presented by Tokar et al. (2006) who analyzed the plasma flow around Enceladus. The measured deflection was initially compared to models developed for Io (Hill et al., 1998). The initial estimate for the total plasma mass loading rate was ~3 x 10^{27} H_2O s^{-1}, corresponding to ~100 kg s^{-1}. The positive ion composition near the plume was found to be dominated by water group ions including O^+, OH^+, H_2O^+ and H_3O^+. The presence of H_3O^+ shows that ion-neutral chemistry occurs in the plume as charge exchange is required for its formation and is velocity dependent with slower velocities favoring charge exchange.

The Radio and Plasma Wave Spectrometer (RPWS) and CAPS Electron Spectrometer (ELS) observe a substantial plasma density increase near Enceladus (Morooka et al., 2011, Coates et al., 2013) again indicating that the main mass loading process is charge exchange. Additional ionization processes include electron impact ionization and photoionization. Charge exchange provides energetic neutrals that create an expansion of the Enceladus-related neutral cloud seen as a large-scale OH cloud from the Hubble Space Telescope (Shemansky et al., 1993) and later from Cassini (Esposito et al, 2005).

Further analysis of positive ions in the plume itself was presented by Tokar et al. (2009) using two close Enceladus encounters in 2008, E3 (52 km closest approach) and E5 (25 km). Cold (<10 eV) ions were observed in the ram direction, indicating an almost stagnant plume ionosphere produced from the plume's neutral exosphere. Slowing of the plasma was observed north of Enceladus at some 4-6 Enceladus radii (R_E) away, while south of Enceladus signatures were seen up to 22 R_E away. The composition of the plume ionosphere was again water group (O^+, OH^+, H_2O^+ and H_3O^+) ions and in addition heavier water dimer positive ions were found ($(H_xO_2)^+$) with x=1-4. These heavier ions, predicted by Johnson et al. (1989), may be formed by charge exchange with a neutral dimer from the plume or via ion-molecule interactions in the stagnant plasma. Figure 12a shows a mass spectrum of positive ions in the Enceladus plume ionosphere.

The cold ions in the plume and the low relative speed between the ions and neutrals here indicate that the initial ions are converted to fresh pickup ions via ion-molecule interactions, consistent with the presence of H_3O^+. The ambient ions from the magnetosphere nearby (O^+, OH^+, H_2O^+ and H_3O^+) interact with H_2O in the plume itself giving H_2O^+ and H_3O^+, in a similar process of H_3O^+ production to comets (Cravens et al., 2011). These initially stagnant ions are gradually accelerated and move into the magnetospheric wake. They become the principal source of H_3O^+ for the Saturnian magnetosphere and contribute to the ambient plasma torus, which interacts via charge exchange with Saturn's extended neutral cloud (Tokar et al., 2006) and becomes redistributed through the magnetosphere (Johnson et al, 2006).

In addition to the positive water dimer ions, another remarkable discovery was that of negative water cluster ions in the plume (Coates et al., 2010a). These cold ions were also seen in the spacecraft ram direction and form part of the plume ionosphere. The ions have a short lifetime and were inferred to be constantly produced from H_2O or ice grains in the plume itself. Enceladus thus joins Earth, comets Halley and Churyumov-Gerasimenko, and Titan, as locations where negative ions have been detected. Figure 12b shows a mass spectrum of negative ions in the Enceladus plume ionosphere, while Figure 9 (a)-(c) shows overviews of the CAPS observations.

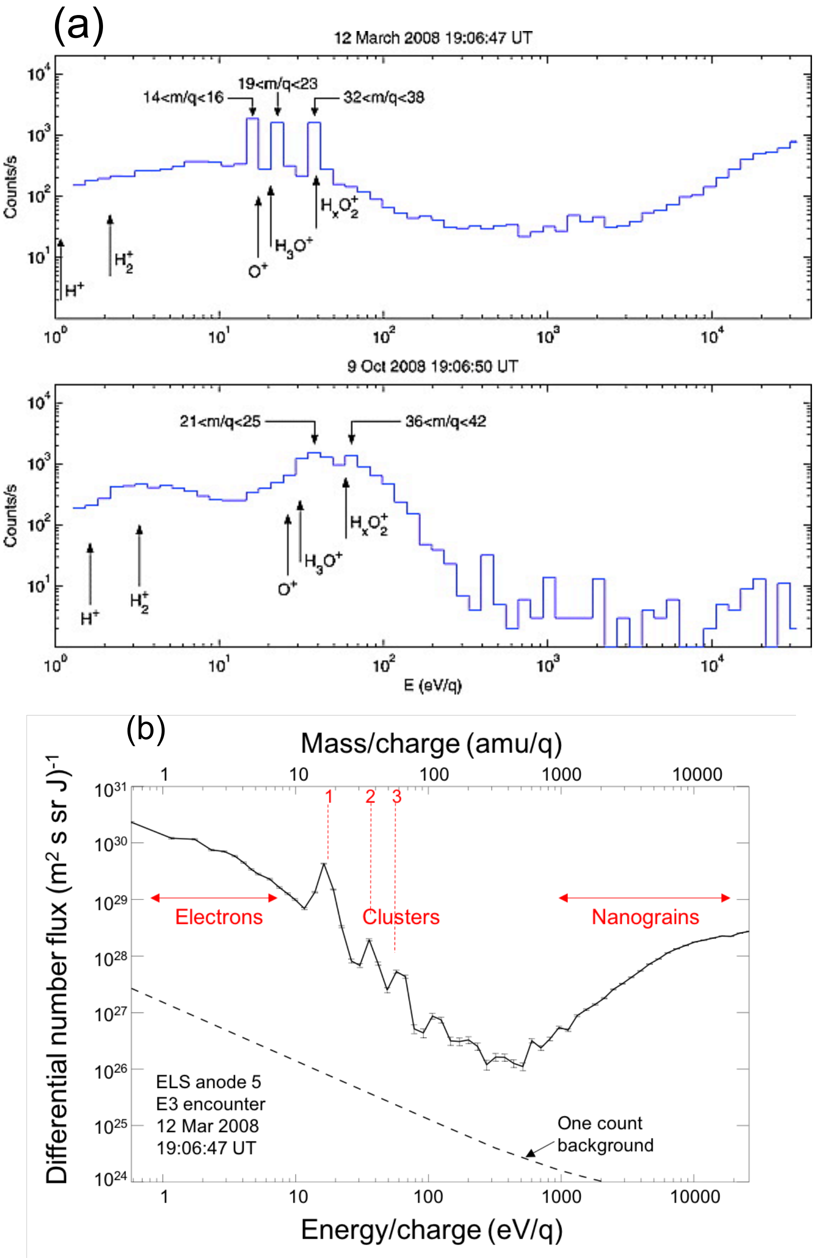

Figure 12 – *(a) Positive ion spectra in the Enceladus plume ionosphere measured during the E3 (top) and E5 (bottom) encounters, showing water group and dimer (with x=4) ion masses (Tokar et al., 2009) (b) Negative ion spectrum measured during the E3 encounter showing*

multiples of m=18 (adapted from Coates et al., 2010a). Nanograins can be seen at the high mass end of the spectrum.

Water-associated negative ions (e.g. OH^-, O^-, H^-) can be produced from H_2O by dissociative electron attachment. Peaks are visible in mass groups 9–27, 27–45, 45–70, 70–300 and 300–500 u/q which may be $(OH)_n^-$ or perhaps $(OH^-)(H_2O)_n$ with n=1,2,3,4…30. Considering the very limited mass resolution of the measurement, the first three peaks are well centered around masses of negative clusters (17u, 35u, 53u). However, the peaks visible in the higher mass groups may include not only water-related clusters, but perhaps more complex carbon-based species such as seen by CDA and INMS (see sections 3 and 5). The density of the negative ions decreased with mass and can reach 50% of the total density of ambient electrons. However, there is also evidence that the highest density of negative species is in the charged dust grains in this region (see section 3.3). A further discussion of the negative ions and comparison with Titan can be found in Coates et al., 2010b.

The complexity of the negatively charged population outside the plume but near Enceladus is presented by Coates et al. (2013). The population includes cold magnetospheric electrons, negative and positive water clusters, charged nanograins, "magnetospheric photoelectrons" produced from ionization of neutrals throughout the magnetosphere near Enceladus, and "plume photoelectrons" from photoionization in the plume. The plume and magnetospheric photoelectrons provide a source of warm electrons with energy >20 eV, which can cause electron impact ionization (>13eV is needed for this ionization). These warm electrons increase the importance of this process in the region near Enceladus and probably throughout Saturn's inner magnetosphere.

The variability of water molecule production rate in the plume was studied using models and Cassini CAPS, MIMI and INMS data by Smith et al (2010) who found at least a factor of 4 variation in the production rate of Enceladus in a 7-month period covering encounters E2, E3 and E5. The results are consistent with variability based on orbital location (Hedman et al., 2013) as mentioned by Blanc et al., 2015 (see also chapter by Smith et al., this volume).

4.2 Compositional CAPS and MIMI Measurements of Ionized Plume Material in Saturn's Magnetosphere

The first measurements by CAPS at Saturn (Young et al., 2005) revealed that the dominant species in the magnetosphere is water group ions (W^+, corresponding to combinations of O^+, OH^+, H_2O^+, H_3O^+). They also reported small concentrations of N^+ between ~3.5-8 R_S indicating that, unexpectedly, something in the inner magnetosphere (rather than Titan, at 20 R_S) was producing the N^+.

Further analysis of the water group population has been performed. The dominance of the W^+ density implied a dominant plasma source within 5.5 R_S (Wilson et al., 2008). A more comprehensive survey of plasma parameters including regions inside Enceladus' orbit (Thomsen et al, 2010) over 4.5 years showed that (1) the ratio of the density of H_2^+ to H^+ is higher near Titan's orbit, indicating Titan as a source of H_2^+, and (2) W^+ ions dominate in the inner magnetosphere within ~3 R_s of the equatorial plane. Arridge et al. (2011) reviewed the published plasma data and concluded that the inner magnetosphere is dominated by low energy electrons and water group ions sourced from Enceladus. Figure 13 shows the densities of various electron and ions species, collected by Arridge et al. (2011).

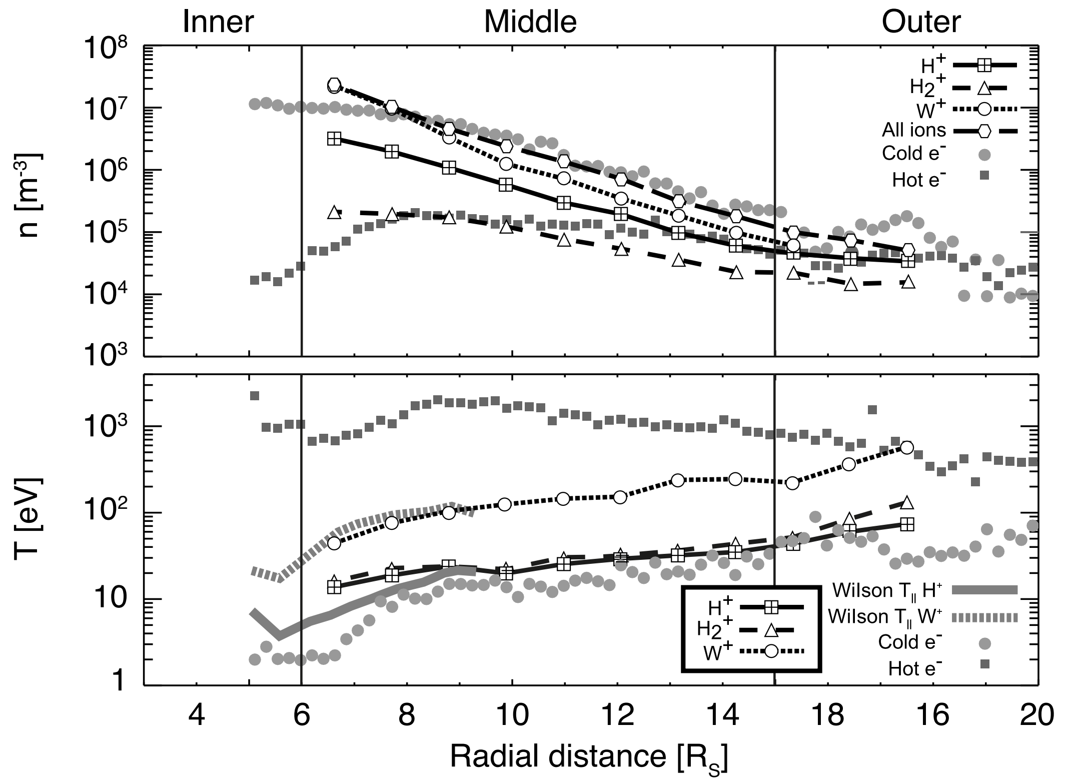

Figure 13 - *Density and temperature in Saturn's magnetosphere from various sources collected by Arridge et al. (2011): (a) number densities of hot and cold electrons (Schippers et al. 2008), and thermal ions (Thomsen et al. 2010); (b) plasma temperatures of hot and cold electrons (Schippers et al. 2008), thermal ions (Thomsen et al. 2010; Wilson et al. 2008).*

Pickup water group ions near Enceladus' orbit were studied by Tokar et al (2008). They suggest that the ions are formed by charge exchange near Enceladus between water group neutrals (O, OH, H_2O) and thermal ions corotating with Saturn. The velocity space distribution of the pickup ions, assumed to be OH^+, is ring-like in velocity space (see section 4.1), indicating that they are relatively new pickup ions. Their density corresponded to ~8% of the total ion density between 4 to 4.5 R_S. Related ion cyclotron waves were studied by Leisner et al. (2006) who found that waves produced by W+ (O^+, OH^+, H_2O^+, H_3O^+) and also O_2^+ were visible throughout the E-ring region.

Further analysis of the nitrogen population has also been pursued by Smith et al. (2005, 2007) who confirmed a source in the inner magnetosphere, although the molecular source (N_2 or NH_3) has not been determined yet. Subsequent work by Smith et al. (2008) using a combination of data analysis and modeling showed that the most likely source is NH_x^+, likely from ammonia, representing a fraction of a few % compared to water ions (see Figure 14). An N_2^+ origin may additionally be present. However, the non-detection by UVIS in the neutral plume gas restricts the N_2 abundance to be below 0.5% of the emitted water vapor (Hansen et al., 2011) and the INMS detects NH_3 in the plume with a volume mixing ratio of 0.4% – 1.3% (see section 2.2). It is currently unclear why charged nitrogen species appear to be more abundant in the magnetosphere compared to what can be supplied by the known nitrogen bearing neutral species. One possibility may be that NH_x^+ species have longer lifetimes than water ions.

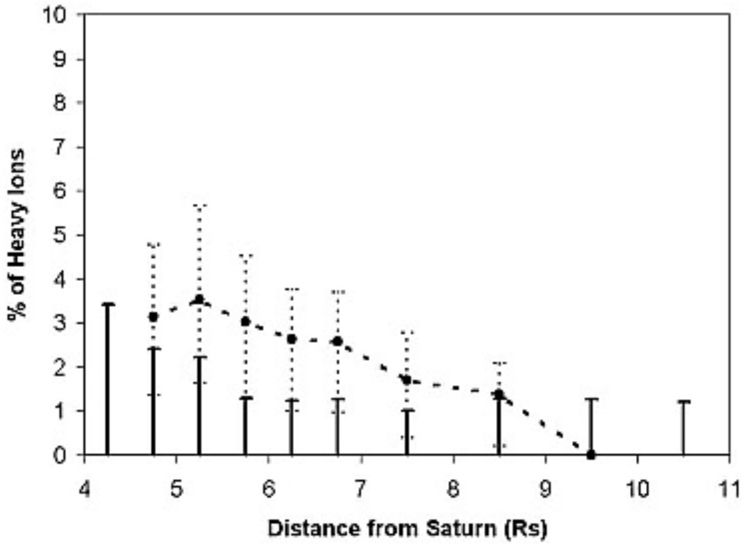

Figure 14 - *Concentrations for N_2^+ (solid black lines) and NH_x^+ (dotted line) from CAPS IMS data. Percentages of all heavy ions are shown as a function of radial distance from Saturn (Rs). For N_2^+ only an upper limit could be inferred. (From Smith et al., 2008).*

The analysis of minor ions compared to W^+ in the magnetosphere with integration times of several years (Figure 15) has also been pursued using the CHEMS sensor of the MIMI instrument (Krimigis et al. 2004), which detects energetic particles in the range 83-167 keV (Christon et al. 2013, 2014). The presence of N^+ (~2% compared to W^+) confirmed the CAPS detection of nitrogen bearing species. Furthermore, C^+ indicates dissociation of abundant organic material in agreement with the organic species found in the plume (section 2 and 3). In particular, Christon et al. (2013, 2014) studied the $^{28}M^+$ (<1% compared to W^+) and O_2^+ (~2%). The main nearby source for the O_2^+ is photolysis of Saturn's main rings, based on the observed seasonal variation that favors a ring-related source. For $^{28}M^+$ the source may be Enceladus or the main rings, and $C_2H_5^+$, $HCNH^+$, N_2^+, Si^+, and CO^+ were suggested as possible species. Further seasonal variations are under study. Christon et al. (2015) studied an ion with mass 56 u with an abundance of ~10^{-4} compared with W^+, identifying it as Fe^+. However, they suggested that this ion may be produced from meteor ablation near Saturn's mesosphere-ionosphere boundary, or perhaps from impacted interplanetary dust particles in the main rings and that Enceladus is probably not the source in this case.

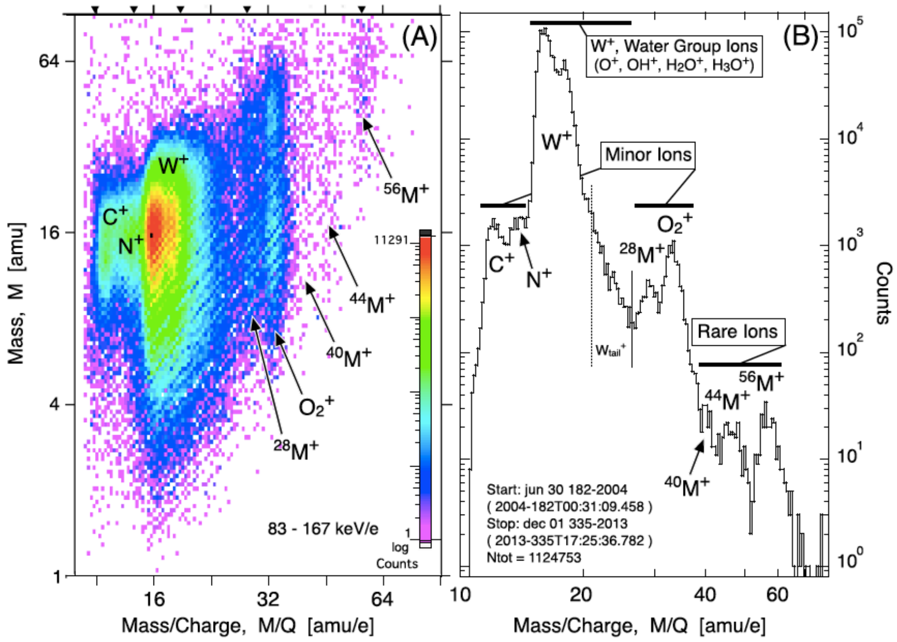

Figure 15 *- From Christon et al. (2015)*
(a) Triple coincidence pulse height analysis events by MIMI-CHEMS measured in Saturn's near-equatorial magnetosphere under certain selection criteria (see Christon et al. 2015) inside of 20 Rs or the magnetopause, whichever is closer to Saturn, from 2004 to 2013 are displayed in a Mass (M) versus Mass-per-Charge (M/Q), color spectrogram. The water group (W^+) (mostly O^+ at 16 amu/e, followed by roughly equal amounts of OH^+ and H_2O^+ at 17 and 18 amu/e, respectively, at about half the O^+ abundance, along with a little H_3O^+), and the minor and rare heavy ion species are identified. C^+ and N^+ are the most abundant non-water species.
(b) Histogram of the data plotted in (a). The histogram permits clearer identification of the minor ions like ^{28}M and O_2^+ and the 'rare group' ions of CO_2^+ ($44M^+$) and iron ($56M^+$) and facilitates qualitative visual comparisons to W^+ and the minor ions.

5. SOURCES OF THE DIVERSE PLUME CONSTITUENTS

5.1. Solid Compounds

The distinct compositional ice grain families probably have very different origins and/or generation mechanisms. The composition of Type III particles matches the composition expected for liquid water within Enceladus (Zolotov, 2007), which has washed out salts from primordial rock inside the moon's potentially porous (McKinnon, 2015) core (Postberg et al., 2009a, 2011a; Hsu et al., 2015). Postberg et al. (2009a) suggest that a spray of droplets is inevitably generated when bubbles reaching the water table of the ocean burst (e.g., Lhuissier & Villermaux, 2012). The bubbles can be formed either from water evaporating close to its triple point or upwelling volatile gases (Matson et al., 2012), like CO_2, CH_4, or H_2. If the spray-droplets are sufficiently small, they will not fall back onto the water table but will be carried by vapour (emerging from the evaporating water) and follow the pressure gradient upwards through the cracks and vents into space (Postberg et al., 2009a). Following this model, Type III grains would be direct samples from the water table of the ocean. From their composition the ocean salinity would be above 0.5%, with NaCl as the most abundant dissolved component followed by about half the amount of $NaHCO_3$ and/or $NaCO_3$ (see the chapter by Glein et al. in this volume).

By contrast, the salt poor (or salt free) Type I grains cannot be generated from ocean spray. Most of these grains are probably produced from vapor condensation (Schmidt et al., 2008, Yeoh et al. 2015). Whether the vapor stems from evaporating ocean-water or sublimated ice makes no noticeable difference in their composition, and both mechanisms are likely to contribute. However, most Type I spectra show traces of sodium ($Na/H_2O \approx 10^{-7}$) that are in good agreement with the traces of salts that one expects to find in the gas phase of evaporating salt water (Postberg et al., 2009a). The observation of predominately crystalline ice grains in the plume (Dhingra et al. 2017 (see Figure 10, section 3.4)) implies that the grains formed at temperatures well above 130 K, which is consistent with other evidence that the conditions in the ice vents are rather warm (see chapter by Goldstein et al. in this volume).

Vapor that rapidly moves upward inside the ice vents condenses to ice grains when narrow passages in the ice channels cause local supersaturation. This process naturally forms smaller grains than the freezing of ocean spray. Compared to the latter, these smaller salt-poor grains are accelerated to higher average speeds (for any given density and speed of the carrier gas) (Schmidt et al., 2008, Postberg et al., 2011a). Homogeneous vapor condensation can also occur during adiabatic cooling after the vapour left the vents. This condensation is limited to altitudes equivalent to 10 – 100 vent diameters (after which the gas becomes collisionless) and produces small grains from nanometer scales up to radii clearly below 1 μm for plausible vent diameters and gas velocities (Yeoh et al. 2015, also see chapter by Goldstein et al. this volume). This scenario is again consistent with salt-poor vapour condensates being preferentially smaller than grains formed from salt-rich ocean spray.

The origin of the organic-enriched Type II grains is the least constrained of the three types. However, their great abundance and frequent detection during Cassini crossings of the Enceladean plume again suggest that Enceladus is their main source (Postberg et al., 2008, 2011a; Khawaja et al., 2017, Postberg et al. 2018). Most of them are salt-poor, in agreement with a formation from condensing vapor. In this case, besides water, initially volatile organic compounds may have condensed onto ice grains as the vapor cooled on its way upwards through the icy channels. A small fraction of grains shows spectral features of Type II as well as Type III. These grains could be frozen salt-water droplets that may have incorporated organic compounds from the Enceladean ocean. Alternatively, organics that initially were in the gas phase could have condensed onto the salty ice grains in the vents.

About 3% of Type II grains exhibit mass lines that stem from organic parent species with molecular masses in excess of 200u in particularly high concentration (Postberg et al., 2018). These organic species are too massive to be in the gas phase at plausible physical conditions above the evaporating water table ($T \leq 0°C$), where the water is inevitably in contact with the ice crust. The refractory organic material has been detected mostly in salt poor ice grains and thus they did not form from the salty ocean spray which preserves the liquid composition. Consequently, the organic material was not dissolved in the ocean water when the ice grain formed. According to Postberg et al. (2018) the most plausible way to generate these ice grains containing abundant high-mass-organics is if the organic material exists as a separate phase, such as a thin film or layer of mostly refractory, insoluble organic species floating on top of the water table. When bubbles burst in such a scenario, they tear apart the organic film and, besides salty water droplets, throw up droplets or flakes rich in hydrophobic organic material (Fig. 16). They will then serve as efficient nucleation cores for ice condensation: droplets ascending in the icy vents become coated by water ice condensing from the vapor carrying the grains (Postberg et al., 2018). These high mass organics species potentially also have been observed by INMS in the plume during high speed flybys, where the high impact velocity of organic-bearing ice grains disintegrated large molecules to organic fragments small enough to show up in INMS limited mass range (< 100 u) (Postberg et al. 2018, see section 2). The observation of unspecified high mass molecular species in the plume by CAPS (Coates et al., 2010a, 2010b) might also be due to large fragment ions from these organic species (see section 4.1 and Figure 12).

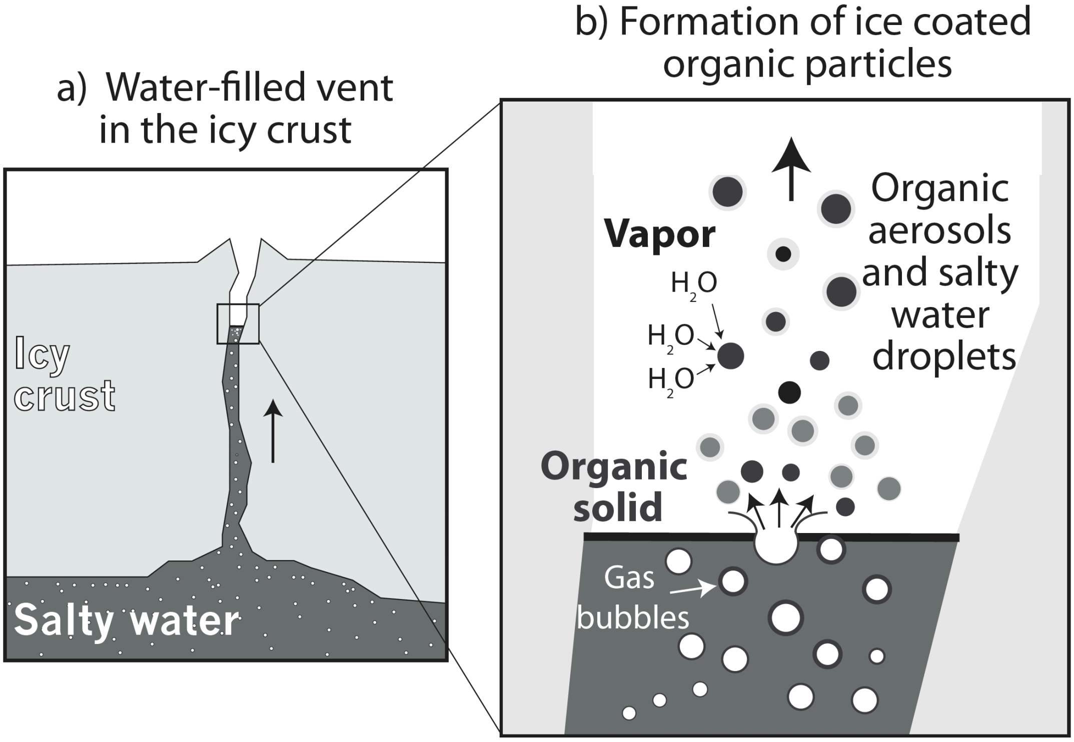

Figure 16

Schematic on the formation of ice grains from heterogenous nucleation (not to scale). From Postberg etal. (2018) with permission from Nature. (a) Ascending gas bubbles in the ocean efficiently transport organic material into water-filled cracks in the south polar ice crust. (b) Organics ultimately concentrate in a thin organic layer on top of the water table, located inside the icy vents. When gas bubbles burst, they form aerosols made of insoluble organic material that later serve as effi cient condensation cores for the production of an icy crust from water vapor, thereby forming HMOC-type particles. Another effect of the bubble bursting is that larger, pure saltwater droplets form, which freeze and are later detected as salt-rich type-3 ice particles in the plume and the E ring. The fi gure implies the parallel formation of both organic and saltwater spray, but their formation could actually be separated in space (e.g., at different tiger stripes cracks) or time (e.g., dependent on the varying tidal stresses working on the cracks) (Hedman et al., 2013; Kite and Rubin, 2016).

The nano - phase silica (SiO_2) grains emitted from the E ring can be interpreted as silica colloids with radii of 2 - 9 nm that formed during the cooling of hydrothermal waters in the subsurface ocean of Enceladus (Hsu et al., 2015). Combined with long-term laboratory experiments, the composition and narrow size distribution of these grains argue for ongoing hydrothermal activities within Enceladus and place constraints on the temperature, alkalinity, and salinity of Enceladus' subsurface waters (Hsu et al., 2015; Sekine et al., 2015). For further details see chapter by Glein et al. in this volume. These nano-particles would be transported from hydrothermal reaction sites, probably located inside Enceladus' porous rocky core to the water table (Hsu et al. 2015, Choblet et al. 2017) and then naturally become inclusions of salty ocean spray from which Type III ice grains form. Nano-silica might also be hovering in the vapor phase above the water table, dragged into ice vents and then become condensation cores for the formation of salt poor ice grains of the Types I and II. Interestingly MIMI-CHEMS observes a species with a mass of 28 u in Saturn's magnetosphere with Enceladus being a possible source (section 3). Besides volatile gases (section 5.2), Si^+ from eroded nanosilica grains might be a source.

Other nano-phase species measured in the plume are charged grains, presumably made of water ice, observed by CAPS (Jones et al. 2009, Hill et al. 2012). These tiny grains inevitably form when the water vapor cools during adiabatic expansion into space (Yeoh et al. 2015, also see chapter by Goldstein et al. in this volume). They quickly become mostly negatively charged after leaving the vents (e.g. Hill et al. 2012, see section 3.3 for details). The CAPS measurements indicate a size of 1 - 3 nm and hence are even smaller than the silica nano grains. Although these grains are invisible in Cassini images, they might be as abundant by mass as macroscopic ice grains (see section 3.3).

5.2 Volatile Compounds

With a mixing ratio above 95%, INMS and UVIS measurements clearly rank H_2O vapor as the most abundant gaseous plume constituent (section 2). A large part likely comes from evaporation of ocean water, close to its triple point, that has hydrostatically ascended inside the 'Tiger Stripe' cracks through most of the south polar ice crust. With an ice shell thickness below 5 km at the south pole (Cadek et al. 2016, Le Gall et al., 2017) the evaporating water table lies less than 1000m below the surface (Postberg et al., 2016) (see chapter by Spencer et al. this volume). Ice sublimation will cause a currently unspecified but substantial contribution to the observed water vapor. Above the water table, ice in walls of the vents is warmed by the ascending gas. Even at the outlets, where the vents reach the moon's surface, ice temperatures reach almost 200K, causing a non-negligible vapor pressure from sublimating ice (Goguen et al., 2013).

Probably the most remarkable volatile plume constituent is H_2, which during E21 has been detected in concentrations exceeding 0.3%. Its extreme volatility precludes "storage" over geological time scales on a small body like Enceladus and suggests that it is currently (or has been very recently) produced inside the moon. Its detection is highly suggestive of ongoing serpentinization reactions in hydrothermal systems within the ocean of Enceladus (Waite et al., 2017). Most importantly the data in Table 2 in section 2.2 allowed Waite et al. (2017) to calculate the chemical viability of H_2 as the chemical energy source in the reaction $4H_2 + CO_2 \rightarrow CH_4 + H_2O$ – a reaction that expresses methanogenic metabolism in Earth's hydrothermal systems. At moderate alkaline pH values, the chemical affinity is positive, thus verifying the habitability of the interior ocean (see chapter by Glein et al., this volume).

Ammonia (NH_3) is detected in the plume in similar mixing ratios (0.4 – 1.3%) as H_2. It is a very reproducible constituent because it has been detected at all occasions when the INMS acquired plume composition and its presence also enhances the spectral fit for UVIS plume spectra (see section 2). The nitrogen-bearing ion species observed in Saturn's magnetosphere (section 4.2) indicate even higher concentrations there. Possible sources for NH_3 are numerous and are poorly constrained from Cassini measurements. For example, it can: 1) form from the dissolving gases in the ocean, 2) be a product of a chemical reaction in the ocean or hydrothermal sites, or 3) be released from clathrates that might reside deep in the icy crust (Kieffer et al. 2006).

Similar considerations are true for methane (CH_4), that has been frequently measured in the plume at concentrations of about 0.2 % (section 2.2). Bouquet et al. (2015) discuss methane contributions from clathrate decomposition as well as hydrothermal production and conclude that both scenarios are viable. Waite et al. (2017) suggest hydrothermal scenarios such as Sabatier or Fischer-Tropsch like processes as well thermogenesis.

Carbon dioxide with a mixing ratio of about 0.5% likely is released when pressurized water saturated in CO_2 ascends from the depth of the ocean. Matson et al. (2012) present a model where dissolved gases, mostly CO_2, exsolves as the water moves toward the surface inside conduits in the south polar ice crust. Bubbles formed by exsolution can decrease the bulk density of the vertical column of water enough that the pressure at the bottom of the column is less than that at the top of the ocean. It is suggested that this pressure difference drives ocean water into and up the conduit toward the surface. CO_2 saturated ocean water would be in good agreement with the substantial concentrations of carbonate salts found in the salt rich ice grains that are suggested to resemble ocean water composition (Postberg et al., 2009a), with more dissolved CO_2 for a lower ocean pH (see chapter by Glein et al., this volume).

The most controversial Cassini observation in the plume gas is the species with a mass of 28 u which could be attributed to CO, N_2, C_2H_4 or even Si (as a cationic species, see below). Both INMS and UVIS measurements now agree that the abundance of CO and N_2 lies below 0.5%. Whereas the latest INMS results exclude any intrinsic plume gas with mass 28 u at a level of 0.1% (Waite et al., 2017), UVIS results indicate at least traces of ethylene (C_2H_4) to be present (Shemansky et al., 2016). These constraints are particularly interesting in the context of a 28 u cation species observed by MIMI-CHEMS in Saturn's magnetosphere (Christon et al., 2014) (section 4.2). However, it cannot be differentiated if this species stems from a gaseous plume compound or dissociated silicates, like silica nano-grains or interplanetary dust (with the latter obviously not being of Enceladus origin).

6. SURFACE COMPOSITION

6.1. Infrared observations

Earth-based telescopic spectra of Enceladus already indicated the presence of water ice (Grundy *et* al., 1999; Cruikshank *et* al., 2005; Emery *et a*l., 2005, Verbiscer *et al.,* 2006). At opposition, the icy surface reflects more than 130% of the visible sunlight (geometric albedo = 1.375 ± 0.008 (Verbiscer et al. 2007), Bond albedo = 0.85 ± 0.11 (Pitman et al. 2010)), which makes Enceladus the body with the highest visible geometric albedo of all bodies in the solar system. The Bond albedo of the trailing hemisphere is higher (0.93 ± 0.11) than that of the leading hemisphere (0.77 ± 0.09) (Pitman et al. 2010). Grundy *et al*., Emery *et al*., and Verbiscer *et al*. reported detecting a weak absorption in the 2.2 to 2.4 μm region indicating a possible presence of NH_3 or NH_3 hydrate, but Cruikshank *et al*. did not detect the feature, and so far, it has not been definitively detected in Cassini's VIMS data with the latest instrument calibration (Clark *et al*., 2016).

Early studies by Cassini VIMS confirmed dominant water ice on Enceladus' surface (Figures 17a, 17b). Trapped CO_2 was found in most locations, including the Tiger Stripe region (Brown *et al*., 2006). Brown *et al*. also reported amorphous ice. However, this early work did not include the effects of diffraction by sub-micron ice grains that are common in the E-ring and in the plume (e.g., Kempf et al. 2008, Hedman at el. 2009, Postberg et al. 2011a, see section 3.4.). The signatures of sub-micron ice grains, probably from E ring deposition in most cases, can be observed throughout the Saturn system (Clark *et al*. 2012). Clark *et al*.

(2012) showed that a radiative transfer model that included diffraction from sub-micron particles modified the spectral structure in a unique way, changing relative band depths and shifting band shapes toward longer wavelengths, and verified the effects with lab spectral of small ice grains. Amorphous ice shifts the bands to shorter wavelengths and changes the shapes differently than sub-micron grains. For further discussion on crystalline and amorphous surface ice see section 7.2.

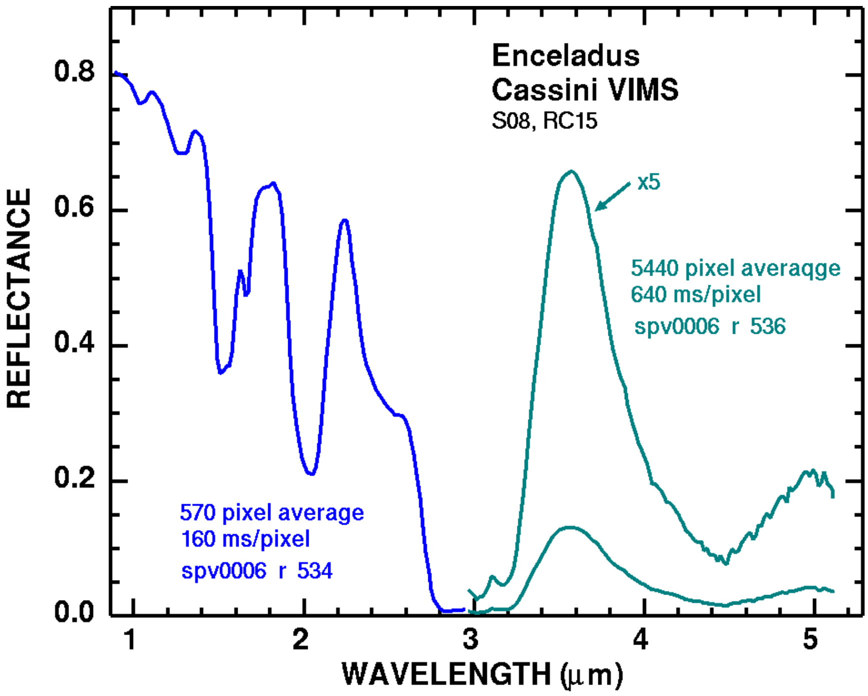

Figure 17a. *VIMS average spectra of Enceladus show the signatures of crystalline water ice at 1.65 µm and 3.1 µm.*

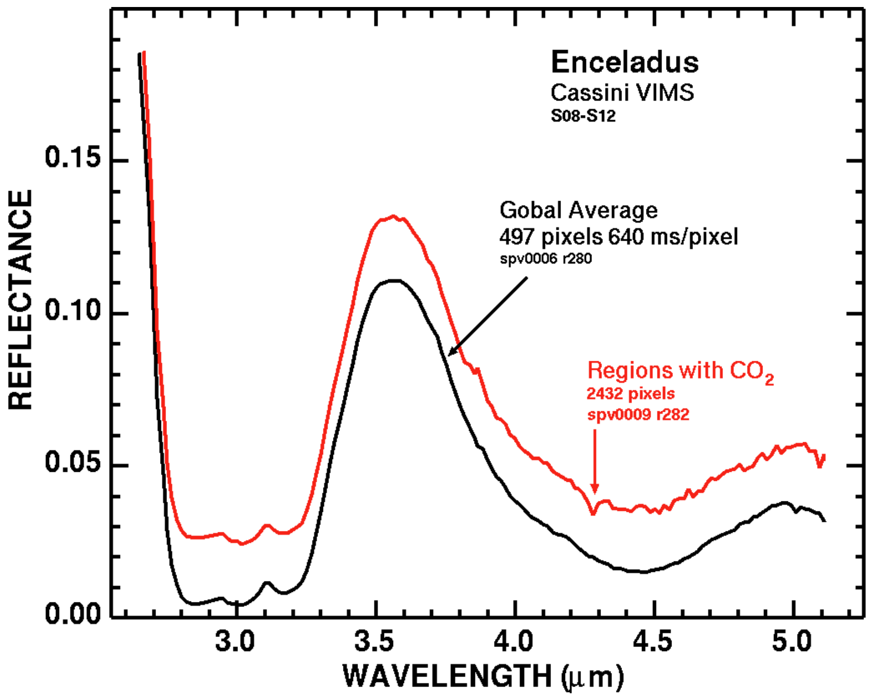

Figure 17b. *VIMS spectra of Enceladus showing crystalline water ice (3.1 µm) and a CO_2 signature in some locations, predominantly in the Tiger Stripe region.*

Jaumann et al. (2008) mapped the grain size of ice across Enceladus' surface and found that the observed ice absorption strengths in Cassini VIMS spectra could be explained by pure crystalline ice of varying grain sizes. They found the largest grain sizes (~0.2 mm) in the south polar "Tiger Stripe" region. Jaumann et al. also found that the particle diameter of water ice grains increases toward younger tectonically altered surface units and the largest particles are found in relatively "fresh" surface material. The smallest ice grains were generally found in old, densely cratered terrains. They also found that the ice grain diameters are strongly correlated with geologic features and surface ages, indicating a stratigraphic evolution of the surface that is caused by plume deposition and distribution of materials from cratering events. A complicating factor in deriving grain sizes in the presence of sub-micron ice grains is that, as tiny ice grains become more abundant, the surface looks more like a block of ice and the absorption band depth increases. Fortunately, the presence of small grains is revealed by the modification of the shapes of the absorption bands (Clark et al., 2012), but a more sophisticated analysis of the spectral properties is needed than a simple calculation of band depth (Figure 18). Jaumann et al. (2008) completed their study before these effects were known. Some of the areas they found with larger ice grain sizes, especially those subject to large amounts of plume 'snow', are definitely affected by sub-micron ice grains and thus need to be re-evaluated. Scipioni et al., (2017) have begun that evaluation and have generally found much smaller grain sizes than Jaumann et al. (2008) and a correlation with plume deposition (see section 7.1 for a details). However, the highest spatial resolution data have yet to be analyzed at the native resolution.

Additional work on the relation between band depth and grain size has been accomplished by Verbiscer et al. (2006) who demonstrated the effects of the photometric or scattering properties of surface particles on absorption band depths. Such analysis is further complicated by the relationship between band depth and phase angle (e.g. Pitman et al. 2017), which needs to be included in any modeling effort.

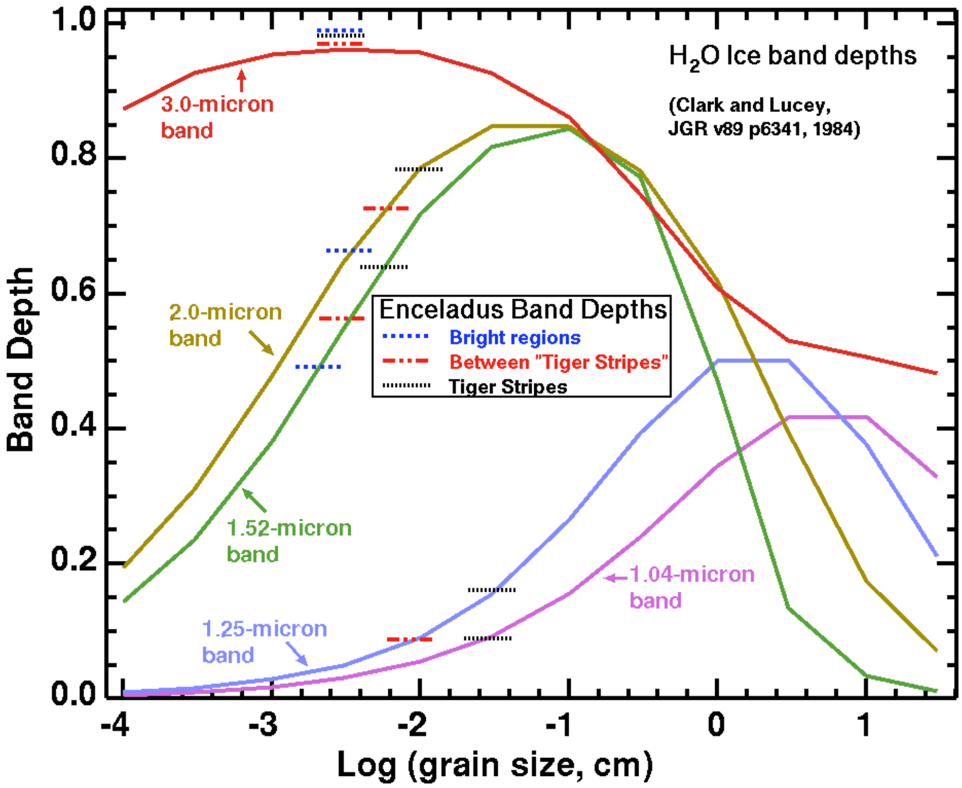

Figure 18. *Ice band depth as a function of grain diameter with band depths observed on Enceladus. This graph does not include photometric effects or the effects of sub-micron ice grains, which will show enhanced band depths as the abundance of such grains increases.*

Derivation of compositional abundances from reflectance spectroscopy requires the identification of the components making up the surface, and a simultaneous solution of the grains sizes and abundances of each component. While water ice dominates Enceladus' surface, Brown *et al.*, (2006) found trace organic compounds in the Tiger Stripe region (Figure 19). The band position of the organics is consistent with aliphatic hydrocarbons, but the signature is weak and a more specific identification could not be made. Detecting the presence of the organic absorptions is made more complex by the spectral curvature in the strong signatures of ice. A more sophisticated analysis than that performed by Brown et al., with the latest VIMS calibration (Clark et al. 2016) needs to be done and might reveal more information on the nature of the organics. However, the signatures of organic trace compounds (Brown et al. 2006) are consistent with the detection of organic bearing ice grains and methane in the plume by CDA (Postberg et al. 2008, 2018) and INMS, respectively, (Waite *et al*. 2006, 2017) that are expected to be deposited primarily near the Tiger Stripes (section 7.1). Brown *et al.*, (2006) also set an upper limit of 2% for solid NH_3 global surface deposits. Hodyss et al., (2009) reported detecting methanol in VIMS spectra from Enceladus' surface but it has not been verified with the latest VIMS calibration.

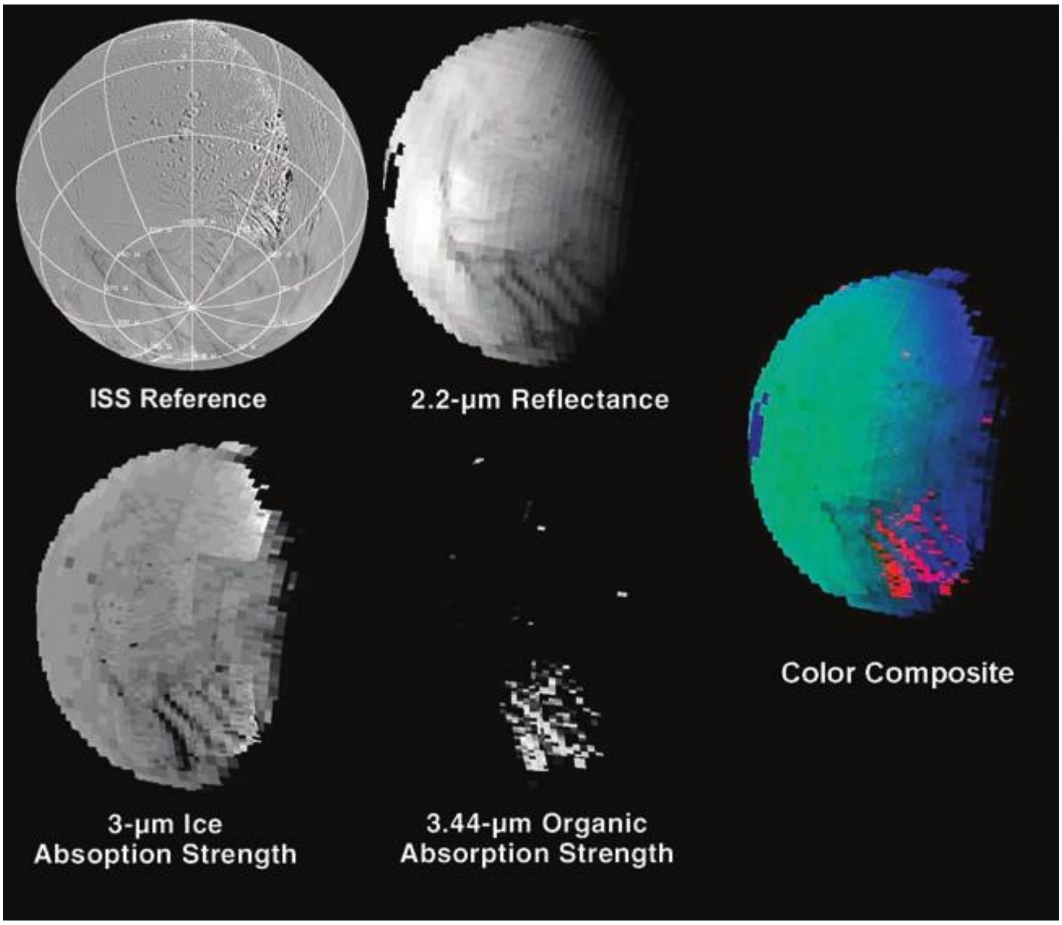

Figure 19. *Cassini VIMS surface composition from Brown et al., (2006).*

Sodium salts (NaCl and $NaHCO_3/Na_2CO_3$) have been reported in the ice grains in Enceladus' plume at the 0.1% - 1% level (Postberg et al. 2009a, 2011a, section 3.1, 3.2). It is possible that these salts could be detected by optical remote sensing. Carbonate salts have strong absorptions in the 2+ micron region due to C-O stretch-bend combinations. Sodium chloride, NaCl, is a naturally occurring mineral, halite. Halite is transparent in the VIMS spectral range unless the halite contains water. Adsorbed water absorption is shifted to shorter wavelengths than ice absorptions, but a high signal-to-noise ratio is needed to detect adsorbed water in small abundances. Halite shows a narrow 0.27-micron absorption (Clark et al., 2007), but this spectral region is not covered by any instrument on Cassini. Halite has not been measured in the deeper UV covered by the UVIS instrument. At present, the published VIMS spectra of the plumes have insufficient signal-to-noise ratios to constrain salt abundance. By averaging all VIMS spectra of the surface or the plume obtained over the entire mission might produce a high enough signal-to-noise ratio to constrain the salt abundance in the future.

6.2 Ultraviolet and visible light observations.

At far ultraviolet (FUV) and middle-ultraviolet (MUV) wavelengths, Enceladus' reflectance drops precipitously. Figure 20a shows an Enceladus spectrum acquired by UVIS (*Hendrix et al.*, 2010). Water ice has an absorption edge between 165 and 180 nm which is diagnostic of grain size. A combination of grain sizes can be found to fit the absorption edge of water ice to the UVIS spectrum, consistent with the water ice composition established by longer wavelength spectra. Anderson and van Dishoeck (2008) show that the ice absorption edge, in the UVIS spectral region, shifts to shorter wavelengths in amorphous ice relative to crystalline ice. While we do not have amorphous ice optical constants in the UVIS range at the temperatures of Enceladus, the crystalline optical constants provide a good match if the grain size is on the order of 10μm (Hendrix et al. 2010), consistent with the UV indicating the dominance of crystalline ice. For further discussion on crystalline and amorphous surface ice see section 7.2. There is an additional absorber(s) longward of 175 nm that reduces the reflectivity in the UVIS spectral range (Figure 20a).

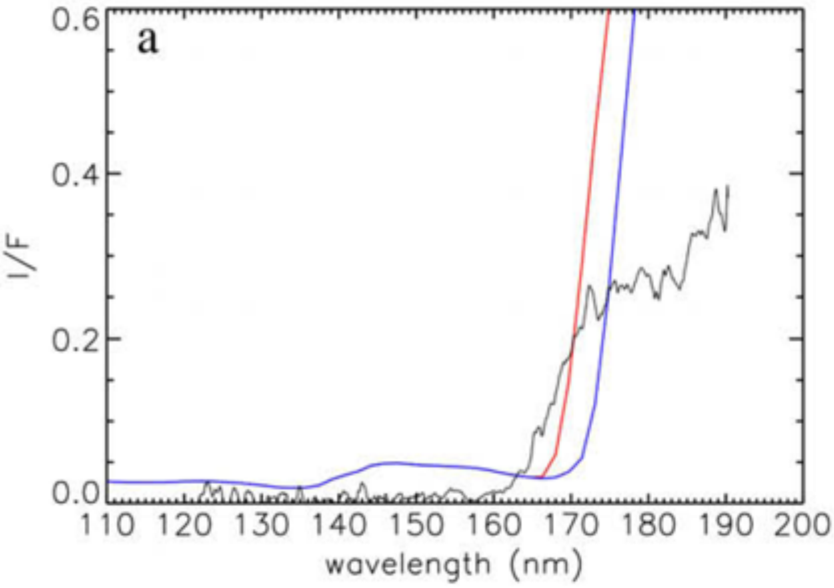

Figure 20a *(from Hendrix et al. 2010). This UVIS spectrum (grey) was acquired on 27 May 2007 at a range of 620,000 km at a solar phase angle of 2°. In red and blue two model spectra of crystalline water ice with different grain sizes are shown (blue: areal mixture of 70% 45 μm and 30% 400μm grains, red: areal mixture of two intimate ice grain mixtures of the two sizes). The mixture of grain sizes in the ice determines the precise location of the absorption edge between 165 and 180 nm. An additional absorber longward of ≈ 175 nm is required to fit the Enceladus spectrum.*

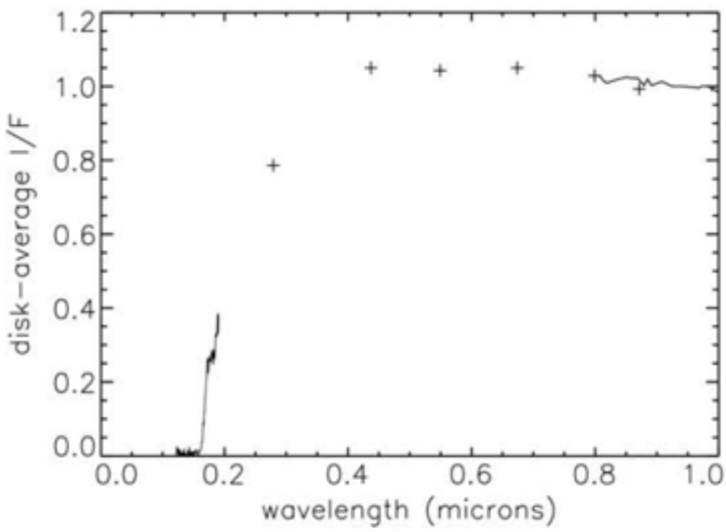

Figure 20b *UVIS FUV data are combined with a single MUV data point from HST at 275 nm (Verbiscer et al., 2005), the visible spectrum (plus signs) from Verbiscer et al (2005) and data from 800 to 1000 nm from Verbiscer et al (2006). The visible data were acquired at larger phase angles and thus do not reach the absolute albedo maximum of* 1.375 ± 0.008 (Verbiscer et al. 2007).

Figure 20b shows the spectrum of Enceladus when UVIS data are combined with the data at visible and near-infrared wavelengths from *Verbiscer et al*. (2005) and *Verbiscer et al.* (2006), as illustrated in *Hendrix et al.* (2010). With an I/F of > 1 Enceladus is very reflective at visible wavelengths >400 nm. At wavelengths shorter than 400 nm the disk-averaged I/F drops to 80% at 275 nm (*Verbiscer et al.*, 2005), then to < 40% at 190 nm. The UVIS FUV spectrum exhibits a "ledge" from 175 to 185 nm with ~30% reflectivity, with an upturn between 185 and 190 nm. The final drop-off short of 175 nm is due to the presence of water ice.

The spectrum of Enceladus at FUV and MUV wavelengths is not consistent with pure water ice. Some additional contaminant(s) must be present to darken the surface at wavelengths from 175 nm to 400 nm. The effort to identify this component(s) from the spectrum alone is hampered by a severe lack of laboratory data and optical constants in this wavelength range. There is, however, a fairly good idea of the constituents in the plume from INMS, UVIS, and CDA data. While gases escape (*Hansen et al.*, 2006), the larger plume particles preferentially fall back to the surface of Enceladus (Kempf et al. 2010, *Postberg et al.*, 2011a). Smaller plume particles tend to go into orbit forming the E ring, but they can be re-accreted on Enceladus' surface (for details see section by Kempf et al, this volume). A logical approach is to model non-water species in the plume as the contaminants darkening Enceladus' surface.

INMS has identified 0.4 – 1.3% NH_3 in the plume gas (*Waite et al.*, 2017) and, although the CDA has not reported a detection of ammonia in the ice grains, it is possible that nitrogen-bearing compounds are also emitted in the solid phase as minor species. The addition of ~1% NH_3 to water ice with larger grain size in the model surface spectra computed by *Hendrix et al.* (2010) reproduces the ledge seen in the UVIS spectrum from 175 to 185 nm and the upturn at ~185 nm (Figure 21). This finding was confirmed by UV observations with the Hubble Space Telescope (Zastrow et al., 2012). It is also in agreement with the upper limit of 2% NH_3 inferred from VIMS observations (Brown et al. 2006, see also section 6.1). Although NH_3 is not expected to be stable to photolysis and radiolysis on Enceladus' surface, ammonia hydrate may be, and is also consistent with ground-based near-infrared spectra (*Verbiscer et al.*, 2006). Moreover, NH_3 may not need to be stable over long timescales since it is probably constantly replenished. At wavelengths longer than 190 nm NH_3 is no longer an absorber towards the visible portion of the spectrum and an additional component must be present to explain the drop-off in reflectivity between 190 and 400 nm.

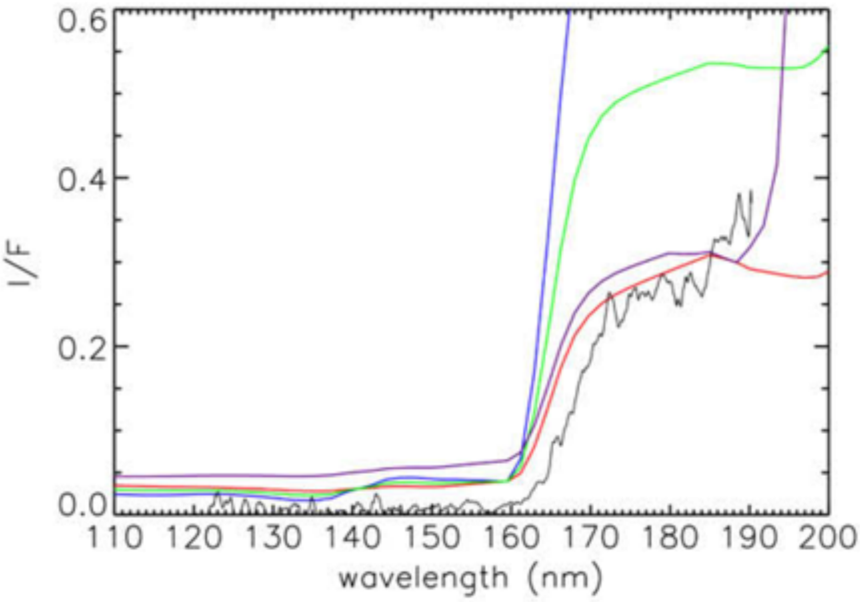

Figure 21. *(from Hendrix et al. 2010). Intimate mixtures of 99 % H_2O (grain size 1µm) and 1 % NH_3 (varying grain sizes: blue 1 µm, green 15 µm, red & purple 30 µm). Models used NH_3 data from Dawes et al. (2007) except purple line, which used NH_3 data from Martonchik et al. (1984).*

The aliphatic hydrocarbons detected by Brown *et al.* (see section 6.1) generally do not have UV absorbers that can explain Enceladus' UV spectrum. However, it has been shown that mixtures of H_2O + CH_4 + NH_3 ices which have been irradiated in the lab produce tholins (*Thompson et al.*, 1987). Moreover, more complex organics have been detected in the plume by CDA (*Postberg et al.*, 2008, 2018) and INMS (*Waite et al.*, 2009) and these may be processed on Enceladus' surface to form such tholins. Unfortunately, very limited spectral data have been published, however it does appear that some type of tholin material could be responsible for the darkening of Enceladus' surface at MUV wavelengths (*Hendrix et al.*, 2010).

A plausible alternative to an organic UV absorber would be nanophase iron in space weathered meteoritic dust. Clark *et al.* (2012) showed common spectral characteristics of the visible to UV absorber at some locations on Iapetus with other icy satellite surfaces in the Saturn system including Enceladus, and in the Cassini Division in Saturn's rings. On Iapetus, the deposits of dark material are relatively pure, and the VIMS data definitively reject tholins, leaving the nanophase metallic iron and iron oxides as the best explanation. However, at present on Enceladus, the available spectral data are insufficient to definitively distinguish between the tholin versus nano-iron plus nano-iron oxide explanation because the UV absorber signatures are relatively weak (see chapter by Hendrix et al., this volume).

7 PLUME / SURFACE INTERACTION

7.1. Constraints from grain size

Water ice is the main component observed in the plume ejected from Enceladus' Tiger Stripes. Most of the icy dust particles and gas erupted from this region redeposit on the surface at a rate that decreases with increasing distance from the surface fractures. The deposition rate had been simulated by Kempf et al (2010) and Southworth et al. (2018) to be 0.5 mm/yr close to the vents, and 10 μm/year at certain regions north of the equator assuming compact ice deposition (density ≈ 0.9 g/cm^3). The plumes' deposits are broad below 45°S, then, due to interactions with Saturn's gravity, they split into two patterns centered at ~45°W and ~225°W, respectively (Figure 22).

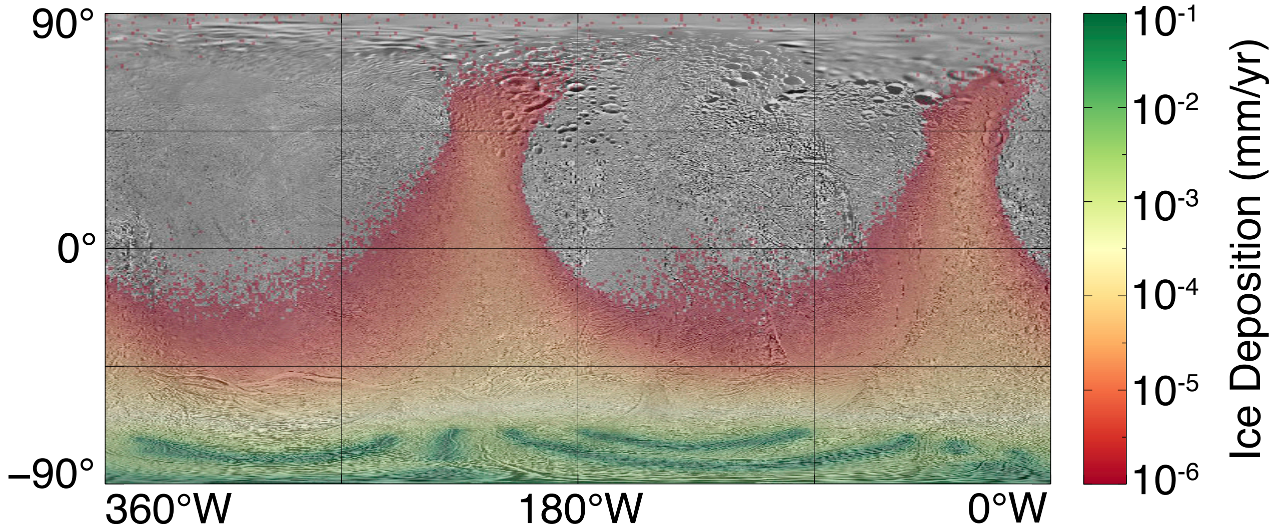

Figure 22: *Plume deposition on Enceladus surface as modeled by Southworth et al. (2018). The model assumes a homogenous distribution of sources all along the Tiger Stripe fractures.*

Scipioni et al. (2017) investigated whether the plume material that accumulates on the surface leaves a spectral signature that can be observed by analyzing data returned by VIMS between 0.88-5.12 μm (Figure 23). VIMS-IR spectra are sampled in 256 spectral channels, with an average spectral sampling of 16.6 nm (Brown et al., 2004). In general, the depth of absorption features is influenced by the variation of water ice abundance and grain size. Larger grains generally cause a deeper absorption, whereas if water ice is mixed with a contaminant

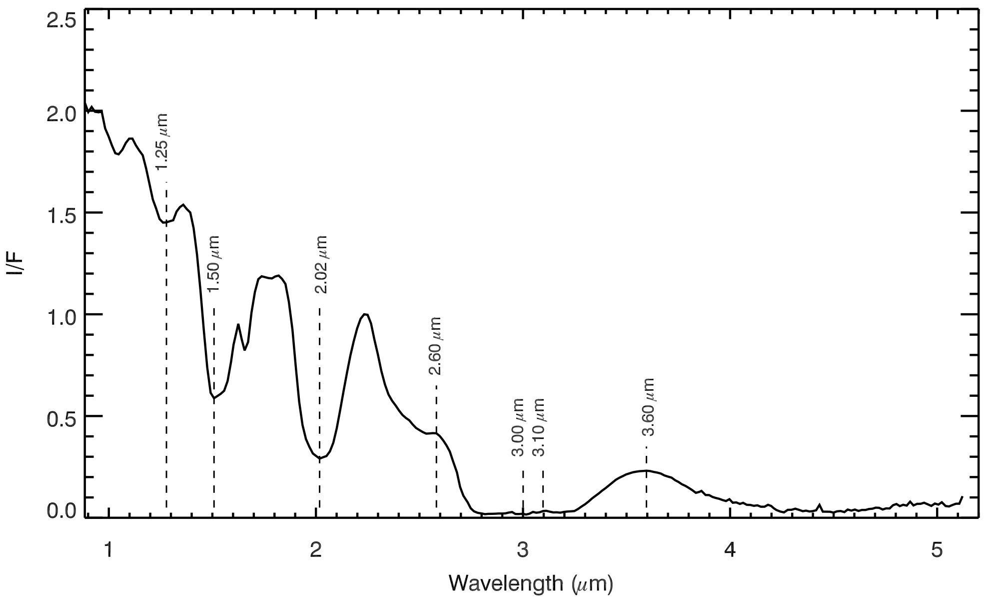

Figure 23. *VIMS Enceladus spectrum showing water ice absorption and reflection features in the near infrared. The main water ice overtones and combinations in the near infrared range are located at 1.04, 1.25, 1.5, 2.0, and 3.0 μm, while a reflectance peak arises at 3.6 μm.*

material, then band depths become shallower (Hapke et al., 1978; Clark, 1981a, 1981b). However, micron and sub-micron ice grains show enhanced band depths as the abundance of such grains increases (Figure 18) (Clark et al. 2012). Therefore, plume ice grain deposition, the sizes of which predominately lie in such a small size regime (Schmidt et al. 2008, Kempf et al. 2010, Postberg et al. 2011a), might increase band depth because of reduced scattering in closely packed small particles when the particles are much smaller than the wavelength (Clark *et a*l., 2012). Although the grain sizes of up to ~0.2 mm inferred by Jaumann et al. (2008) are probably drastically overestimated due to the aforementioned effect, the general finding of Jaumann et al. that larger grains are observed closer to the plume sources is in agreement with the observed size stratification of the plume (e.g., Hedman et al. 2009, see section 3.2 and chapter by Kempf et al., this volume).

To have a comprehensive view of the distribution of the abundance of the water ice and/or of the variation of the grain size across the surface, Scipioni et al. (2017) created spatially-resolved, cylindrically-projected maps of the selected water ice band depths and of the reflectance peak. From the comparison between model-predicted ice deposits and water ice distribution maps, the observation of deeper absorptions is expected where the plume deposition rate increases.

Water ice spectral signatures vary little across the surface of Enceladus (Figure 24), and water ice band depths only have subtle variations across Enceladus on average. The most pronounced difference in band depths values involves the South Polar Terrain (SPT). Indeed, the Tiger Stripes, and the terrains surrounding them, up to about -60° latitude, show by far the deepest water ice absorption bands, and the smallest value of the 3.6-μm reflectance peak. Elsewhere on the surface, the band depths and the reflection peak show a longitudinal variation. The terrains with the lowest band depth values are located between 0°W and 45°W, between 315°W and 360°W, and around 180°W, and they have almost constant band depths across the latitudinal direction. A regional bright spot shows up in the leading side, centered at about 90°W and 30°N. The near infrared reflectance (Figure 24d) of the bright spot is relatively high, while this spectral index decreases to background levels moving towards 0°W and 180°W.

To visualize the re-deposition processes taking place on the surface of Enceladus, the extracted level curves from the modeled deposition rate (Figure 22) are plotted on top of VIMS-derived maps in Figure 24. The water ice distribution maps show overall a good agreement with the predicted ejecta deposits in the SPT and in the eastern portion of the trailing hemisphere. The ice deposits along ~225° W predicted by the model (Figure 22) are in fact reproduced by color changes observed in the VIMS maps. From 205°W to 360°W, there is a qualitative match between the model and the data but the "wedged" shape of the deposition map is not well reproduced. On parts of the leading side (0°W - 135°W), the map and the plume deposit prediction's diverge. Although both the ejecta deposition rate and the water ice band depths show a longitudinal trend on the leading hemisphere, their positions in latitude do not exactly overlap. This divergence is at least partially caused by a regional bright spot centered at 30°N, 90°W. At this location, the deposition model predicts a rate below 10μm/year (Kempf et al., 2010).

The location of this bright spot on the leading hemisphere matches that of a microwave scattering anomaly (Ries & Jansen, 2015) found by Cassini's RADAR instrument. The feature correlates with a tectonized terrain with very few craters, indicative of a recent (< 100 Myr) resurfacing event, maybe caused by an ice diapir (Ries & Jansen, 2015). It is possible that this caused accumulation of fresh water ice, or annealing to bigger grain sizes, that would explain the deeper band depth in the near infrared observations and would mask the faint signature of the plumes' deposits in this region.

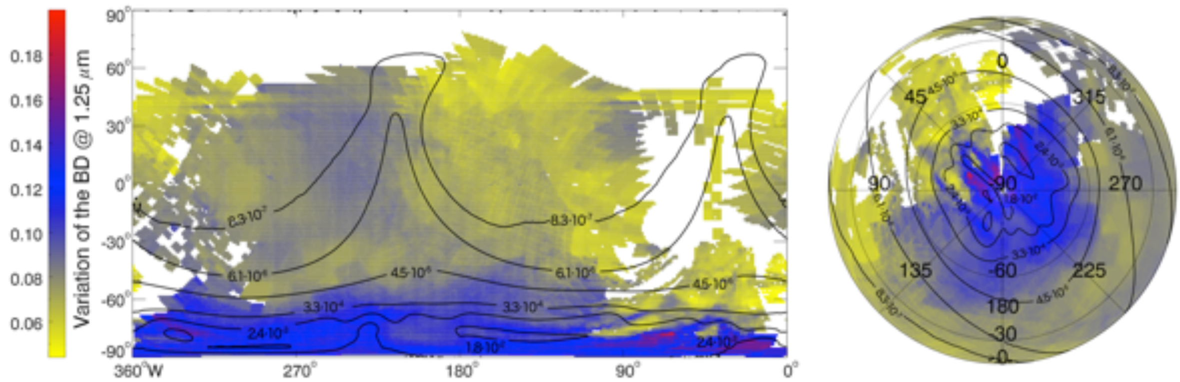

(a)

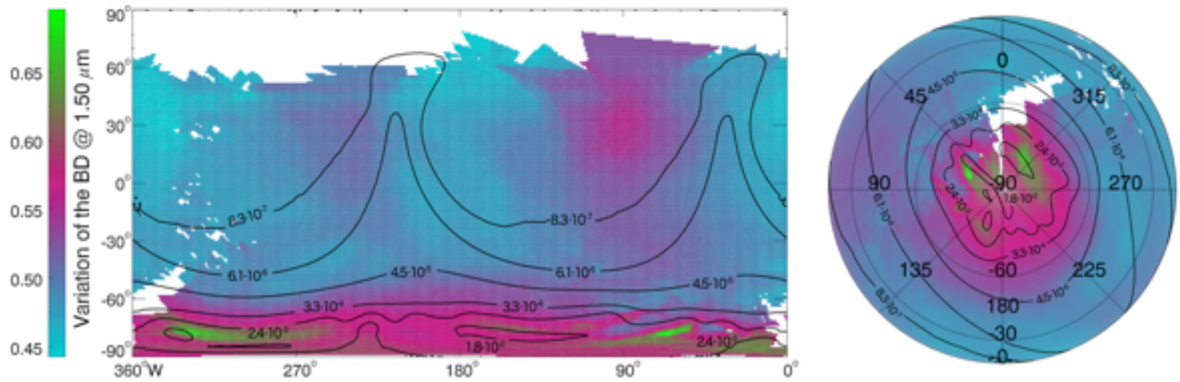

(b)

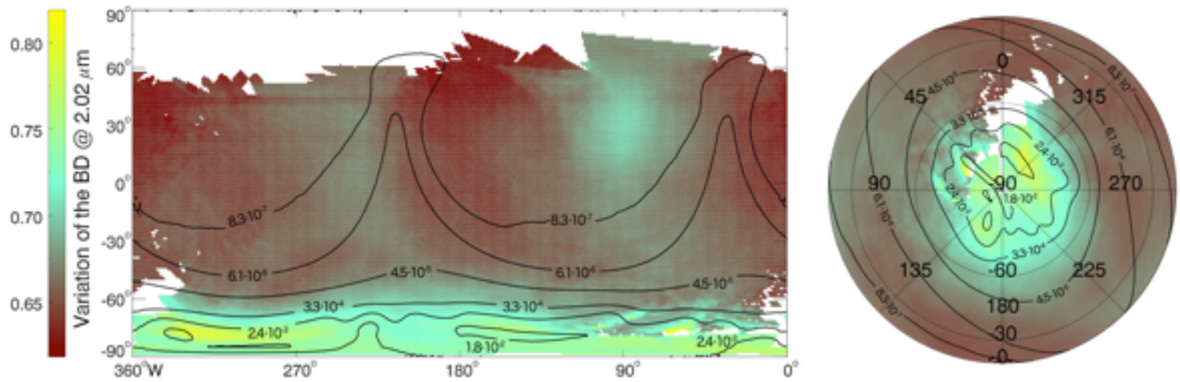

(c)

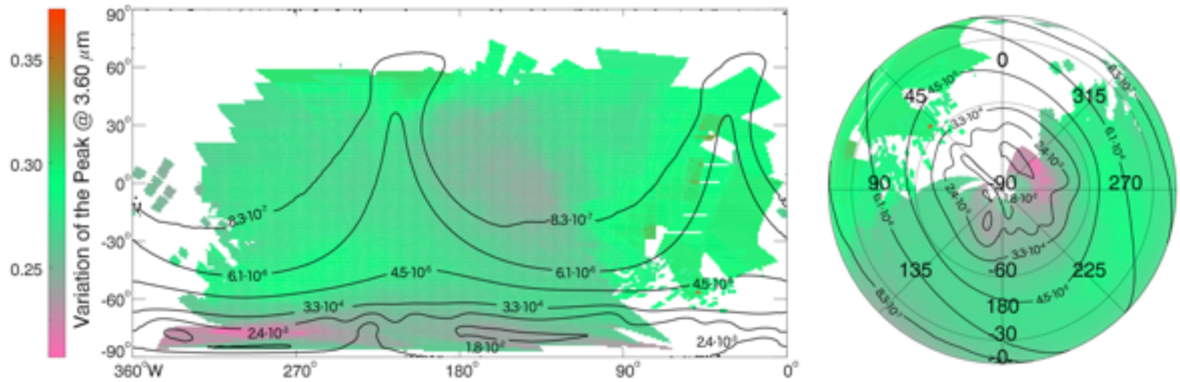

(d)

Figure 24 *Panels from top to bottom map the 1.25, 1.5, 2-µm band depth (a – c), and the strength of the 3.6-µm reflectance peak (d), respectively. Contour lines correspond to yearly plume deposition rate in millimeters (Southworth et al., 2018) under the, unrealistic, assumption of compact ice deposition with a density of 0.9 g/cm^3.*

The near infrared data can be compared to four global, high spatial resolution color ratio maps form Cassini's Imaging Science Subsystem (ISS) produced by Schenk et al. (2011) by cylindrically projecting and mosaicking ISS data in the IR3 (0.930 µm), GRN (0.586 µm) and UV3 (0.338 µm) filters.

Except for the IR3/GRN ratio map, the maps displayed in Figure 25 agree with the plume deposition model very well. The position as well as the shape of the features in the ratio maps matches the deposition model. In contrast to the near infrared maps, the match is also good on the leading hemisphere and in general the match is more accurate for these visible maps (Figure 25) compared to the near infrared maps of Figure 24. The reason for this mismatch might be that in visible light, water ice is more transparent than in the near infrared, leading to a more apparent optical effect produced by a trace abundance of a non-ice component (discussed above), or due to a grain size difference between the non-ice components and the ice. The bright region in the leading hemisphere, observed in the near infrared water ice band depth maps, is only apparent in the GRN/UV3 and not as obvious in the IR3/UV3 map.

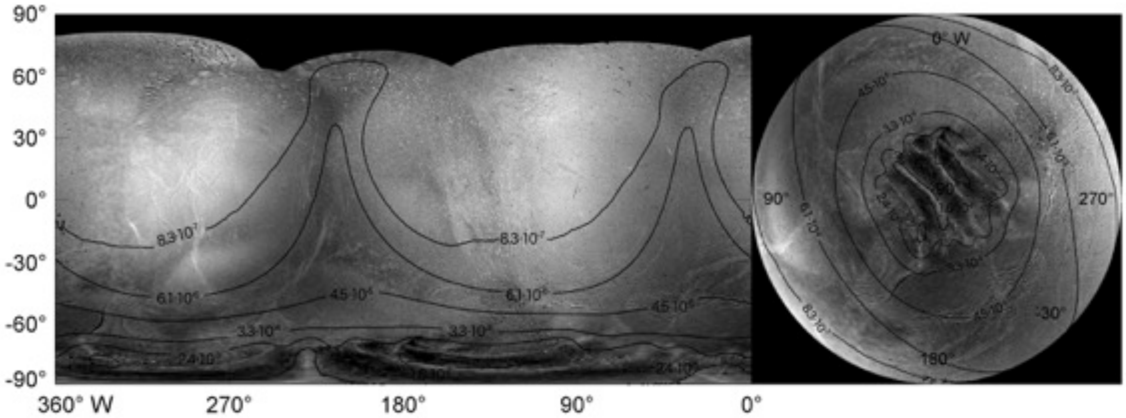

a)

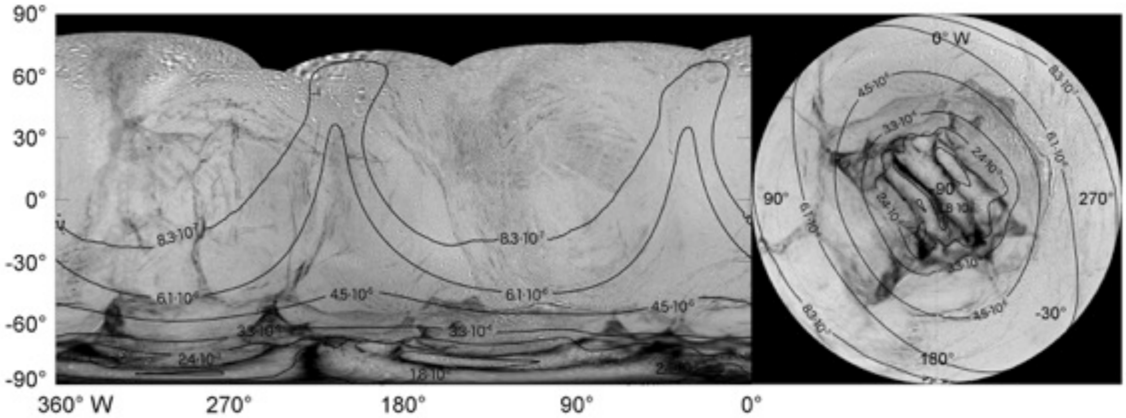

(b)

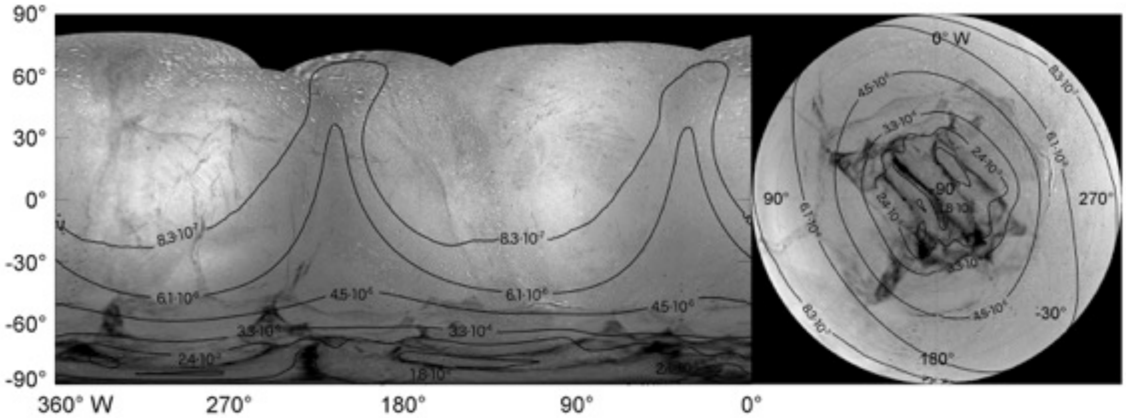

(c)

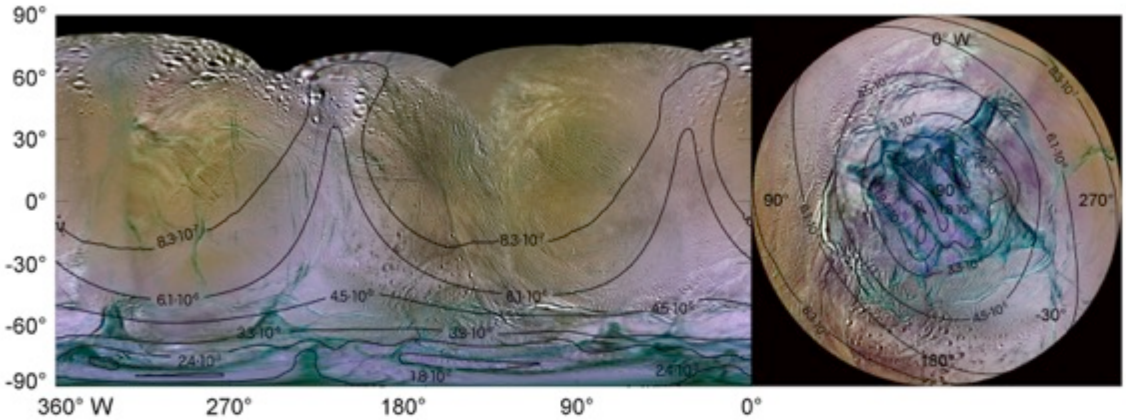

(d)

***Figure 25** The first three panels show three Cassini ISS ratio maps: GRN/UV3 (a), IR3/GRN (b), and IR3/UV3 (c) (Schenk et al. 2011). The last panel, 25d, represents the RGB combination of the three filters. In the a, b, and c color ratio maps, bright areas are* *associated with a positive slope relative to the ratioed bands. The bright regions in the a, c, and d combination resemble well the plume fallout outlined by deposits model (Southworth et al., 2018). The IR3/GRN map (25b) is smoother and does not resemble ejecta deposits.*

7.2 Constraints from ice crystallinity

Mapping the crystallinity of surface ices on Enceladus provides an alternative method to find indicators of plume deposition on its surface. At the average surface temperature on the icy Saturnian satellites, ~80 K, amorphous ice is stable against thermal recrystallization for long timescales (Mastrapa et al. 2013). Temperature enhancements beyond 135 K are known to cause a phase change in H_2O ice from amorphous to crystalline; H_2O ice can then re-amorphize over time when subjected to ion bombardment as shown by Mastrapa & Brown (2006) or by micrometeorite bombardment. Changes in H_2O ice phase can thus be used to track variations in temperature and physical conditions on the surface, ideal to reveal past and/or present processes on the surface. In the case of Enceladus, H_2O plume vapor deposited on a cold surface (≤130 K) might produce amorphous ice (Baragiola et al., 2008) while icy plume deposits are expected to be crystalline (Dhingra et al. (2017), also see section 3.4). Consequently, amorphous H_2O ice at the SPT might mark the presence of a vapor deposition mechanism whereas crystalline ice would be indicative of deposition of plume ice grains as the dominant process. Moreover, amorphous ice further away from the SPT could indicate an "old" surface where secondary effects, like space weathering, are more efficient than plume deposition.

Although early Cassini results by Brown et al. (2006) indicated amorphous ice, later work by Clark et al. (2012) indicated that the effects of diffraction from sub-micron ice grains might explain the observed VIMS spectra of Enceladus rather than amorphous ice. Brown et al. (2006) based amorphous ice detection on a decrease in strength of absorption at 1.65 μm, and a decrease in intensity of the 3.1-μm Fresnel peak. Clark et al., (2012) showed both of these effects are also caused by diffraction from sub-micron ice particles in the surface.

The analysis of VIMS data in principle allows spatially resolved measurements but no results on the detection and distribution of amorphous ice have been published yet. However, various analyses to constrain the effects of plume deposition with a "crystallinity map" are currently ongoing (e.g., with the method established by Dalle Ore et al. 2015 but modified for the effects sub-micron ice grains).

8. CONCLUSIONS AND OPEN QUESTIONS

8.1. Plume composition

The Enceladean plume is composed of three different phases: Gas, solids (dust), and ions. Neutral gas is the most abundant component and is emitted with an average rate of 170 – 250 kg/s (Hansen et al. 2017). The estimates for the emitted solid material vary much more. This estimate only partially reflects the orbital variation in emitted dust that appears to be larger than for gas (Hedman et al. 2013, Nimmo et al. 2014, Ingersoll & Ewald 2017, Hansen et al. 2017) but also reflects the larger uncertainty of the dust flux estimates. Estimates range from about 3 - 5kg/s (Schmidt et al. 2008, Kempf et al. 2010) to 50 kg/s (Ingersoll & Ewald, 2011) or 15 – 65 kg/s (Dong et al. 2015). The arguably most robust value is given by Kempf et al. (this volume) with about 20 kg/s and yields a dust to gas ratio about 10% (for a detailed discussion see chapter by Kempf et al., this volume). The ejection speed of the gas is much larger than that of the dust grains (Schmidt et al. 2008, Hedman et al. 2009), therefore the gas almost completely escapes into space. The ionic component is picked up by Saturn's magnetosphere and also escapes Enceladus' gravitational influence. The abundant nanometer-sized grains observed by CAPS (Hill et al 2012, Dong et al. 2015) probably also almost completely escape. However, only a fraction (5 – 10%) of the solid material larger than ≈ 0.1 μm in the plume escapes into the E ring, whereas the greater part is falling back to the surface (Porco et al. 2006, Spahn et al. 2006, Schmidt et al. 2008, Kempf et al. 2010, Ingersoll & Ewald 2011), a fact that strongly couples plume composition and surface composition (see section 8.3). The probability of escape is coupled to the grain size: larger grains are ejected at lower speeds, leading to the observed tendency of large particles preferentially populating the lower regions of the plume and smaller grains preferentially escaping into the E ring (Kempf et al. 2008, Hedman et al. 2009). This size dependence also causes a compositional plume stratification (Postberg et al. 2011a, Khawaja et al. 2017) (see 8.2).

All three phases (gas, dust, and ionic) are primarily composed of water. For the neutral gas the water abundance is larger than 96%, for dust grains with $r > 0.2$ μm it is in the order of 99%, whereas the water proportion in the ionic phase, though dominant, is less well constrained. The majority of ice grains in the plume are in a crystalline (and not amorphous) state (Dhingra et al., 2017) indicative of formation temperatures above 130K. Although the general interpretation that these grains are made of water ice is justified (e.g. Hill et al., 2012), the composition of the predominately negatively charged nano-grains in the plume is actually not known (see section 8.4. 'Open Questions').

The main non-icy compounds in the solid phase ($r > 0.2$ μm) are sodium salts and organic material. Salts and organics are heterogeneously distributed over three compositional diverse main ice grain populations and can both reach percent level abundance in individual grains (Postberg et al. 2009a, 2011a, 2018). SiO_2 is another important constituent (> 100 ppm) but was indirectly inferred by measurements in the outer Saturnian system (Hsu et al., 2011, 2015). The most abundant volatiles are ammonia, molecular hydrogen, carbon dioxide, and organics. Each of these compounds is present in mixing ratios of fractions of a percent with upper limits of H_2 and NH_3 slightly above 1% (Waite et al. 2017). The D/H ratio is 2.9 (+1.5/–0.7) x 10^{-4} and is approximately in the mid-range of observed cometary D/H values and much higher than in Saturn's atmosphere (Waite et al., 2009). Methane (≈ 0.2%) is the most abundant organic compound in the gas phase with less abundant C_2 and maybe C_3 species (Magee & Waite, 2017). In comparison, the ice grains carry more refractory organic material with atomic masses ranging from about 28 u up to at least 200 u (Postberg et al. 2008, 2018). O- and N-bearing organic species might be present in both, neutral gas and ice grains (Magee & Waite 2017, Postberg et al. 2018). The tentative detection of ammonia in the surface ice of Enceladus (Emery et al. 2005, Verbiscer et al. 2006, Hendrix et al. 2010, section 4.2) supports the idea of nitrogen-bearing ice grains being emitted by the plume.

In general, the sensitivity of Cassini instruments to minor species in ionized form is lower than for neutral molecules or macroscopic ice grains. Ions directly measured in the plume are composed almost exclusively of water and water products. Detected cations have the form H_nO^+ ($n = 0 - 3$) and respective dimers. Detected anions are dissociated water molecules (OH, H^-, O^-) or cluster of the form $(H_2O)_nOH^-$ ($n = 1 - 3$) (Tokar et al. 2009, Coates et al. 2010a, 2010b). The only indication for ions other than from water are high-mass anions (> 200 u) possibly in agreement with complex organics (Coates et al., 2010a, 2010b). In contrast, there is ample evidence for non-water ions from integrated measurements in Saturn's magnetosphere that likely were emitted by Enceladus' plume. The most apparent are N-bearing cations, in particular NH^+ detected by CAPS, present on a level of a few percent (Smith et al. 2008), a proportion that seems to be difficult to reconcile with the lower abundance of N-bearing species in the plume (see section 8.4 for further discussion). The detection of N^+ by the MIMI-CHEMS sensor supports this result. The instrument also finds C^+ in similar abundance (≈ 1%) indicative of dissociation of organic plume constituents. Another ion species of possible plume origin detected in trace abundance, are cations with a mass of 28 u that could be $C_2H_5^+$, $HCNH^+$, N_2^+, Si^+, and CO^+ (Christon et al. 2014, 2015). See section 8.4 for further discussion.

Possible origins of the different constituents in Enceladus' interior are discussed in section 5 and in the chapter by Glein et al. this volume.

8.2. Variability of the plume composition in space and time

There is clear indication of spatial variation in the plume's composition. Most apparent is the compositional stratification of the ice grains with $r > 0.2$ µm measured by the CDA. Ice grains containing significant amounts of sodium and potassium salts are significantly more abundant at low altitudes. This stratification is indicative of lower ejection speeds caused either by slower ejection speed of the carrier gas or by the larger size of these grains (Postberg et al., 2011a). In turn the almost pure water ice grains are more abundant at high altitudes and in the fraction that escapes into the E ring. Organic bearing grains appear to be most abundant in confined high velocity jets at all altitudes (Postberg et al. 2011a, Khawaja et al. 2017). The stratification outlined above is based on proportions, obviously the absolute abundance of ice grains of any composition increases with lower altitudes. The plume material above Baghdad and Damascus sulci has a dust-to-gas mass ratio that is roughly an order of magnitude higher than the material above Alexandria and Cairo sulci (Hedman et al. 2018). This difference suggests, but does not prove, that the there is a lateral variation in the ice grain composition (Postberg et al. 2011a, Dhingra et al., 2017). Organic bearing grains are possibly more abundant in emissions from Damascus sulcus than from the other sulci (Postberg et al. 2011a, Brown et al. 2006).

The spatial density variation of the neutral gas inside the plume is substantial (Hansen et al. 2008, Teolis et al., 2017). However, it is not known if a compositional variation is linked to this spatial variation. The only clue from Cassini is INMS measurements which indicate that heavier molecular species (e.g. CO_2, 44 u) have a narrower lateral spread than lighter species (e.g., H_2, 2 u) in a supersonic jet cone (Perry et al. 2015).

Spatial variations in the composition of the ionized phase have not been reported. However, charged molecules and charged nano grains both will have very different trajectories compared to the ballistic trajectories of the neutral gas and larger grains. The plasma environment is dominated by the dynamics of the interactions between the plume neutral gas and the co-rotational plasma in Saturn's magnetosphere (see chapter by Smith et al., this volume) Because the charge-to-mass ratios of nanograins are sufficiently large, their dynamics are strongly influenced by the Lorentz forces and thus sensitive to the local electromagnetic environment resulting from the plume-magnetosphere interactions. Grains with radii of a few nm with both polarities are found in the plume (Jones et al., 2009), and these grains are likely responsible for several features observed in the Cassini magnetic field and thermal plasma data (Simon et al., 2011, Hill et al., 2012, Meier et al., 2014, Meier et al., 2015, Dong et al., 2015). Fluxes of both plasma ions and charged nanograins emitted by

Enceladus will strongly vary with magnetic field and co-rotational plasma conditions and could potentially be linked to a compositional variation.

The plume is known to be time variable. The most apparent activity cycle is coupled to the moon's orbital period (Hedman et al. 2013, Nimmo et al. 2014, Ingersoll & Ewald 2017). The plume brightness from emitted ice grains varies by about a factor of 4 between apocenter (maximum) and pericenter (minimum). This variation can be explained either by a change in total mass flux or by a drastic change in the grain size distribution or by a superposition of both effects (Hedman et al., 2013). A variation by a factor of four has also been observed for the nanograin flux (Smith et al. 2010, Blanc et al, 2015) (for detail see chapter by Smith et al., this volume). There is also indication for brightness variations on the order of years (Hedman et al. 2013, Ingersoll & Ewald 2017). By contrast, the variations in the integrated emitted gas flux over time seem to be milder (Hansen et al. 2017, Teolis et al. 2017). Currently no compositional variation can be linked to either these variations (see section 8.4.).

8.3. Surface composition

Enceladus exhibits the cleanest water ice surface with the highest visible albedo known in the solar system (Verbiscer at al. 2007). The only non-icy component that has been measured with certainty is CO_2 that is trapped in surface water ice. CO_2 appears to be most abundant in the south polar terrain (Brown et al. 2006). An absorption in the far UV consistent with NH_3 mixed in water ice has been identified in disk-averaged UVIS images (Hendrix et al. 2010) but is only in agreement with its absence in near infrared spectra at concentrations of less than 2% (Emery et al. 2005, Verbiscer et al. 2006, Brown et al., 2006). Infrared bands consistent with aliphatic hydrocarbons have been identified along the tiger stripe fissures (Brown et al. 2006). Suitable candidates for an absorption in the mid UV, also observed on other icy moons of Saturn (see chapter by Hendrix et al., this volume), might be some sort of tholins or traces of a mixture of nano-phase iron and iron oxide.

Deposition of plume material, especially micron-sized ice grains, happens on most of Enceladus surface. If E ring deposition is also taken into account, the entire surface is exposed to plume material (see chapter by Kempf et al., this volume) though deposition rates vary with surface location. The south polar terrain is subject to intense resurfacing by icy plume deposits and the composition there should be largely governed by the composition of the emitted ice grains. From deposition maps (Schenk et al. 2011, Scipioni et al. 2017) and plume dynamics (see section by Goldstein et al. this volume), the largest grains fall back onto the surface closest to their Tiger Stripe sources. CDA data indicate that these large grains are particularly rich in non-icy components, which make it likely that sodium salts, in particular chloride and carbonate/bicarbonate, and organic compounds are present in substantial quantities of up to ≈ 1% close to the Tiger Stripe fissures.

At present, the published VIMS spectra of the plumes have insufficient signal-to-noise ratios to constrain the salt abundance. Organic material is likely present near the tiger stripes (Brown et al., 2006) and "tholins" are tentatively indicated (Hendrix et al. 2010). If the latter are present, they could be the result of space weathering of organic precursors in the plume and can form on geological time scales. This process might be more efficient at regions further away from the south polar terrain which are not subject to the highest deposition rates of fresh plume material. Although the deposition of crystalline ice grains from the plume might argue for mostly crystalline surface ice, at least near the south polar terrain, the question of whether amorphous ice is present on Enceladus' surface has not been fully resolved.

8.4. Major open questions

The only reduced carbon plume compound that can be identified with certainty is methane. Although there are definite measurements of further (unspecified) organic species with higher masses in the ice grains (Postberg et al. 2008, 2018) and the neutral plume gas (Waite et al. 2009, Magee & Waite 2017), the actual organic compounds are poorly constrained qualitatively and quantitatively. In the plume gas, this uncertainty concerns unspecified species with up to three C-atoms whereas in the ice grains the organic molecules, at least occasionally, are much more complex (Postberg et al. 2018). It is also likely that the limited mass resolution of the CDA not only limits the detection and specification of organic compounds but also the detection of inorganic compounds, like minerals and salts other than the most abundant species reported by Postberg et al. (2009a). In particular, ammonia or other nitrogen-bearing species would be in agreement with observations of Enceladus' surface (Hendrix et al. 2010). One of the major compositional uncertainties is the unidentified species at 28 u. There is no such species detected by the INMS in the plume with an upper limit below 0.1% (Waite et al. 2017). However, UVIS reports traces of organic species, attributed mostly to C_2H_4 (28 u), in the plume (Shemansky et al., 2016) and an unspecified ionic species with 28 u is detected in Saturn's magnetosphere (Christon et al. 2013, 2014). Obviously, a better understanding of the organic as well as the inorganic plume inventory is a critical element for the investigation of Enceladus' subsurface ocean by future missions (see chapter by Lunine et al., this volume).

Cassini's instruments could not directly measure the composition of nanograins in the plume. Although it is a plausible assumption that they are mostly or exclusively composed of water ice, the actual composition is in principle unknown. Nanograins play an important role in the overall emission of solid plume material (Hill et al. 2012), and they are in contrast to the larger grains ($r > 0.1$ µm) observed by CDA that completely escape into the Saturnian system. At least some of the emitted nanograins are composed of SiO_2. Dynamical modeling indicates that these are different from the nano-grains directly observed in the plume (Hsu et al., 2011, 2015, Hill et al., 2012). SiO_2 grains might leave the vents primarily incorporated into macroscopic ice grains and are only released later by plasma sputter erosion of their carriers (Hsu et al. 2015) in the E ring, but it is actually unclear whether SiO_2 nano-grains also exist as individual particles in the plume.

The overabundance of N-bearing ions (in particular NH_x^+) from Enceladus in Saturn's magnetosphere (Smith et al. 2008) compared to the apparent plume composition is a long-standing unresolved question. Possible explanations could be: a) NH_x^+ has a long lifetime compared with water ions and is therefore overrepresented in the ionic phase; b) abundant N-bearing species are emitted in the form of organic molecules (in the gas and in ice grains) that, after their dissociation, feed NH_x^+ into the magnetosphere; c) Nanograins are effective carriers of N-bearing species that are later released as ions into Saturn's magnetosphere. The tentative detection of ammonia in the surface ices of Enceladus (Emery et al. 2005, Verbiscer et al. 2006, Hendrix et al. 2010) supports the idea of nitrogen-bearing ice grains emitted by the plume.

Except for the compositional stratification of the macroscopic ice grains in the plume (Postberg et al., 2011a), variations of the plume's composition in space and time are not yet well constrained by Cassini measurements. However, given the rich dynamical fine structure (Hansen et al. 2008, 2017, Porco et al. 2014, Teolis et al. 2017, Southworth et al. 2018) and the quite drastic diurnal orbital variation in the plume brightness (Hedman et al., 2013, Nimmo et al., 2014, Ingersoll & Ewald 2017) it is highly likely that, yet unknown, compositional variations coincide with the variations in activity.

Sodium salts and organic compounds are currently poorly constrained on the Enceladean surface although their presence in quantities up to the percent level on the south polar terrain is highly likely. The effects of submicron grains on VIMS spectra have been underestimated at first and a new VIMS calibration was required for observations that occurred later in the mission (Clark et al. 2016). Therefore, a more sophisticated analysis of the VIMS data might reveal more information on organics in the near future. Ultimately, co-adding all VIMS spectra of the surface obtained over the entire Cassini mission may produce a spectrum with a sufficiently high signal-to-noise ratio to constrain salt abundances in the near future.

There is a non-water mid UV absorber on Enceladus. It seems to have similar properties to impurities observed on other icy moons (see chapter by Hendrix et al. this volume) and the main rings (e.g., Clark et al. 2012, Filacchione et al. 2012). At present, the available spectral data are insufficient to definitively distinguish between the two best candidates: tholins or a mixture of nano-phase iron and iron oxide. The latter could potentially indicate impact gardening by space weathered meteoritic dust.

The detection of amorphous water ice on Enceladus could reveal more of its surface history by identifying regions where ice condensed from vapor at low temperatures or locations where previous surface modification by particle bombardment is/was more efficient than the deposition of crystalline plume ice grains. Amorphous water ice may still be detected on the surface of Enceladus in Cassini VIMS spectra if the latest VIMS calibration (Clark et al., 2016) is applied, but such analyses have not been done at the full spatial resolution of the VIMS dataset.

Acknowledgements:

F.P. acknowledges funding from the European Research Council (ERC) under the European Union's Horizon 2020 research and innovation programme (Consolidator Grant 724908-Habitat OASIS).

References

Altobelli N., Postberg F., Fiege K., Trieloff M. and 11 co-authors (2016) Flux and composition of interstellar dust at Saturn from Cassini's Cosmic Dust Analyser, *Science* 352, 312-318.

Anderson, S, and E. F. van Dishoeck, 2008, Photodesorption of water ice *Astron and Astrophys*. **91**, 907–916.

Arridge, C.S., N. André, H.J. McAndrews, E.J. Bunce, M.H. Burger, K.C. Hansen, H.-W. Hsu, R.E. Johnson, G.H. Jones, S. Kempf, K.K. Khurana, N. Krupp, W.S. Kurth, J.S. Leisner, C. Paranicas, E. Roussos, C.T. Russell, P. Schippers, E.C. Sittler, H.T. Smith, M.F. Thomsen and M.K. Dougherty (2011) Mapping Magnetospheric Equatorial Regions at Saturn from Cassini Prime Mission Observations, *Space Sci Rev*, *164*, 1–83.

Balsiger, H., Altwegg, K., Geiss, J. (1995) D/H and $^{18}O/^{16}O$ ratio in the hydronium ion and neutral water from in situ ion measurements in comet Halley, JGR 100, 5827-5834.

Baragiola, R.A., Famá, M., Loeffler, M.J., Raut, U., & Shi, J. 2008. Radiation effects in ice: New results. Nuclear Instruments and Methods in Physics Research B, 266, 3057-3062.

Blanc, M., D.J. Andrews, A.J. Coates, D.C. Hamilton, C. Jackman, X. Jia, A. Kotova, M. Morooka, H.T. Smith, J.H. Westlake (2015), Saturn plasma sources and associated transport processes, *Space Science Reviews, 192*, 237-283.

Bouquet A., Mousis O., Waite J.H., Picaud S. (2015) Possible evidence for a methane source in Enceladus' ocean, GRL 42, 1334 – 1339.

Brown, R. H. and 21 co-authors (2004). The Cassini Visual and Infrared Mapping Spectrometer (VIMS) investigations. Space Science Reviews 115, 111-168.

Brown R. H. and 24 co-authors (2006) Composition and physical properties of Enceladus' surface. Science 311, 1425 – 1428

Cadek, O., Tobie, G., van Hoolst, T., Masse, M., Choblet, G., Lefevre, A., Mitri, G., Baland, R.-M., Behounkova, M., Bourgeois, O.. Trinh, A. (2016) Enceladus's Internal Ocean and Ice Shell Constrained from Cassini Gravity, Shape, and Libration Data. GRL, Vol. 43, No. 11, 5653–5660

Choblet, G., Tobie, G, Sotin, C., Běhounková, M., Čadek, O., Postberg, F., Souček, O. (2017) Powering prolonged hydrothermal activity inside Enceladus. Nature Astronomy **1**, 841 - 847.

Christon, S.P., D.C. Hamilton, R.D. DiFabio, D.G. Mitchell, S.M. Krimigis and D. S. Jontof-Hutter (2013) Saturn suprathermal O_2^+ and mass-28^+ molecular ions: Long-term seasonal and solar variation, *J. Geophys. Res*., *118*, 3446–3462.

Christon, S.P., D.C. Hamilton, D.G. Mitchell, R.D. DiFabio, and S.M. Krimigis (2014) Suprathermal magnetospheric minor ions heavier than water at Saturn: Discovery of $^{28}M^+$ seasonal variations, *J. Geophys. Res*., *119*, 5662-5673, 2014.

Christon, S.P., D.C. Hamilton, J.M.C. Plane, D.G. Mitchell, R.D. DiFabio and S.M. Krimigis (2015), Discovery of suprathermal Fe^+ in Saturn's magnetosphere, *J. Geophys. Res., 120*, 2720-2738.

Clark, R. N., 1981a, The spectral reflectance of water-mineral mixtures at low temperatures: *Journal of Geophysical Research,* **86**, p. 3074-3086.

Clark, R. N., 1981b, Water frost and ice: The near-infrared spectral reflectance 0.65-2.5 μm: *Journal of Geophysical Research,* **86**, p. 3087-3096.

Clark, R., Roush, T., 1984. Reflectance spectroscopy - Quantitative analysis techniques for remote sensing applications. Journal of Geophysical Research 89, 6329-6340.

Clark, R., Carlson, R., Grundy, W., Noll, K., 2011. Chapter 1: Observed ices in the Solar System. In Murthy Gudipati (Ed.), Solar System Ices, 3-46.

Clark, R.N., Swayze, G.A., Wise, R., Livo, E., Hoefen, T., Kokaly, R., Sutley, S.J., 2007, USGS digital spectral library splib06a: *U.S. Geological Survey*, Data Series 231, http://speclab.cr.usgs.gov/spectral-lib.html

Clark, R. N., D. P. Cruikshank, R. Jaumann, R. H. Brown, K. Stephan, C. M. Dalle Ore, K. E. Livo, N. Pearson, J. M. Curchin, T. M. Hoefen, B. J. Buratti, G. Filacchione, K. H. Baines, and P. D. Nicholson, 2012, The Composition of Iapetus: Mapping Results from Cassini VIMS, *Icarus*, **218**, 831-860.

Clark, R. N., R. H. Brown, and D. M. Lytle, 2016, The VIMS Wavelength and Radiometric Calibration, NASA Planetary Data System, The Planetary Atmospheres Node, http://atmos.nmsu.edu/data_and_services/atmospheres_data/Cassini/vims.html, 23pp.

Coates, A.J., G.H. Jones, G.R. Lewis, A. Wellbrock, D.T.Young, F.J. Crary, R.E. Johnson, T.A. Cassidy, T.W. Hill (2010a) Negative Ions in the Enceladus Plume, *Icarus*, *206*, 618–622.

Coates, A.J., A. Wellbrock, G.R. Lewis, G.H.Jones, D.T. Young, F.J. Crary, J.H. Waite, R.E. Johnson, T.W. Hill, E.C. Sittler Jr. (2010b) Negative ions at Titan and Enceladus: recent results, *Faraday Disc*., *147*, 293-305.

Coates, A.J., A. Wellbrock, G.H. Jones, J.H. Waite, P. Schippers, M.F. Thomsen, C.S. Arridge, and R.L. Tokar (2013), Photoelectrons in the Enceladus plume, *J. Geophys. Res*., *118*, 5099–5108.

Cravens, T. E., N. Ozak, M. S. Richard, M. E. Campbell, I. P. Robertson, M. Perry, and A. M. Rymer (2011), Electron energetics in the Enceladus torus, J. Geophys. Res., 116, A09205, doi:10.1029/2011JA016498

Cruikshank D.P., Owen T.C., Dalle Ore C., Geballe T.R., Roush T.L., de Bergh C., Sandford S.A., Poulet F., Benedix G.K., Emery J.P. (2005) A spectroscopic study of the surfaces of Saturn's large satellites: H 2 O ice, tholins, and minor constituents. Icarus 175:268–283

Dawes, A., Mukerji, R.J., Davis, M.P., Holtom, P.D., Webb, S.M., Sivaraman, B.,Hoffmann, S.V., Shaw, D.A., Mason, N.J., 2007. Morphological study into the temperature dependence of solid ammonia under astrochemical conditions using vacuum ultraviolet and Fourier-transform infrared spectroscopy. J. Chem. Phys. 126, 244711-1–244711-12.

Dalle Ore, C.M., Cruikshank, D.P., Mastrapa, R.M.E., Lewis, E., & White, O.L. 2015. Impact craters: An ice study on Rhea. Icarus, 261, 80

Degruyter, W., Manga, M., 2011. Cryoclastic origin of particles on the surface of Enceladus. Geophysical Research Letters 38, L16201.

Dhingra, D. Hedman, M.M., Clark, R.N., Nicholson, P.D. (2017). Spatially Resolved Near Infrared Observations of Enceladus' Tiger Stripe Eruptions from Cassini VIMS, Icarus, in press

Dong, Y., T. W. Hill, and S.-Y. Ye (2015), Characteristics of ice grains in the Enceladus plume from Cassini observations, J. Geophys. Res. Space Physics, 120, 915–937

Dougherty, M.K., Khurana, K.K., Neubauer, F.M., Russell, C.T., Saur, J., Leisner, J.S., Burton, M.E. (2006) Identification of a dynamic atmosphere at Enceladus with the Cassini magnetometer, *Science, 311*, 1406–1409.

Emery, J. P., D. M. Burr, D. P. Cruikshank, R. H. Brown, and J. B. Dalton (2005), Near-infrared (0.8–4.0micron) spectroscopy of Mimas, Enceladus, Tethys, and Rhea, Astron. Astrophys., 435, 353, doi:10.1051/0004- 6361:20042482.

Esposito, L. W. and 19 co-authors (2004), The Cassini Ultraviolet Imaging Spectrograph Investigation, Space Sci. Rev., **115**, 299

Esposito, L.W., J.E. Colwell, K.Larsen, W.E. McClintock, A.I.F. Stewart, J.T. Hallett, D.E. Shemansky, J.M. Ajello, C.J. Hansen, A.R. Hendrix, R.A. West, H.U. Keller, A. Korth, W.R. Pryor, R. Reulke, Y.L. Yung (2005), Ultraviolet Imaging Spectroscopy Shows an Active Saturnian System, *Science, 307*, 1251-1255.

Filacchione, G. and 18 co-authors (2012). Saturn's icy satellites and rings investigated by Cassini - VIMS. III. Radial compositional variability, Icarus Vol. 22, Issue 2, pp. 1064–1096.

Filacchione, G., D'Aversa, E., Capaccioni, F., et al. 2016. Saturn's icy satellites investigated by Cassini-VIMS. IV. Daytime temperature maps, Icarus, 271, 292

Goguen J.D, et al. (2013) The temperature and width of an active fissure on Enceladus measured with Cassini VIMS during the 14 April 2012 South Pole flyover. Icarus. 2013;226:1128–1137.

Grundy W.M., Buie M.W., Stansberry J.A., Spencer J.R., Schmitt B. (1999) Near-infrared spectra of icy outer solar system surfaces: Remote determination of H 2 O ice temperatures. Icarus 142:536-549.

Grün, E. and co-aurhors (1993). Discovery of Jovian dust streams and interstellar grains by the Ulysses spacecraft. Nature 362, 428–430.

Hamilton, D. and J. Burns (1993). Ejection of dust from Jupiter's gossamer ring. *Nature* 364, 695–699.

Hansen C. J., Esposito L., Stewart A. I. F., Colwell J., Hendrix A., Pryor W., Shemansky D., West R. (2006) Enceladus' water vapor plume, *Science* 311, 1423-1425.

Hansen C. J., Esposito L. W., Stewart A. I. F., Meinke B., Wallis B., Colwell J. E., Hendrix A. R., Larsen K., Pryor W., Tian F. (2008), Water vapour jets inside the plume of gas leaving Enceladus, Nature 456, 477-479.

Hansen, C. J., Shemansky D. E., Esposito L. W.,. Stewart I. A. F, Lewis B. R., Colwell J. E., Hendrix A. R., West R. A., Waite Jr. J. H., Teolis B., Magee B. A. (2011), The Composition and Structure of the Enceladus Plume, *GRL* 38:L11202.

Hansen**,** C. J., Esposito, L. W. , Aye, K.-M., Colwell, J. E., Hendrix, A. R., Portyankina, G., Shemansky, D (2017). Investigation of diurnal variability of water vapor in Enceladus' plume by the Cassini ultraviolet imaging spectrograph, GRL 44 10.1002/2016GL071853 (2017).

Hapke, B., Wagner, J., Cohen, A., Partlow, W., 1978. Reflectance measurements of lunar materials in the vacuum ultraviolet. Lunar and Planetary Science Conference IX, 456-458.

Hedman, M.M., Nicholso, P.D., Showalter, M.R., Brown, R.H., Buratti, B.J., Clark, R.N. (2009) Spectral Observations of the Enceladus Plume with Cassini-VIMS. Astrophys. Journal 693, 1749-1762.

Hedman, M.M., C.M. Gosmeyer, P.D. Nicholson, C. Sotin, R.H. Brown, R.N. Clark, K.H. Baines, B.J. Buratti & M.R. Showalter (2013) An observed correlation between plume activity and tidal stresses on Enceladus, *Nature*, *500*, 182–184.

Hedman, M.M., Dhingra, D., Nicholson, P.D., Hansen, C.J., Portyankina, G., Ye, S., Dong, Y. (2018) Spatial variations on the dust-to-gas ratio of Enceladus' plume, Icarus 305, 123 – 138.

Hendrix A. R., Hansen C. J., Holsclaw, G. M. (2010) The ultraviolet reflectance of Enceladus: Implications for surface composition. *Icarus* 206, 608-617.

Hill T.W. and Pontius D. (1998) Plasma injection near Io, *J. Geophys. Res*., *103*, 19879-19886.

Hill, T.W., Thomsen M.F., Tokar R.L., Coates A.J., Lewis G.R., Young D.T., Crary F.J., Baragiola R.A., Johnson R.E., Dong Y., Wilson R.J., Jones G.H., Wahlund J.-E., Mitchell D.G., and Horányi M. (2012) Charged nanograins in the Enceladus plume, *J. Geophys. Res*., *117*, A05209.

Hillier, J. K., Green, S. F., McBride, N., Schwanethal, J. P., Postberg, F., Srama, R., Kempf, S., Moragas-Klostermeyer, G., McDonnell, J. A. M., and E. Grün (2007). The composition of Saturn's E ring. MNRAS 377, 1588–1596.

Hodyss, R., Parkinson C. D., Johnson P. V., Stern J. V., Goguen J. D., Yung Y. L., and Kanik I. (2009), Geophys. Res. Letters, **36**, L17103, doi:10.1029/2009GL039336.

Horányi, M., Morfill, G., and Grün E. (1993). Mechanism for the acceleration and ejection of dust grains from Jupiter's magnetosphere. *Nature* 363, 144–146.

Hsu, H.-W., .Kempf, S., Postberg, F., Srama, R., Jackman, C.M., Moragas-Klostermeyer, G., Helfert, S., and Grün, E. 2010. Interaction of the Solar Wind and Stream Particles, Results from the Cassini Dust Detector, AIP conference proceedings, Solar Wind 12, p.p. 154 – 163

Hsu, H.-W., Postberg, F., Kempf, S., Trieloff, M., Burton, M., Roy, M., Moragas-Klostermeyer, G., Srama, R. 2011. Stream Particles as the Probe of the Dust–Plasma–Magnetosphere Interaction at Saturn, Journal of Geophysical Research, Vol. 116, Issue A9, CiteID A09215

Hsu, H.W., Krüger, H., Postberg, F. (2012) Dynamics, Composition, and Origin of Jovian and Saturnian Dust Stream Particles, in 'Nanodust in the Solar System: Discoveries and Interpretations', Editors: Ingrid Mann, Nicole Meyer-Vernet, Andrzej Czechowski, Springer Astrophysics and Space Science Library 385, ISBN 978-3-642-27542-5

Hsu, H.W., Postberg, F., Sekine, Y. and 12 co-authors (2015) Ongoing hydrothermal acitivities within Enceladus, Nature, Vol. 519, p. 207-210.

Hurley, D. M., Perry M. E., and Waite J. H. (2015), Modeling insights into the locations of density enhancements from the Enceladus water vapor jets, J. Geophys. Res. Planets, 120, 1763–1773, doi:10.1002/ 2015JE004872.

Ingersoll, A.P., Ewald, S.P. (2011) Total particulate mass in Enceladus plumes and mass of Saturn's E ring inferred from Cassini ISS images, Icarus 216, 492 – 506.

Ingersoll, A.P., Ewald, S.P. (2017). Decadal timescale variability of the Enceladus plumes inferred from Cassini images, Icarus 282, 260 – 275.

Jaumann, R. and 16 co-authors (2008), Distribution of Icy Particles Across Enceladus' Surface as Derived from Cassini-VIMS Measurements, *Icarus* **193** (2008) 407419, doi:10.1016/j.icarus.2007.09.013.

Johnson, R.E., Pospieszalska M.K., Sittler Jr. E.C., Cheng A.F., Lanzerotti L.J., Sieveka E.M. (1989) The neutral cloud and heavy ion inner torus at Saturn, *Icarus*, *77*, 311-329.

Johnson R.E., Smith H.T., Tucker O.J., Liu M., Burger M.H., Sittler E.C., and. Tokar R.L. (2006) The Enceladus and OH Tori at Saturn, *Astrophys. J.*, *644*, L137-L139.

Jones, G.H., Arridge C. S., Coates A. J., Lewis G. R., Kanani S., Wellbrock A., Young D. T., Crary F. J., Tokar R. L., Wilson R. J., Hill T. W., Johnson R. E., Mitchell D. G., Schmidt J., Kempf S., Beckmann U., Russell C. T., Jia Y. D., Dougherty M. K., Waite Jr. J. H., Magee B. (2009) Fine jet structure of electrically-charged grains in Enceladus' plume, *Geophys. Res. Lett.*, *36*, L16204.

Kempf, S., Srama, R., Horányi, M., Burton, M., Helfert, S., Moragas-Klostermeyer, G., Roy, M., and E. Grün 2005a. High-velocity streams of dust originating from Saturn. *Nature* 433, 289–291.

Kempf, S., Srama, R., Postberg, F., Burton, M., Green, S. F., Helfert, S., Hillier, J. K., McBride, N., McDonnell, J. A. M., Moragas-Klostermeyer, G., Roy, M., and E. Grün 2005b. Composition of Saturnian Stream Particles. *Science* 307, 1274–1276.

Kempf, S., Beckmann, U., Moragas-Klostermeyer, G., Postberg, F., S. R., Economou, T., Schmidt, J., Spahn, F., and E. Grün 2008 The E ring in the vicinity of Enceladus I: Spatial distribution and properties of the ring particles. *Icarus* 193, 420-437

Kempf, S., Beckmann, U., Schmidt, J., 2010. How the Enceladus dust plume feeds Saturn's E ring. Icarus 206, 446-457.

Khawaja, N. , Postberg, F., Schmidt, J. (2017) The Compositional Profile of the Enceladian Ice Plume from the Latest Cassini Flybys. LPSC 48 (2017), Abstract 2005.

Kieffer, S. W. et al. A Clathrate Reservoir Hypothesis for Enceladus' South Polar Plume. *Science* **314**, 1764-1766 (2006)

Kite E. S. and Rubin A. M. (2016) Sustained eruptions on Enceladus explained by turbulent dissipation in tiger stripes. *Proc. Natl. Acad. Sci*., 113(15), 3972–3975.

Krimigis, S.M., Mitchell, D.G., Hamilton, D.C. et al. Space Sci Rev (2004) 114: 233. https://doi.org/10.1007/s11214-004-1410-8

Le Gall, A. and 17 co-authors (2017) Thermally anomalous features in the subsurface of Enceladus's south polar terrain. Nature Astronomy, Vol. 1, Nr. 63.

Leisner, J.S., C.T. Russell, M.K. Dougherty, X. Blanco-Cano, R.J. Strangeway and C. Bertucci (2006) Ion cyclotron waves in Saturn's E ring: Initial Cassini observations, *Geophys. Res. Lett*., *33*, L11101.

Lhuissier, H., & Villermaux, E. (2012). Bursting bubble aerosols. *Journal of Fluid Mechanics, 696*, 5-44. doi:10.1017/jfm.2011.418

Magee, B.A. & Waite, J.H. (2017), LPSC 48, Abstract 2974, Neutral Gas Composition of Enceladus' Plume – Model Parameter Insights from Cassini-INMS

Martonchik, J.V., Orton, G.S., Appleby, J.F., 1984. Optical properties of NH3 ice from the far infrared to the near ultraviolet. Appl. Opt. 23, 541–547.

Mastrapa, R.M.E., Brown, R.H. (2006) Ion irradiation of crystalline H2O-ice: Effect on the 1.65-lm band. Icarus 183, 207–214.

Mastrapa, R.M.E., Grundy, W.M., Gudipati, M.S. (2013) Amorphous and Crystalline H2O-Ice. The Science of Solar System Ices, pp. 371–408.

Matson, D.L., Castillo-Rogez, J.C., Davies, A.G., Johnson, T.V. (2012). Enceladus: A hypothesis for bringing both heat and chemicals to the surface, Icarus, Vol. 221, 53 – 62.

McCord, T. and 24 co-authors (2004). Cassini VIMS observations of the Galilean satellites including the VIMS calibration procedure. Icarus 172, 104-126.

McKinnon, W B. Effect of Enceladus's rapid synchronous spin on interpretation of Cassini gravity (2015). GRL (42), Issue 7, 2137 - 2143

Meier, P., Kriegel, H., Motschmann, U., Schmidt, J., Spahn, F., Hill, T. W., Dong, Y., Jones, G. H. (2014) A model of the spatial and size distribution of Enceladus' dust plume, *PSS*, 104, 216-233.

Meier, P., Motschmann, U., Schmidt, J., Spahn, F., Hill, T. W., Dong, Y., Jones, G. H. Kriegel, H. (2015) Modeling the total dust production of Enceladus from stochastic charge equilibrium and simulations, *PSS,* 119, 208-221.

Morooka, M.W., Wahlund J.-E., Eriksson A.I., Farrell W.M., Gurnett D.A., Kurth W.S., Persson A.M., Shafiq M., Andre M., Holmberg M.K.G. (2011). Dusty plasma in the vicinity of Enceladus, *J. Geophys. Res., 116*, A12221.

Nimmo, F., Porco, C., Mitchel. C (2014). Tidally Modulated Eruptions on Enceladus: Cassini ISS Observations and Models, *The Astronomical Journal* 148:46, 14pp.

Perry, M. E. *et al.* (2015) Cassini INMS measurements of Enceladus plume density. *Icarus* **257**, 139–162

Pierel J.D.R, Nixon C.A., Lellouch E., Fletcher L.N., Bjoraker G.L., Achterberg R.K., Bézard B., Hesman B.E., Irwin P.G.J., Flasar F.M. (2017) D/H ratios on Saturn and Jupiter from Cassini CIRS, The Astronomical Journal 154, 154-178.

Pitman, K. M., Buratti, B. J., Mosher, J. A., (2010) Disk-integrated bolometric Bond albedos and rotational light curves of saturnian satellites from Cassini Visual and Infrared Mapping Spectrometer. Icarus 206, 537 – 560.

Pitman K.M., Kolokova L., Verbiscer A.J., Mackowski D.W., Joseph E.C.S. (2017) Coherent backscattering effect in spectra of icy satellites and its modeling using multi-sphere T-matrix (MSTM) code for layers of particles, PSS 149, 23 – 31.

Porco, C.C., Helfenstein P., Thomas P.C., Ingersoll A.P., Wisdom J., West R., Neukum G., Denk T., Wagner R., Roatsch T., Kieffer S., Turtle E., McEwen A., Johnson T.V., Rathbun J., Veverka J., Wilson D., Perry J., Spitale J., Brahic A., Burns J.A., DelGenio A.D., Dones L., Murray C.D. and Squyres S. (2006) Cassini Observes the Active South Pole of Enceladus, *Science*, *311*, 1393-1401.

Porco, C., DiNino, D., Nimmo, F. (2014). How the Geysers, Tidal Stresses, and Thermal Emission across the South Polar Terrain of Enceladus are Related, *The Astronomical Journal* 148:45, 24pp.

Porco, C., Dones, L., Mitchell, C. Could it be snowing microbes on Enceladus? Asessing conditions in ist plume and implications for future missions (2017). Astrobiology 17 (9), 876 – 912.

Postberg, F., Kempf, S., Srama, R., Green, S. F., Hillier, J. K., McBride, N., and Grün E. (2006). Composition of jovian dust stream particles. *Icarus* 183, 122–134.

Postberg, F, Hillier, J. K., Kempf, S., Srama, R., Green, S. F., McBride, N. and Grün E. (2008) The E-ring in the vicinity of Enceladus II. Probing the moon's interior—the composition of E-ring particles. Icarus 193, 438–454.

Postberg, F., Kempf, S., Schmidt, J., Brillantov, N., Beinsen, A., Abel, B., Buck, U., Srama, R. (2009a) Sodium salts in E ring ice grains from an ocean below the surface of Enceladus. Nature 459, 1098–1101.

Postberg, F., Kempf, S., Rost, D., Stephan, T., Srama, R., Trieloff, M., Mocker, A., Goerlich, M. (2009b). Discriminating contamination from particle components in spectra of Cassini's dust detector CDA, Planetary and Space Science 57, 1359–1374

Postberg, F., Schmidt J., Hillier, J.K., Kempf S., Srama, R. (2011a) A salt-water reservoir as the source of a compositionally stratified plume on Enceladus, Nature, Vol. 474, Issue 7353, 620-622.

Postberg, F., Grün E., Horanyi M., Kempf S., Krueger H., Srama R.,Sternovsky Z., Srama R. (2011b) Compositional Mapping of Planetary Moons by Mass Spectrometry of Dust Ejecta, Planetary and Space Science, Vol. 59, 1815–1825.

Postberg, F., Tobie, G., Dambeck, T. (2016) Under the Sea of Enceladus. Scientific American Vol 315, Nr. 4., 38-45.

Postberg, F., Khawaja, N. and 19 co-authors.(2018) Macromolecular organic compounds from the depths of Enceladus, Nature, in press.

Ries, P.A. & Jansen, M (2015) A large-scale anomaly in Enceladus' microwave emission. Icarus 257, 88–102.

Schenk, P., Hamilton, D., Johnson, R., McKinnon, W., Paranicas, C., Schmidt, J., Showalter, M., 2011. Plasma, plumes and rings: Saturn system dynamics as recorded in global color patterns on its midsize icy satellites. Icarus 211, 740-757.

Schippers, P., Blanc M., Andre N., Dandouras I., Lewis G.R., Gilbert L.K., Persoon A.M., Krupp N., Gurnett D.A., Coates A.J., Krimigis S.M., Young D.T., Dougherty M.K. (2008) Multi-instrument analysis of electron populations in Saturn's magnetosphere, *J. Geophys. Res*., *113*, A07208.

Schmidt, J., Brillantov, N., Spahn, F. & Kempf, S. (2008). Slow dust in Enceladus' plume from condensation and wall collisions in tiger stripe fractures. Nature 451, 685–688.

Scipioni, F., Schenk P., Tosi F., D'Aversa E., Clark R., Combe J.-Ph., Dalle Ore C.M., 2017, Deciphering sub-micron ice particles on Enceladus surface, Icarus 290 183–200.

Sekine, Y., Shibuya, T., Postberg, F., Hsu, H.W., Suzuki, K., Masaki, Y., Kuwatani, T., Mori, M., Hong, P.K., Yoshizaki, M., Tachibana, S., & Sirono, S. (2015) High-temperature water-rock interactions and hydrothermal environments in the chondrite-like core of Enceladus, Nature comms. 6, 8604, DOI: 10.1038/ncomms9604

Shemansky, D. E., Matheson P., Hall D.T., Hu H.-Y., Tripp T.M. (1993), Detection of the hydroxyl radical in the Saturn magnetosphere, *Nature, 363*, 329-331.

Shemansky, D.E., Yoshii, J., Hansen, C., Hendrix, A.m Xianming, L., Yung, Y (2016), The Complex Highly Structured Near Enceladus Environment: Analysis of Cassini UVIS Image Cube Vectors in the FUV, AOGS 2016, abstract PS06-A025.

Simon, S., Saur, J., Kriegel, H., Neubauer, F. M., Motschmann, U., Dougherty, M. K. (2011) Influence of negatively charged plume grains and hemisphere coupling currents on the structure of Enceladus' Alfven wings: analytical modeling of Cassini magnetometer observations. *J. Geophys. Res*., *116*, A04221.

Smith, H.T., Shappirio M., Sittler E.C., Reisenfeld D., Johnson R.E., Baragiola R.A., Crary F.J., McComas D.J. and Young D.T. (2005) Discovery of nitrogen in Saturn's inner magnetosphere, *Geophys. Res. Lett*., *32*, L14S03.

Smith, H.T., Johnson R.E., Sittler E.C., Shappirio M., Reisenfeld D., Tucker O.J., Burger M., Crary F.J., McComas D.J. and Young D.T. (2007) Enceladus: The likely dominant nitrogen source in Saturn's magnetosphere, *Icarus*, *188*, 356–366.

Smith, H.T., Shappirio M., Johnson R.E., Reisenfeld D., Sittler E.C., Crary F.J., McComas D.J. and Young D.T. (2008) Enceladus: A potential source of ammonia products and molecular nitrogen for Saturn's magnetosphere, *J. Geophys. Res*., *113*, A11206.

Smith, H.T., Johnson R.E., Perry M.E., Mitchell D.G., McNutt R.L., and Young D.T. (2010), Enceladus plume variability and the neutral gas densities in Saturn's magnetosphere, *J. Geophys. Res., 115*, A10252.

Southworth B. S., Kempf, S., Spitale, J. Surface Deposition of the Enceladus Plume and the Angle of Emissions, in review with Icarus 2018

Spahn, F. and 15 colleagues, 2006. Cassini Dust Measurements at Enceladus and Implications for the Origin of the E Ring. Science 311, 1416–1418.

Spencer at al. (2013) EPSC Abstracts Vol. 8, EPSC2013-840-1, 2013, European Planetary Science Congress 2013

Spitale, J. N., Porco, C. C. (2007) Association of jets on Enceladus with the warmest regions on its south-polar fractures. *Nature* **449**, 695-69.

Spitale, J. N.; Hurford, T. A.; Rhoden, A. R.; Berkson, E. E.; Platts, Symeon, S. (2015). Curtain Eruptions from Enceladus' south-polar terrain; Nature 521, 7550, pp.57-60.

Srama, R. and 43 co-authors (2004) The Cassini Cosmic Dust Analyser. Space Science Review 114, 465–518.

Teolis B.D., Perry M.E., Hansen, C.J., Waite J.H., Porco C.C., Spencer J.R., Howett C.J.A. (2017). Enceladus Plume Structure and Temporal Variability: Comparison of Cassini Observations, submitted

Thompson W. R., Murray B. G. J. P. T., Khare B. N., Sagan C. (1987) Coloration and darkening of methane clathrate and other ices by charged particle irradiation: Applications to the outer Solar System. *J. Geophys. Res.* 92, 14933-14947.

Thomsen, M.F., Reisenfeld D.B., Delapp D.M., Tokar R.L., Young D.T., Crary F.J., Sittler E.C., McGraw M.A. and Williams J.D. (2010) Survey of ion plasma parameters in Saturn's magnetosphere, *J. Geophys. Res*., *115*, A10220.

Tokar, R. L., Johnson R.E., Hill T.W., Pontius T.D.H., Kurth W.S., Crary F.J., Young D.T., Thomsen M.F., Reisenfeld D.B., Coates A.J., Lewis G.R., Sittler E.C., Gurnett D.A. (2006) The Interaction of the Atmosphere of Enceladus with Saturn's Plasma, *Science*, *311*, 1409-1412.

Tokar, R.L., Wilson R.J., Johnson R.E., Henderson M.G., Thomsen M.F., Cowee M.M., Sittler Jr. E.C., Young D.T., Crary F.J., McAndrews H.J. and Smith H. T. (2008) Cassini detection of water-group pick-up ions in the Enceladus torus, *Geophys. Res. Lett*., *35*, L14202.

Tokar, R.L., Johnson R.E., Thomsen M.F., Wilson R.J., Young D.T., Crary F.J., Coates A.J., Jones G.H., Paty C.S. (2009) Cassini Detection of Enceladus' Cold Water-Group Plume Ionosphere, *Geophys. Res. Lett.*, *36*, L13203.

Verbiscer A. J., French R. G., McGhee C. A. (2005) The opposition surge of Enceladus: HST observations 338-1022 nm. *Icarus* 173, 66-83.

Verbiscer A. J., Peterson D. E., Skrutskie M. F., Cushing M., Helfenstein P., Nelson M. J., Smith J. D., Wilson, J. C. (2006) Near-infrared spectra of the leading and trailing hemispheres of Enceladus. *Icarus* 182, 211-223.

Verbiscer, A., French, R., Showalter, M., Helfenstein, P. (2007) Enceladus: Cosmic Graffiti artist caught in the act. Science, 315, 5813, pp. 815

Waite, J. H. and 15 co-authors (2004), The Cassini Ion and Neutral Mass Spectrometer (INMS) investigation, Space Sci. Rev., 114, 113-231, 2004.

Waite, J. H., Combi, M. R., Ip, W.-H., Cravens, T. E., McNutt, R. L., Kasprzak, W., Yelle, R., Luhmann, J., Niemann, H., Gell, D., Magee, B., Fletcher, G., Lunine, J., andW.-L. Tseng (2006). Cassini Ion and Neutral Mass Spectrometer: Enceladus Plume Composition and Structure. Science 311, pp. 1419–1422.

Waite, J. H., Lewis W.S., Magee B.A., Lunine J.I., McKinnon W.B., Glein C.R., Mousis O., Young D.T., Brockwell T., Westlake J., Nguyen M.-J., Teolis B., Niemann H., McNutt R., Perry M. & Ip W.-H. (2009). Liquid water on Enceladus from observations of ammonia and ^{40}Ar in the plume. Nature 460, pp. 487–490.

Waite J.H. and 12 co-authors et al., Cassini finds molecular hydrogen in the Enceladus plume: Evidence for hydrothermal processes (2017), *Science* 356, 6334, pp155-159.

Walker J. D., Chocron S., Waite J. H., and Brockwell T., The Vaporization Threshold: Hypervelocity Impacts of Ice Grains Into a Titanium Cassini Spacecraft Instrument Chamber, Procedia Engineering 103, 628-635, 2015 (Proceedings of the 2015 Hypervelocity Impact Symposium).

Wilson, R.J., Tokar R.L., Henderson M.G., Hill T.W., Thomsen M.F., and Pontius Jr. D.H. (2008). Cassini plasma spectrometer thermal ion measurements in Saturn's inner magnetosphere, *J. Geophys. Res.*, *113*, A12218.Y

Yeoh, S.K, Chapman, T.A., Goldstein, D.B., Varghese, P.L., Trafton, L.M. (2015). On understanding the physics of the Enceladus south polar plume via numerical simulation, Icarus 253, pp.205-222.

Young, D.T., Berthelier J.-J., Blanc M., Burch J. L., Coates A. J., Goldstein R. , Grande M., Hill T.W., Johnson R. E., Kelha V., McComas D. J., Sittler E. C., Svenes K. R., Szegv K., Tanskanen P., Ahola K., Anderson D., Bakshi S., Baragiola R. A., Barraclough B. L., Black R., Bolton S., Booker T., Bowman R., Casey P., Dirks G., Eaker N., Gosling J.T., Hannula H., Holmlund C.,.Huomo H, Illiano J.-M., Jensen P., Johnson M. A., Linder D., Luntama T., Maurice S., McCabe K., Narheim B. T., Nordholt J. E., Preece A., Rutzki J., Ruitberg A., Smith K., Szalai S., Thomsen M.F., Viherkanto K., Vollmer T., Wahl T.E., Wuest M., Ylikorpi T. and Zinsmeyer C. (2004) Cassini Plasma Spectrometer Investigation, *Space Sci. Rev.*, *114*, 1-112.

Young, D.T., Berthelier J.-J., Blanc M., Burch J. L., Bolton S., Coates A. J., Crary F.J., Dunlop M. W., R. Goldstein R. , Grande M., Hill T.W., Johnson R. E., Baragiola R. A., Kelha V., McComas, Mursula, K., D. J., Sittler E. C., Svenes K. R., Szegö K., Tanskanen P., Thomsen M.F., Bakshi S., Barraclough B. L., Bebesi D., Delapp D., Dunlop M.W., Gosling J.T., Furman J.D., Gilbert L.K., Glenn D., Holmlund C., Illiano J.-M., Lewis G.R., Linder D.R., Maurice S., McAndrews H.J., Narheim B.T., Pallier E., Reisenfeld D., Rymer A.M.,. Smith H.T, Tokar R.L.,Ylikorpi T. and Zinsmeyer C. (2005) Composition and Dynamics of Plasma in Saturn's Magnetosphere, *Science*, *307*, 1262-1265.

Zastrow, M, Clarke, J.T., Hendrix, A.R., Noll, K.S. (2012). UV Spectrum of Enceladus, Icarus 220, pp. 29-35

Zolotov, M. Y. (2007) An oceanic composition on early and today's Enceladus. Geophys. Res. Lett. 34, L23203.